

9-21-2017

# Physical Property Extraction of Powder Contaminated Surfaces from Longwave Infrared Hyperspectral Imagery

Timothy Gibbs  
tjg7873@rit.edu

Follow this and additional works at: <http://scholarworks.rit.edu/theses>

---

## Recommended Citation

Gibbs, Timothy, "Physical Property Extraction of Powder Contaminated Surfaces from Longwave Infrared Hyperspectral Imagery" (2017). Thesis. Rochester Institute of Technology. Accessed from

This Dissertation is brought to you for free and open access by the Thesis/Dissertation Collections at RIT Scholar Works. It has been accepted for inclusion in Theses by an authorized administrator of RIT Scholar Works. For more information, please contact [ritscholarworks@rit.edu](mailto:ritscholarworks@rit.edu).

Physical Property Extraction of Powder Contaminated Surfaces  
from Longwave Infrared Hyperspectral Imagery

by

Timothy Gibbs

B.S. Meteorology, The College at Brockport, 2013

B.S. Water Resources, The College at Brockport, 2013

A dissertation submitted in partial fulfillment of the  
requirements for the degree of Doctor of Philosophy  
in the Chester F. Carlson Center for Imaging Science  
College of Science

Rochester Institute of Technology

September 21, 2017

Signature of the Author \_\_\_\_\_

Accepted by \_\_\_\_\_  
Coordinator, Ph.D. Degree Program Date



CHESTER F. CARLSON CENTER FOR IMAGING SCIENCE  
COLLEGE OF SCIENCE  
ROCHESTER INSTITUTE OF TECHNOLOGY  
ROCHESTER, NEW YORK

CERTIFICATE OF APPROVAL

---

Ph.D. DEGREE PROPOSAL

---

The Ph.D. Degree Proposal of Timothy Gibbs  
has been examined and approved by the  
dissertation committee as satisfactory for the  
dissertation required for the  
Ph.D. degree in Imaging Science

---

Dr. David W. Messinger, Dissertation Advisor	Date
--	------

---

Coordinator Ph.D. Degree Program	Date
----------------------------------	------

---

Dr. Carl Salvaggio	Date
--------------------	------

---

Dr. Charles M. Bachmann	Date
-------------------------	------

---

Dr. Surendra Gupta	Date
--------------------	------

DISSERTATION RELEASE PERMISSION  
ROCHESTER INSTITUTE OF TECHNOLOGY  
COLLEGE OF SCIENCE  
CHESTER F. CARLSON CENTER FOR IMAGING SCIENCE

Title of Dissertation:

**Physical Property Extraction of Powder Contaminated Surfaces from  
Longwave Infrared Hyperspectral Imagery**

I, Timothy Gibbs, hereby grant permission to Wallace Memorial Library of R.I.T. to reproduce my thesis in whole or in part. Any reproduction will not be for commercial use or profit.

Signature \_\_\_\_\_ Date \_\_\_\_\_



# Contents

<b>1</b>	<b>Introduction</b>	<b>23</b>
1.1	Objectives . . . . .	25
1.1.1	Tasks . . . . .	25
1.2	Scope . . . . .	26
1.3	Overview . . . . .	26
<b>2</b>	<b>Background</b>	<b>29</b>
2.1	Remote Sensing . . . . .	29
2.2	Solar Reflected Radiation . . . . .	30
2.3	Infrared Radiation . . . . .	31
2.4	Electromagnetic Radiation Collection Geometry . . . . .	33
2.5	Material Properties . . . . .	35
2.6	Temperature Emissivity Separation . . . . .	37
2.6.1	Fixed Window Technique . . . . .	38
2.6.2	Moving Window Technique . . . . .	39
2.6.3	Known Temperature . . . . .	40
2.6.4	Full Scene Methods . . . . .	41
2.7	Material Mixtures and Contaminants . . . . .	44
2.7.1	Gaseous Contaminants . . . . .	44
2.7.2	Liquid Contaminants . . . . .	45
2.7.3	Solid Materials Properties . . . . .	46
2.8	Particle Size Considerations . . . . .	47
2.9	Chemical Composition . . . . .	49
2.10	Solid Contamination Properties . . . . .	52
<b>3</b>	<b>Theory</b>	<b>57</b>
3.1	NEFDS Contamination Model . . . . .	57
3.1.1	NEFDS Contamination Model Parameters . . . . .	62
3.2	Extinction Cross Section . . . . .	63
3.3	Signature Injection . . . . .	64
3.4	Simulated Contaminant Scenes . . . . .	66

<b>4</b>	<b>Methods</b>	<b>69</b>
4.1	Measurements . . . . .	70
4.1.1	Substrate and Contaminant Selection . . . . .	72
4.1.2	Powder Deposition Technique . . . . .	73
4.1.3	LWIR Instrumentation . . . . .	75
4.2	Estimation of Physical Parameters . . . . .	78
4.3	Direct Cross Section Measurement . . . . .	83
4.3.1	Light Source . . . . .	84
4.3.2	Integrating Sphere Experimental Design . . . . .	84
4.3.3	Disk Making . . . . .	87
4.4	Scene Simulation . . . . .	90
4.5	Signature Injection . . . . .	91
4.6	Signature Injected HSI Data . . . . .	92
<b>5</b>	<b>Results</b>	<b>95</b>
5.1	FTIR Instrument Analysis . . . . .	96
5.1.1	Blackbody Characterization . . . . .	96
5.1.2	Effect of Nitrogen Dewar . . . . .	99
5.2	microDIRISIG Modeling . . . . .	100
5.3	Direct Extinction Cross Section Measurements . . . . .	101
5.3.1	Integrating Sphere Measurements . . . . .	102
5.3.2	Blackbody Measurements . . . . .	104
5.3.3	Integration into Parameter Inversion Model . . . . .	107
5.4	Parameter Inversion Estimate Results . . . . .	110
5.4.1	Scalability Test . . . . .	110
5.4.2	Measured Results . . . . .	112
5.4.3	Contrast Ratio . . . . .	114
5.4.4	Estimated Extinction Cross Section . . . . .	118
5.4.5	Comparisons Across Measurement Sets . . . . .	120
5.4.6	Scalar Parameter Estimates and Mixture Reconstruction . . . . .	122
5.4.7	Derived Total Mass . . . . .	126
5.4.8	Statistical Analysis . . . . .	129
5.5	Signature Injections . . . . .	133
5.5.1	PSF vs. No PSF . . . . .	135
5.6	Target Detection . . . . .	137
5.6.1	Red Chalk . . . . .	141
5.6.2	Silicon Carbide . . . . .	142
5.7	Blue Heron Real Airborne Data . . . . .	144
5.7.1	Target Detection Analysis . . . . .	146
5.7.2	Application into the Inversion Model . . . . .	148

<b>6 Summary</b>	<b>157</b>
6.1 Future Considerations . . . . .	159
<b>A X-Ray Diffraction Data</b>	<b>161</b>
<b>B Scanning Electron Microscope Images</b>	<b>165</b>
<b>C Parameter Inversion Results: Additional Data Collections</b>	<b>171</b>
C.1 Chalk on Asphalt . . . . .	171
C.2 Quartz Sand . . . . .	174
C.3 Silicon Carbide . . . . .	179
C.4 Fused Silica . . . . .	182
<b>D Additional Extinction Cross Section Results</b>	<b>187</b>
<b>E ROC Curve Results for Blue Heron Synthetic Targets</b>	<b>193</b>



# List of Figures

1.1	Fused Silica dust coating a painted aluminum surface. . . . .	25
2.1	Visual representation of various paths photons travel to reach a sensor in the longwave infrared. Taken from Schott (1997), Figure 3.3. . . . .	33
2.2	Geometry of the a surface receiving incident energy at angles specified with an ‘i’ subscripts and reflected in a direction specified by ‘r’ subscript angles. . . . .	34
2.3	Three cases of a scattering by electromagnetic energy. The left-most image represents the ideal specular case and the right-most image represents the ideal diffuse case for scattering. The center image is representative of most objects, where scattering is fairly diffuse, with an low intensity specular lobe. . . . .	35
2.4	Derived emissivity spectra of quartz sand for temperatures between 306 and 316 K. The red line represents the best emissivity estimate and its temperature based on spectral smoothness within a fixed window. . . .	39
2.5	Derived emissivity for the user defined fixed spectral window from 8.12-8.6 $\mu m$ . At 312 Kelvin, the emissivity has the smoothest features within the fixed window and therefore represents the best estimate for emissivity. . . .	40
2.6	A comparison of spectral emissivity derivation from various temperature emissivity separation methods. . . . .	41
2.7	A recreation of a standard scatter plot to estimate atmospheric parameters. Plot represents the observed vs Planck radiance for each wavelength. Image taken from Figure 3 of Borel (2003). . . . .	43
2.8	Gas absorption spectra of $NH_3$ from Eismann, Figure 4.18. . . . .	45
2.9	Change in emissivity given angle for Quartz sand. Measurements taken at Sand Mountain Recreation Area in Sand Mountain, Nevada. . . . .	47
2.10	Little change in emissivity given angle occurs for another size that is not quartz. Measurements taken at the Nevada Automotive Testing Center in Nevada. . . . .	48



2.11	Reflectance change of quartz material between different particle sizes. The solid line represents a polished piece of quartz, the dashed line is the reflectance of large quartz particles ( $75 - 250\mu m$ ) and the small dashed line is the reflectance of fine particles ( $> 75\mu m$ ). Taken from Salisbury and Wald (1992), Figure 1B . . . . .	49
2.12	Emissivity of quartz particle sizes ranging from 15 to $277\mu m$ on a wavenumber( $cm^{-1}$ ) scale. Note that $1000\text{ }cm^{-1}$ is approximately $10\mu m$ . Taken Figure 6a from Moersch and Christiansen (1995) . . . . .	50
2.13	Pure silicon carbide powder emissivity. . . . .	53
2.14	X-ray diffraction images of silicon carbide powder. Data was collected in the material science department at the Rochester Institute of Technology in August 2016. . . . .	54
2.15	The average and standard deviation of critical parameters . . . . .	55
4.1	A flow chart depicting an overview of the project. . . . .	70
4.2	One inch thick aluminum plate painted with Krylon 1602 Ultra Flat Black spray paint. . . . .	71
4.3	Humboldt sieve used to apply contaminants to the substrate surfaces. . . . .	74
4.4	Designs and Prototypes FTIR 102 instrument set up. . . . .	76
4.5	Surface Optics Corporation 400-T Reflectometer. The aperture (seen in gold at the top of the instrument) is roughly half an inch in diameter. . . . .	78
4.6	Diagram of inner workings of SOC-400T reflectometer. Taken from SOC-400 manual. . . . .	79
4.7	Flow Chart of model parameter inversion process. . . . .	81
4.8	Labsphere 2 inch infragold integrating sphere. . . . .	83
4.9	Measured radiance at intervals across two hour period for EK-573X IR emitter light bulb . . . . .	85
4.10	Radiance shift at three wavelengths over two hours for EK-573X IR emitter light bulb. . . . .	86
4.11	X-Press 3630 40 ton disk press. . . . .	88
4.12	A disk compressed with silicon carbide powder and bound with potassium bromide. . . . .	89
5.1	Measured Radiance of a Blackbody Using the CI SR-80 blackbody with the D&P . . . . .	97
5.2	A close up look at the location of peak blackbody radiance for each time interval measurement using the D&P. . . . .	97
5.3	Calculated standard deviation for the blackbody as measured by the D&P . . . . .	98
5.4	Calculated variance of the blackbody radiance for the D&P . . . . .	99
5.5	The measured peak wavelength of the CI SR-80 blackbody measured by the D&P . . . . .	99

5.6	Radiance Ratio between the pristine integrating sphere to one with two amounts of silicon carbide contamination. . . . .	103
5.7	Extinction . . . . .	104
5.8	Derived extinction cross section parameter found from blackbody transmission measurements of compressed disks of fused silica powder. . . . .	106
5.9	Derived extinction cross section parameter found from blackbody transmission measurements of compressed disks of red chalk powder. . . . .	107
5.10	Derived extinction cross section parameter found from blackbody transmission measurements of compressed disks of silicon carbide powder. . . . .	108
5.11	Derived extinction cross section parameter found from blackbody transmission measurements of lowest number density compressed disk of fused silica powder. . . . .	109
5.12	Derived extinction cross section parameter found from blackbody transmission measurements of lowest number density compressed disk of red chalk powder. . . . .	110
5.13	Derived extinction cross section parameter found from blackbody transmission measurements of lowest number density compressed disk of silicon carbide powder. . . . .	111
5.14	Measured emissivity of various amounts of fused silica powder on hardened clay soil in Nevada. Also captured are emissivity measurements of the hardened clay soil without contaminant and an optically thick layer of fused silica. . . . .	112
5.15	Measured emissivity of various amounts of red chalk (Calcium Carbonate and Red Iron Oxide) powder on a concrete surface. Also captured are emissivity measurements of the pristine concrete and an ultra thick layer of red chalk. . . . .	114
5.16	Measured emissivity of various amounts of silicon carbide powder on a concrete surface. Also captured are emissivity measurements of the pristine concrete and an ultra thick layer of silicon carbide. . . . .	115
5.17	Contrast ratio of fused silica powder in three amounts. . . . .	116
5.18	Contrast ratio of red chalk powder in three amounts. . . . .	117
5.19	Contrast ratio of silicon carbide powder in three amounts. . . . .	118
5.20	Extinction cross section estimates for each contaminant amount of fused silica powder. Due to measurement error, sections of the estimated spectra between beyond 11.5 microns and between 8.0 and 8.25 microns are not considered for final estimates. . . . .	119
5.21	Extinction cross section estimates for each contaminant amount of red chalk powder. In ideal cases, limited variation will occur between each measurement. This example has variation in the largest amount of contaminant present, but good agreement between initial two estimates. . . . .	120

5.22	Extinction cross section estimates for each contaminant amount of silicon carbide powder. In ideal cases such as this, limited variation will occur between each measurement. . . . .	121
5.23	Extinction cross section estimates for each contaminant amount of red chalk powder. In ideal cases, limited variation will occur between each measurement. This example has variation in the largest amount of contaminant present, but good agreement between initial two estimates. . .	122
5.24	Extinction cross section estimates for each contaminant amount of silicon carbide powder. In ideal cases such as this, limited variation will occur between each measurement. . . . .	123
5.25	Measured and modeled comparison for fused silica powder on hardened clay coil. . . . .	124
5.26	Measured and modeled comparison for red chalk on concrete. . . . .	125
5.27	Measured and modeled comparison for silicon carbide powder on concrete. . . . .	126
5.28	Deposited versus Estimated total mass for each contaminant. . . . .	127
5.29	Histogram chart of the estimated results for the 2.11g application of silicon carbide on concrete for the $\beta$ parameter. . . . .	131
5.30	Histogram chart of the estimated results for the 2.11g application of silicon carbide on concrete for the $\frac{n}{a}$ parameter. . . . .	131
5.31	Histogram chart of the estimated results for the 2.11g application of silicon carbide on concrete for the derived total contaminant mass. . . . .	132
5.32	Derived total contaminant mass [g] for three contaminant amounts with varying temperature changes. . . . .	133
5.33	Blue Heron airborne sensor data with synthetic target signatures injected onto asphalt parking lot surface. This image was created without consideration to the effects of the point spread function created by the limitations in the optics of the Blue Heron sensor. Spectral plots show emissivity products of each pixel in a target block (9 total). . . . .	134
5.34	Spectral profiles of the nine target signatures from the center target block found in the middle row and fifth column of the target block grid. Targets in this block were created with the middle mixture parameters estimated from the parameter inversion model and contain target signatures in just 50% of each pixel. Little to no variability exists between the spectra due to the effects of the point spread function not being included in the target signatures. . . . .	135
5.35	Target signatures from pixels contained in the center target block (5th column, middle row) for silicon carbide. These target signatures contain the effects of the point spread function unlike the previous example. Variability exists between the middle pixel, edge pixels and corner pixels that would normally have been seen in real imagery. . . . .	136

5.36	Blue Heron airborne sensor data with synthetic target signatures injected onto asphalt parking lot surface. This image was created with consideration to the effects of the point spread function created by the limitations in the optics of the Blue Heron sensor. Clear variation occurs between center, edge and corner pixels from a visual and spectral standpoint. . .	138
5.37	Full scene image from Blue Heron sensor with the synthetic targets placed inside the bounds of the asphalt parking lot. Targets were blurred with the PSF of the sensor. . . . .	140
5.38	Target detection analysis of synthetic red chalk targets using the ACE algorithm. The best target spectrum for each target pixel are colored as pure contaminant spectrum (yellow), highest mixture spectrum (orange), middle mixture (green), lowest mixture (lighter blue). Background pixels are labeled dark blue. . . . .	142
5.39	Target detection analysis of synthetic silicon carbide targets using the ACE algorithm. The best target spectrum for each target pixel are colored as pure contaminant spectrum (yellow), highest mixture spectrum (orange), middle mixture (green), lowest mixture (lighter blue). Background pixels are labeled dark blue. . . . .	144
5.40	Left: 25g of silicon carbide powder placed across target area surrounded on all sides with aluminum wrapped 2x4 lumber. Aluminum helps provide high fidelity targets in airborne data. Right: 50g of silicon carbide powder placed across target area surrounded on all sides with aluminum wrapped 2x4 lumber. Aluminum helps provide high fidelity targets in airborne imagery. . . . .	145
5.41	Full scene image from Blue Heron sensor with the synthetic targets placed inside the bounds of the asphalt parking lot. Targets were blurred with the PSF of the sensor. . . . .	146
5.42	Left: Detection score map for ACE run with pure fused silica spectrum as target spectrum for Blue Heron data collection. Target pixels were detected at a 0.096 threshold with 38 target pixels identified to two false alarms. Right: Detection score map for ACE run with pure silicon carbide spectrum as target spectrum for Blue Heron data collection. Target pixels were detected at a 0.035 threshold with 19 target pixels identified to one false alarm. . . . .	148
5.43	Histogram of 1000 parameter inversion runs on the $0.0025 \frac{g}{cm^2}$ fused silica coverage density target. . . . .	150
5.44	Histogram of 1000 parameter inversion runs on the $0.0050 \frac{g}{cm^2}$ fused silica coverage density target. . . . .	151
5.45	Histogram of 1000 parameter inversion runs on the $0.0025 \frac{g}{cm^2}$ silicon carbide coverage density target. . . . .	152
5.46	Histogram of 1000 parameter inversion runs on the $0.0050 \frac{g}{cm^2}$ silicon carbide coverage density target. . . . .	152

5.47	Measured vs Modeled Estimates for fused silica targets placed in Blue Heron 11/12/17 flyover. Estimated coverage density for both targets is in near perfect agreement with the actual amounts placed in-scene. . .	153
5.48	Measured vs Modeled Estimates for silicon carbide targets placed in Blue Heron 11/12/17 flyover. Estimated coverage density for both targets is in near perfect agreement with the actual amounts placed in-scene. . .	154
5.49	Process to incorporate inversion model estimator with target detection	155
A.1	X-ray diffraction images of Fused Silica powder. Fused Silica has one broad intensity lobe, indicating that the material is comprised of multiple types of materials. The result is that the Fused Silica is amorphous, not crystalline like the other materials. Data was collected in the material science department at the Rochester Institute of Technology in August 2016. . . . .	162
A.2	X-ray diffraction images of Red Chalk powder. This confirms the technical data sheet that stated the material was a combination of calcium carbonate dyed with red iron oxide powder. Data was collected in the material science department at the Rochester Institute of Technology in August 2016. . . . .	163
B.1	Scanning Electron Microscope (SEM) images of Fused Silica powder at various zooming distances . . . . .	166
B.2	Scanning Electron Microscope (SEM) images of Red Chalk powder at various zooming distances . . . . .	167
B.3	Scanning Electron Microscope (SEM) images of Duralum White powder at various zooming distances . . . . .	168
B.4	The average and standard deviation of critical parameters . . . . .	169
C.1	Contrast Ratio for three mixtures of red chalk powder on asphalt. . . .	172
C.2	Extinction cross section for three mixtures of red chalk powder. . . . .	173
C.3	Measured emissivity (solid lines) vs modeled results for mixtures of red chalk powder on asphalt. Emissivity data for the bare substrate and pure contaminant are also included. . . . .	175
C.4	Contrast ratio for four mixtures of quartz sand on Krylon 1602 spray painted aluminum. . . . .	176
C.5	Extinction cross section for four mixtures of quartz. . . . .	178
C.6	Measured emissivity (solid lines) vs modeled results for four mixtures of quartz sand on Krylon 1602 painted aluminum. Emissivity data for the bare substrate and pure contaminant are also included. . . . .	178
C.7	Contrast ratio for three mixtures of Silicon Carbide (SiC) on Krylon 1602 painted aluminum. . . . .	180
C.8	Extinction cross section of three mixtures of Silicon Carbide (SiC). . . .	181

C.9	Measured Emissivity (solid lines) vs modeled emissivity results for three mixtures of Silicon Carbide (SiC) on Krylon 1602 painted aluminum. Emissivity data for the bare substrate and pure contaminant are also included. . . . .	182
C.10	Contrast Ratio for three mixtures of fused silica powder on Krylon 1602 painted aluminum. . . . .	183
C.11	Extinction cross section for three mixtures of Fused Silica powder. . . .	184
C.12	Measured emissivity (solid lines) vs Modeled emissivity results for three mixtures of fused silica powder on Krylon painted aluminum. Emissivity data for the bare substrate and pure contaminant are also included. . .	185
D.1	Average ratio of two amounts of silicon carbide powder placed inside the port cover of an infragold integrating sphere. The silicon carbide was not compressed into a disk prior to placement inside the integrating sphere. . . . .	188
D.2	Resulting extinction cross section measurement of the uncompressed silicon carbide material placed in the output port cover of the infragold integrating sphere. . . . .	189
D.3	Radiance ratios of fused silica to a pristine sphere found over a period of 1 hour. . . . .	190
D.4	Extinction cross section generated from fused silica in a infragold integrating sphere. . . . .	191
E.1	ROC generated curves for pure silicon carbide target spectrum using ACE, MF, CEM, and SAM target detection algorithms. . . . .	194
E.2	ROC generated curves for highest mixture amount of silicon carbide target spectrum using ACE, MF, CEM, and SAM target detection algorithms. . . . .	194
E.3	ROC generated curves for second highest mixture amount of silicon carbide target spectrum using ACE, MF, CEM, and SAM target detection algorithms. . . . .	195
E.4	ROC generated curves for lowest mixture amount of silicon carbide target spectrum using ACE, MF, CEM, and SAM target detection algorithms. . . . .	195



# List of Tables

3.1	NEFDS Contamination Model parameters and their respective definitions	61
4.1	Design and Prototypes Model 102F spot size differences by angle. . . . .	77
5.1	Best fit line statistics for each dataset of Applied vs Estimated contaminant total mass. . . . .	128
5.2	Estimated NEFDS contamination model scalar parameters and total mass for fused silica, red chalk and silicon carbide powder examples. Total mass is based on surface area of 10 inch diameter sieve. . . . .	128
5.3	Statistical analysis for parameter estimates of silicon carbide on concrete dataset. . . . .	129
5.4	Target detection statistics for fused silica and silicon carbide targets in Blue Heron imagery. . . . .	147
5.5	Parameter inversion estimates for coverage density of real Blue Heron targets . . . . .	149
C.1	Table of parameter estimates and total calculated mass for red chalk powder mixtures on asphalt. . . . .	174
C.2	Table of parameter estimates and total calculated mass for four mixtures of Quartz sand on Krylon 1602 painted aluminum sheet . . . . .	176
C.3	Table of parameter estimates and total calculated mass for four mixtures of quartz sand on Krylon 1602 painted aluminum. Results were obtained only with parameter estimates from steps 1,2 of the three-step parameter inversion technique. . . . .	177
C.4	Table of parameter estimates and total calculated mass for silicon carbide (SiC) on Krylon 1602 painted aluminum. . . . .	180
C.5	Table of parameter estimates and total calculated mass for Fused Silica powder on Krylon 1602 painted aluminum. . . . .	185



# Physical Property Extraction of Powder Contaminated Surfaces from Longwave Infrared Hyperspectral Imagery

by

Timothy Gibbs

Submitted to the

Chester F. Carlson Center for Imaging Science  
in partial fulfillment of the requirements  
for the Doctor of Philosophy Degree  
at the Rochester Institute of Technology

## Abstract

The detection and characterization of powdered contaminants is a challenging aspect of remote sensing in the longwave infrared spectral region. Powders are small in size (less than 45 microns in diameter) and exhibit weakened spectral features due to increased volume scattering, which is more prevalent as particle size decreases. Meanwhile, atmospheric effects such as wind, clouds, or shadowing cause large fluctuations in temperature of a surface on a microscale. This affects the ability of temperature emissivity separation algorithms to adequately derive a material's spectral emissivity from spectral radiance measurements. Hazardous powdered contaminants that are inaccessible need to be monitored from afar by using instruments of remote sensing. While spectral emissivity signatures alone can be useful, information about the physical properties and phenomenology of the material would be advantageous. Therefore, a method for estimating various physical properties including contaminant mass is presented. The proposed method relies on the principles of the Non-Conventional Exploitation Factors Data System (NEFDS) Contamination Model, which creates spectral reflectance mixtures based on two materials from its own database. Here, a three-step parameter inversion model was utilized that estimates several physical parameters to derive a contaminant mass from three spectral emissivity measurements. This information is then used to inject synthetic target mixtures into real airborne hyperspectral imagery from the Blue Heron LWIR sensor at pixel and sub-pixel levels. Target detection was performed on these images using the adaptive cosine/coherence estimator (ACE) with several types of target spectra. The target spectrum with the largest detection statistic

for each target pixel represents the best spectrum to detect its physical properties and informs the detection method. Results indicate that best performance is not always achieved when using the pure contaminant spectrum, but varies with level of contamination and pixel fill fraction. The inversion algorithm method was also applied to real targets in LWIR imagery and demonstrated the ability to extract contaminant mass from the data directly.

## Acknowledgements

We would like to acknowledge the Department of Energy for funding this research under grant DE-NA0002482, without whom this work would not be possible.

I would like to thank the four members of my committee for the extensive help they have provided to make this project successful. To my advisor Dave, thank you for reading all the terrible first drafts I wrote and giving me the opportunity to be a PhD student. To Chip, thank you for throwing me into the baptismal fire that is a research expedition and teaching me how to improve upon a data collection in the field. To Carl, thank you for knowing a solution to literally every problem I had with a collection, instrument or process. Also thank you for teaching me to question the validity of measurements and results found in conference and journal papers. To Vinny, thank you for your knowledge and expertise in material science and for your flexibility to accommodate me using all your cool instruments.

*This work is dedicated to my family, friends and cat Clarence for their support and love before, during and after this project was completed. Thank you and I love you all.*



*"We have to remember what's important in life: friends, waffles, and work. Or waffles, friends, work. But work has to come third." -Leslie Knope*



# Chapter 1

## Introduction

The field of remote sensing exists to discover and disseminate information about objects without physically interacting with them. Diverse in its application, remote sensing is ingrained into many of the day-to-day functions of society. Everyday citizens checking the weather do so using predictive weather modeling created with the help of data collected on airborne/spaceborne sensors. The NASA Landsat satellites let communities responsibly develop areas of land by mapping changes in land use and trends in land development. Intelligence gathering satellites allow the government to collect evidence of illicit behavior by foreign governments, drug cartels and terrorist organizations without endangering the lives of military personnel. The information gathered in each of these examples is only possible because of our ability to collect and manipulate remote sensing data.

Airborne remote sensing typically collects electromagnetic information in two ways. Active remote sensing systems exclusively collect energy returns after the surface is illuminated by an on board source. The most common form of active remote sensing is light detection and ranging (LIDAR). LIDAR uses light in the form of laser pulses to measure variable distances from the sensor to an object based on the time taken to return to the sensor. This data is combined with other remotely sensed data to create a three-dimensional topographic representation of surface characteristics. Passive remote sensing measures radiation that originates from the sun and is reflected off surfaces or is directly emitted from the observed object.

Visible and near infrared (VNIR + SWIR) electromagnetic radiation predominantly originates from the sun and is reflected back into the sensor from objects. Longwave infrared imagery (LWIR) comes directly as a result of an object's ambient temperature

while midwave infrared energy (MWIR) is a combination of both phenomena.

The region encompassed by a sensor pixel as projected onto the ground is unlikely to be uniform in its composition but rather a mixture of multiple materials that fall in the same governing space. Consider a pixel that is one square meter and falls upon the boundary of a baseball infield and the grassy outfield. From a physical standpoint there is clear separation of materials, which allows electromagnetic energy to independently reach the sensor pixel where energy from all governing materials will combine linearly.

On a smaller scale, pixels can also be represented as a collection of intimate mixtures between materials. While the grassy outfield in the previous example may appear nearly homogeneous in a large area pixel, upon closer inspection the grass may be comprised of different species of grass. Those grass blades also grow from earthy soil materials, all of which will interact with incoming solar electromagnetic radiation prior to reaching the sensor. Everything in the scene contributes to the final measured result.

Methods exist to decompose measured spectrum of a pixel into abundance fractions of constituent materials called spectral unmixing. An important application of spectral unmixing of intimate mixtures is to detect the presence of effluent powders from industrial processes. An effluent powder is another way of identifying a material that should not be present in a location. Often times, this refers to materials of a hazardous or dangerous nature. Companies and countries that hold similar materials typically place them in heavily guarded, inaccessible locations. Remote sensing provides a means to extract as much information as possible about the effluent material from a safe distance in order to assess its risk to the public.

Data processing algorithms assist in the breakdown of spectrally collected remote sensing information. Spectral unmixing algorithms are capable of determining a rough estimate of the composition of mixed pixels (assuming the mixture is a linear combination of materials), but at times this proves inadequate. It is important to be able to accurately assess the type and the amount of a contaminant present as quickly as possible in order to reduce any potential risks to the environment or people. Aerial imagery in conjunction with unmixing algorithms cannot currently derive an accurate amount of material present in a scene when intimately mixed for a variety of reasons to be described later. So how can we estimate physical characteristics of intimately mixed materials that fall within the bounds of a single pixel?

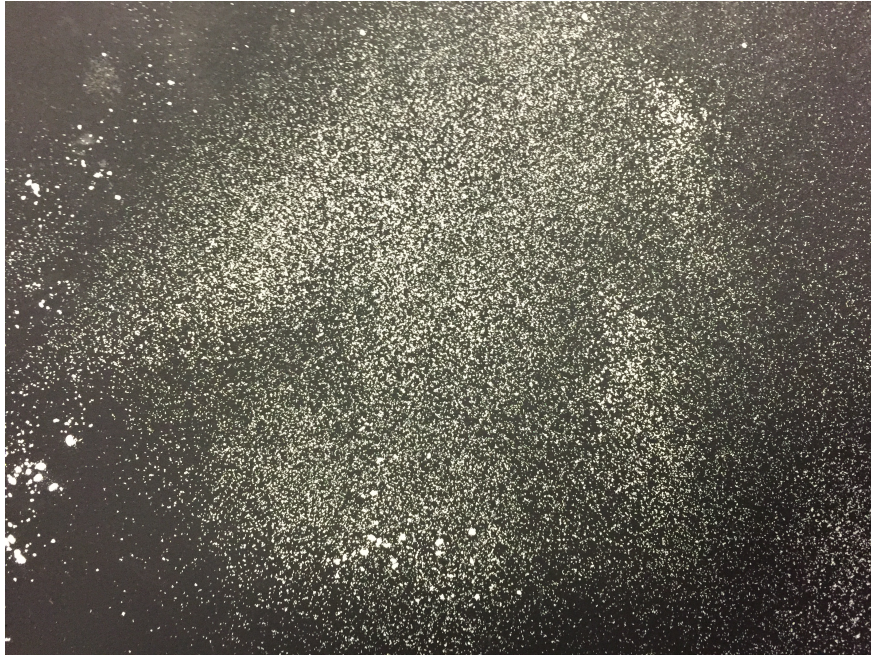


Figure 1.1: Fused Silica dust coating a painted aluminum surface.

## 1.1 Objectives

The goal of this research is to use spectrally mixed hemispherical directional reflectance (HDR) and spectral emissivity data to derive information regarding about the physical properties of an effluent contaminant from remotely sensed longwave infrared hyperspectral imagery. This information can then be used as a way to inform target detection algorithms on the fidelity of using different types of target signatures. A bullet point overview of this is provided below:

### 1.1.1 Tasks

1. Develop a framework for repeatable contamination tests
2. Measure mixtures of materials in laboratory and field settings
  - (a) Using simple mixtures of materials
  - (b) Using complex mixtures of materials



3. Estimate physical parameters of mixed materials from the field and potentially model mixture emissivity
4. Inject signatures into real airborne data in both full and sub pixel forms
5. Determine the minimum detectable amount of contaminant present for both full and sub-pixel mixtures as a function of target signature
6. Compare estimated contaminant mass present to actual mass present

A secondary goal of this project is to improve our detection algorithms by better understanding target phenomenology and the resulting spectra to be used in the detection scheme. Mixtures will be made and injected into real airborne hyperspectral scenes. These mixtures will vary in amount and pixel coverage (full pixel vs subpixel).

## 1.2 Scope

This research will examine estimating physical parameters from the defined region of longwave infrared spectra (8-14  $\mu m$ ). Midwave spectra are not considered as their electromagnetic energy distribution is too complex for the current model. In many cases, especially those not involving naturally occurring materials, directional changes between emissivity spectra can be assumed to be relatively small. As a result of instrument limitations and the overall challenge of the problem, off-nadir considerations were not thoroughly examined. There are already several unresolved potential sources of error in measuring mixture emissivities and estimating physical masses of effluent materials on surfaces. Unless more are rectified, noticeable differences in angular mixture measurements may be the result of a summation of errors and not true phenomenology. This is especially true for intimate mixture cases, where the contaminating material is likely sparsely coating the surface.

## 1.3 Overview

In Chapter 2, a robust discussion of remotely sensed data in the longwave infrared will occur. Longwave infrared imagery was chosen for this study as good imagery can be collected regardless of time of day and many materials have strong identifying features in this spectral range. While great advancements have been made in analysis of longwave

infrared imagery, it is often ignored as a viable alternative to VNIR and SWIR for its complex sensor designs.

In Chapter 3, the Non-Conventional Exploitations Factors Data System (NEFDS) contamination model will be discussed in great detail. This model uses some principles of the Hapke model to create spectral emissivity for mixtures of differing levels. The NEFDS Contamination Model is the basis for the derived algorithm responsible for estimating mixture contaminant amounts. This chapter will also briefly look at  $\mu$ DIRSIG, a first principles based simulation tool as a potential method to create simulated mixtures with well defined properties.

Physical parameters such as coverage density are computed from the NEFDS derived three-step parameter inversion model and the derived total contaminant mass from the results is shown. Estimated parameter values will be derived from real measurements made in a laboratory and field setting. Improvements to the model will be examined, specifically if the contaminant extinction cross section can be directly measured to reduce its impact on estimated density amounts.

A discussion of the methodology of this project is presented in Chapter 4. The three-step parameter inversion model created from the NEFDS contamination model is explained. Physical parameters such as coverage density and contaminant mass are estimated for both measured and modeled data. An approach to injecting the mixture signatures into real airborne longwave hyperspectral scenes for further analysis is explored. Target detection algorithms performed on these synthetic images will help determine the conditions for which each amount of material can be detected. The smallest detectable quantity of contaminant will be considered the minimum detectable quantity (MDQ), but will vary based on density, pixel coverage and type of target signature used.

A number of results for the parameter inversion model are presented in Chapter 5. Several solid powder contaminants were chosen as well as a number of substrate surfaces for the experiments. Basic material combinations were initially created as a proof of concept to the model. Complexity of mixtures is increased by combining materials with less pronounced signatures and by using more complicated substrate materials. The results are presented as individual parameter estimates for mixtures as well as reconstructed reflectance and emissivity signatures. Future work will be proposed at the end that considers the current status of the project and what could be accomplished with additional efforts.



## Chapter 2

# Background

From a remote sensing perspective, the collection and analysis of electromagnetic radiation data is paramount to understanding the characteristics of a material or mixture of materials in a scene. While mixtures are inherently more complicated to understand than a single material collection, all types of data have unique complexities. A single material may appear different than expected due to interactions the surrounding environment and atmosphere have with that material. Furthermore, for some types of data like longwave infrared radiation, temperature retrieval is required along with collected radiance data to calculate spectral emissivity. Before any data can be parsed and analyzed, a thorough understanding of electromagnetic radiation and its impacts on materials needs to occur.

### 2.1 Remote Sensing

As previously mentioned, remote sensing enables us to learn information about an object without ever coming into physical contact with that object. Light waves are collected by instruments and image analysts dissect collected data to discover useful information about the scene. Radiometry provides an adequate way to study the nature of light.

All electromagnetic energy travels at the speed of light  $c$  in a vacuum, which is defined as

$$c = \lambda\nu, \tag{2.1}$$

where speed is comprised of the frequency ( $\nu$ ) of the wave peaks measured in Hertz and the wavelength of light ( $\lambda$ ) [1]. The frequency of light is determined by its source.

Monochromatic light has a single frequency component where as polychromatic light contains a spectrum of radiation components. No theoretical limit to the frequency of light exists, therefore electromagnetic radiation waves may have very large frequencies like radio waves (  $10^4$ m) or very small like gamma ray bursts (  $10^{-16}$ m).

According to quantum theory, energy travels as quanta carried on particles called photons. Energy is based on the wavelength of light that is being considered and is defined as

$$q = \frac{hc}{\lambda}, \quad (2.2)$$

where  $h$  is Planck's constant, and  $q$  is the total energy at the specified wavelength. Most remote sensing instruments and applications measure quanta from the 0.4 - 14.0  $\mu m$  region. The two largest sources of quanta, terrestrial radiation and solar radiation, have the biggest impact in this spectral range.

With this newly defined spectral range, Earth based passive sensor reaching electromagnetic energy originates primarily from two types of sources. The visible and near infrared (VNIR-SWIR) portion of light is dominated by solar energy that reflects off of terrestrial objects towards the sensor while the longwave infrared (LWIR) spectrum contains emitted energy that is associated with the temperature of non-solar objects. In the region between 3-5  $\mu m$  (midwave infrared radiation), both aspects occur in significant amounts.

## 2.2 Solar Reflected Radiation

Solar reflected radiance is calculated by summing electromagnetic radiation originating from the sun that reflects off of materials into a passive sensor. The dominant portion of the electromagnetic spectrum for solar energy occurs in the visible and near infrared.

Depending on the path taken, a photon may interact with many objects before reaching the sensor (downwelling radiance, adjacency effects) or reflect off the target directly (direct radiance). Photons sometimes even fail to interact with the target prior to reaching the sensor (upwelling). Total observed solar radiation ( $L_{obs}$ ) is the combination of each energy path described.

In practice, to determine the surface characteristics, Solar radiance is rearranged and manipulated to solve for spectral reflectance ( $r(\lambda)$ ) which is better for material specificity. If conditions are favorable, it is possible to eliminate some components of

this equation by understanding the surroundings. For example (as described below) the background radiance term  $((1 - F)L_{b,s,\lambda}r_d(\lambda))$  incorporates a sky fraction ( $F$ ) that is defined by the proportion of hemisphere visible from the measurement location. When the entire hemisphere is visible, the background term is completely eliminated.

## 2.3 Infrared Radiation

Unlike solar radiation, infrared radiation is not a measurement of the reflected solar energy, but the radiation that an object directly emits. Any object with a temperature above absolute zero and that is not a perfect reflector, including atmospheric matter will radiate energy. If the temperature the object emits at is roughly the temperature of the Earth, emitted energy will be present in the longwave infrared spectral region. While similar to reflected solar energy, it is more difficult to conceptualize longwave radiation than light originating from the visible spectrum.

Given that objects emit light based on their temperature, there should be a spectral range where emitted light plays a dominant role for Earth objects. Using Wein's Displacement Law, a spectral emission peak can be determined for an object at temperature  $T$  and is written as

$$\lambda = \frac{2898}{T}. \quad (2.3)$$

The numerator of Equation 2.3 represents the Wein displacement constant 'A' and is found by manipulating Planck's Law. Since the sun has a known temperature of approximately 5778 K, its peak emission wavelength hovers around 0.5 microns, or approximately green visible light. An object on Earth will have a temperature around 300 K, which results in a spectral peak of approximately 10  $\mu m$ . For an object on Earth to emit even a small amount of visible light, its temperature needs to reach at least 500 Kelvin which is significantly higher than most terrestrial surfaces.

With this in mind, an idealized spectral range to examine radiation generated by objects found on Earth will be the longwave infrared spectrum (8-14  $\mu m$ ). Much like radiance in the visible and near infrared, multiple sources contribute to longwave infrared radiance. Following the notation of Schott (2007), the radiance at a sensor measuring in the LWIR is written as

$$L = L_D + L_E + L_H + L_F \quad (2.4)$$

where  $L_D$  is the direct radiating term,  $L_E$  is the downwelling radiance,  $L_H$  represents

any existing background effects, and  $L_F$  represents the upwelling component. Each path is visualized in Figure 2.1.

Breaking down Equation 2.4 further, it can be seen that there are many different contributions to each respective term. The comprehensive version of the thermal radiance equation is written as

$$L(\lambda) = [\epsilon(\lambda)L_{BB}(\lambda, T) + FE_d(\epsilon, \lambda)\frac{r_d(\lambda)}{\pi} + (1 - F)(L_b(\epsilon, \lambda))r_d(\lambda)]\tau_2(\lambda) + L_u(\epsilon, \lambda), \quad (2.5)$$

where each term in equation 2.5 corresponds to the respective term written in Equation 2.4. The direct surface radiance is a combination of spectral emissivity ( $\epsilon(\lambda)$ ), black-body radiance ( $L_{BB}(\lambda, T)$ ) at a given temperature and the transmission through the atmosphere to the sensor ( $\tau(\lambda)$ ). The downwelling radiance is comprised of the visible sky fraction ( $F$ ), downwelling irradiance ( $E_d(\epsilon, \lambda)$ ), and reflectance of downwelling irradiance  $r_d(\lambda)$ . Background radiance  $L_b(\epsilon, \lambda)$  is also modulated by the sky fraction, atmospheric transmission and reflectance. Finally the upwelling radiance ( $L_u(\epsilon, \lambda)$ ) is the final term.

Equation 2.5 comprehensively examines the numerous impacts of the surrounding environment on a sensor's observed radiance field. Various mitigating factors to the observed radiance include the material optical properties, background radiance, atmospheric effects and various combinations of each. Ground based instruments are close enough to eliminate any atmospheric effects while placing the instrument far from large objects, such as buildings or trees, eliminates any sky occlusions. For this observation geometry, the sensor reaching radiance is

$$L_{obs}(\lambda) = \epsilon(\lambda)L_{BB}(\lambda, T) + (1 - \epsilon(\lambda))L_d(\lambda) \quad (2.6)$$

Surface emissivity is easily derived by rearranging Equation 2.6 for the emissivity parameter

$$\epsilon(\lambda) = \frac{L_{obs}(\lambda) - L_d(\lambda)}{L_{BB}(\lambda, T_s) - L_d(\lambda)}. \quad (2.7)$$

The resulting spectral emissivity equation leaves a ratio between object and black-body radiance modulated by reducing both the numerator and denominator by the downwelling component. When downwelling from the atmosphere approaches the target temperature, the numerator forces Equation 2.7 to be extremely small relative to its

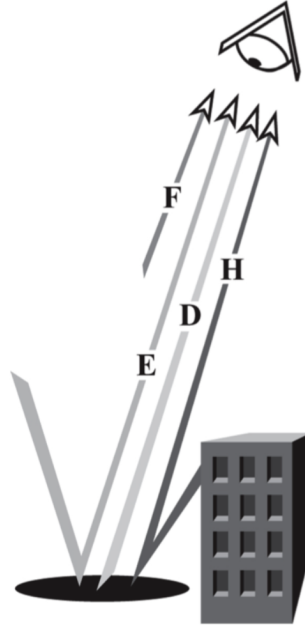


Figure 2.1: Visual representation of various paths photons travel to reach a sensor in the longwave infrared. Taken from Schott (1997), Figure 3.3.

associated denominator. This results in noise dominated emissivity values.

An easy way to reduce the instability associated with poor relative downwelling radiance is to collect when downwelling lacks significant impact. This occurs during cloud free periods with low humidity (low water vapor content). Measurement collection during early morning or early evening time periods helps because the sky is relatively cool compared to the ground.

## 2.4 Electromagnetic Radiation Collection Geometry

The geometry behind measuring energy from the VNIR/SWIR and LWIR is very similar. Visible light acts as in Figure 2.2, where an illuminating light source (typically the sun), strikes a surface at two reference angles. The incident zenith angle( $\phi_i$ ) describes the incoming radiation declination angle from an imaginary z-axis above the incident



surface, while  $\theta_i$  represents the rotational angle from the planar axes ( $x, y$ ). Visible light then reflects off the surface in the direction of the symbols with a  $r$  subscripts, which indicate reflected angles of the same nature as the incident angles.

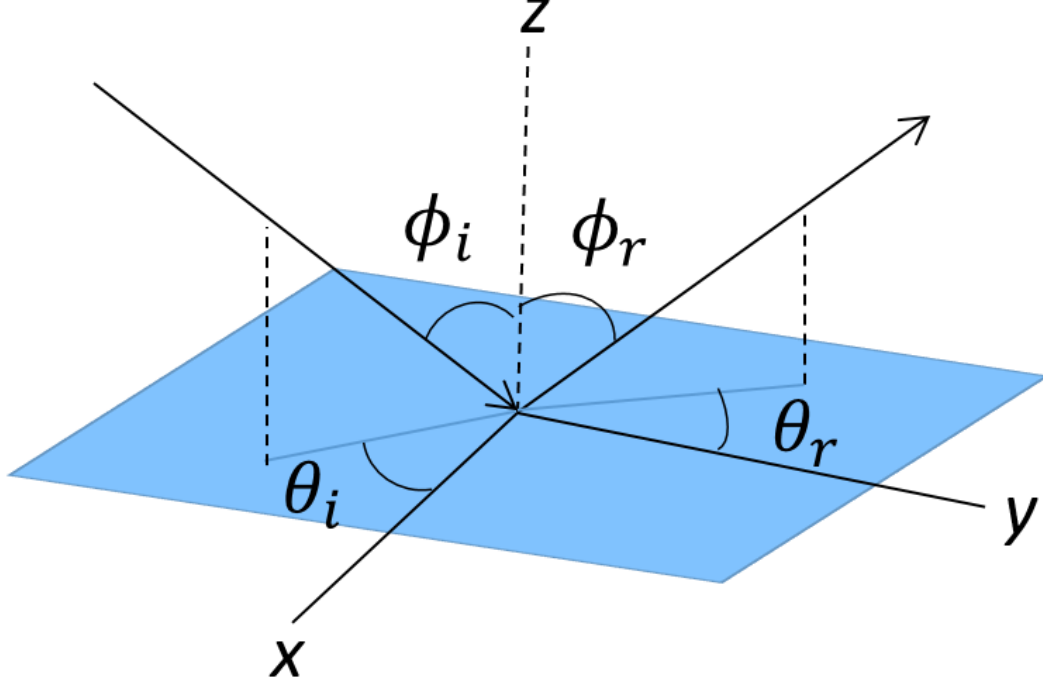


Figure 2.2: Geometry of the a surface receiving incident energy at angles specified with an ‘i’ subscripts and reflected in a direction specified by ‘r’ subscript angles.

Since the reflected electromagnetic energy can travel in any direction across the sky hemisphere above the surface, a measure of this direction scatter should be created. This measurement is defined as the Bidirectional Reflectance Distribution Function (BRDF) and can appear in many forms. An ideal specular reflection appears at the leftmost image in Figure 2.3 where incoming light is reflected in a concentrated singular direction. The closest example of such an event is a laser pointer off a flat mirrored surface. An ideal diffuse reflection will reflect light equally in all directions off a surface, which is best represented by the rightmost image of Figure 2.3. Diffuse surfaces such as flat paints or very rough surfaces will have very diffuse characteristics. Most materials fall somewhere in between these ideal situations similar to the middle image in Figure 2.3. A

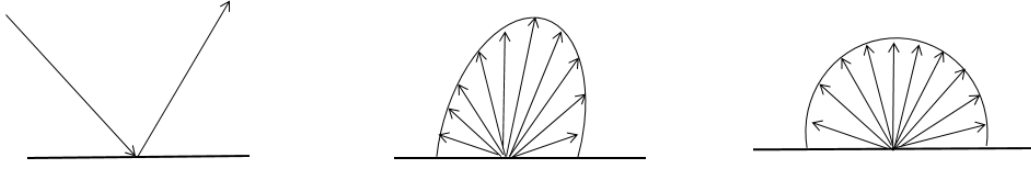


Figure 2.3: Three cases of a scattering by electromagnetic energy. The left-most image represents the ideal specular case and the right-most image represents the ideal diffuse case for scattering. The center image is representative of most objects, where scattering is fairly diffuse, with an low intensity specular lobe.

directionally diffuse surface has a low intensity directional lobe, but is relatively evenly spread across the hemisphere.

In LWIR spectral region emissivity, not reflectance is the dominating factor. While electromagnetic energy from the sun and surrounding environment becomes incident upon the surface, it is the surface itself that emits energy. Directional spectral emissivity combines the properties of emitted energy with these directional components and appears similar to the center and right images of Figure 2.3. With the exception of specific features addressed later, LWIR measurements do not have significant directional variation.

## 2.5 Material Properties

When light reaches a surface, it can either reflect off the surface, be transmitted through the surface or be absorbed by that surface. Since energy is conserved, light will either be reflected, absorbed or transmitted with each having wavelength dependencies. This means the total of the three properties must be equal to the total amount of irradiance reaching that surface. Therefore each interaction can be represented as a ratio (or an efficiency) that sums to one,

$$\alpha(\lambda) + \tau(\lambda) + r(\lambda) = 1 \quad (2.8)$$

where  $\alpha(\lambda)$  is the wavelength dependent absorptance,  $\tau(\lambda)$  is the transmittance, and  $r(\lambda)$  is the reflectance.

Transmittance is the ratio of electromagnetic energy that passes through a surface

$(M_\tau(\lambda))$  to the amount that is incident upon that surface  $(E_i(\lambda))$ . Sunglasses represent a practical example of how to calculate transmittance. Sunglasses are used when sunlight or sun glare visually overwhelms a person's sight. When placed over the eyes, the amount of light reaching the eye is lessened. The ratio of the amount of light reaching their eyes to the amount reaching the sunglasses is a practical example of transmittance. Transmittance is calculated as

$$\tau(\lambda) = \frac{M_\tau(\lambda)}{E_i(\lambda)}. \quad (2.9)$$

Reflectance is the ratio of the spectral exitance reflected off the surface  $(M_r)$  to the incoming irradiance on that surface  $(E_i)$ . This differs slightly from a material's reflectivity in that the reflectivity is a material's capability to reflect incident flux into the entire hemisphere over the material. Spectral sensors in the visible and near infrared most commonly use reflectance to identify materials. The reflectance of a surface is calculated as

$$r(\lambda) = \frac{M_r(\lambda)}{E_i(\lambda)}. \quad (2.10)$$

Finally, when the incident flux is not reflected or transmitted, it is absorbed by the object. The absorptance is represented by the ratio of flux energy that has been converted into another energy by the material  $(M_\alpha(\lambda))$  to the incident flux and is written as

$$\alpha(\lambda) = \frac{M_\alpha(\lambda)}{E_i(\lambda)}. \quad (2.11)$$

One parameter not directly seen in any of the above equations is the emissivity of the material. The spectral radiance of an object or material is directly dependent on the object's temperature. Because the energy source is the object itself and not impinged upon by another source, it is not part of Equation 2.8. Emissivity is a ratio between the amount of energy radiated by the object or material  $(M_\epsilon(\lambda))$  to the amount radiated by a blackbody at the same temperature, written as

$$\epsilon(\lambda) = \frac{M_\epsilon(\lambda)}{M_{BB}(\lambda)}. \quad (2.12)$$

Using the principles of thermodynamics and Kirkhoff's law, the object emissivity can be incorporated into Equation 2.8 without violating conservation of energy laws. Con-

sider an object that is placed in an isothermal enclosure. Over time, the enclosure and object will exchange energy and reach a temperature equilibrium according to the second law of thermodynamics. This implies, as found in Kirkhoff's law, that the absorbed energy and emitted energy of blackbodies are essentially equivalent parameters,

$$\alpha = \epsilon. \quad (2.13)$$

This leads to a modification of Equation 2.8 to appear as

$$\epsilon(\lambda) + \tau(\lambda) + r(\lambda) = 1 \quad (2.14)$$

and for opaque objects where little energy is transmitted through the material,

$$\epsilon(\lambda) + r(\lambda) = 1. \quad (2.15)$$

Given that the longwave infrared spectral region is where emissivity dominates, it is important to understand how to find the spectral exitance for blackbodies. Planck's Radiation Law calculates the exitance based on the vibrational energy state between atoms. The equation used to calculate exitance for a given wavelength and temperature is given by the Planck equation,

$$M_\lambda(T) = \frac{2\pi hc^2}{\lambda^5 (e^{\frac{hc}{\lambda kT}} - 1)} \quad (2.16)$$

In this case,  $k$  denotes the Boltzmann gas constant,  $h$  is the Planck constant,  $c$  is the speed of light in a vacuum,  $\lambda$  is the wavelength and  $T$  represents the object surface temperature in Kelvin.

## 2.6 Temperature Emissivity Separation

In the visible and near infrared, spectral reflectance is ascertained through rearranging components of spectral radiance (see Equation 2.4) to retrieve a solution assuming atmospheric effects are perfectly known or can be modeled using a simulation tool such as MODTRAN. Solving for reflectance is a well posed problem resulting in a unique answer. In the longwave infrared regime, both emissivity and temperature are unknowns. Temperature as well as an emissivity at each wavelength affect the observed spectral radiance of the scene, resulting in a problem with  $n$  measurements, but  $n + 1$  unknowns.

Manipulation of Equation 2.6 along with constraining the number of terms results in an equation for emissivity seen in Equation 2.7. This still leaves an ill posed problem of solving emissivity for ' $n$ ' wavelengths as well as temperature. The process of deriving all the unknowns for a spectral image is called Temperature Emissivity Separation and will be described below.

### 2.6.1 Fixed Window Technique

Numerous TES algorithms exist to extract spectral emissivity and temperature. A commonly used method for fourier transform infrared spectrometer (FTIR) measurements called the fixed window technique determines the temperature that constructs the smoothest spectral emissivity within the user defined window. An algorithm was developed for this method was written in IDL by Carl Salvaggio and is based on work by Horton et al (1998) and Bower (1998). This method examines the average of the squared second derivative of each spectral emissivity at all examined temperatures within set boundary conditions. The average squared magnitudes of the window for each temperature are compared, with the lowest value corresponding to the most likely surface temperature. The lowest value (i.e. the smoothest) is the best because the first derivative denotes the function slope. Small second derivatives demonstrate small changes in the slope, therefore indicating the derived emissivity curve is very smooth. Any size spectral window can be selected over any portion of the longwave infrared spectrum. A poor window selection where the emissivity is not inherently smooth will lead to large estimation errors.

In Figures 2.4 and 2.5 an example of the process behind the fixed window technique is shown for Quartz sand. Figure 2.4 shows the emissivity between 306 and 316 Kelvin at 1 degree intervals and highlights the best estimate of temperature at 312 Kelvin in red. Figure 2.5 focuses on the window where spectral smoothness was evaluated. A fixed window was selected in the range of 8.12-8.6  $\mu\text{m}$  in this example due to a strong well known absorption feature in quartz. A spectral window of any size and location can be used, but selecting the location of the best absorption feature is ideal.

Another similar technique uses two fixed windows to find the correct temperature and spectral emissivity [6]. The method is exactly the same, however the aggregate of the two windows is considered rather than one window. This is useful when the material is known and has two distinctly strong absorption features to consider. In cases where two strong absorption features do not exist or where only one feature is well

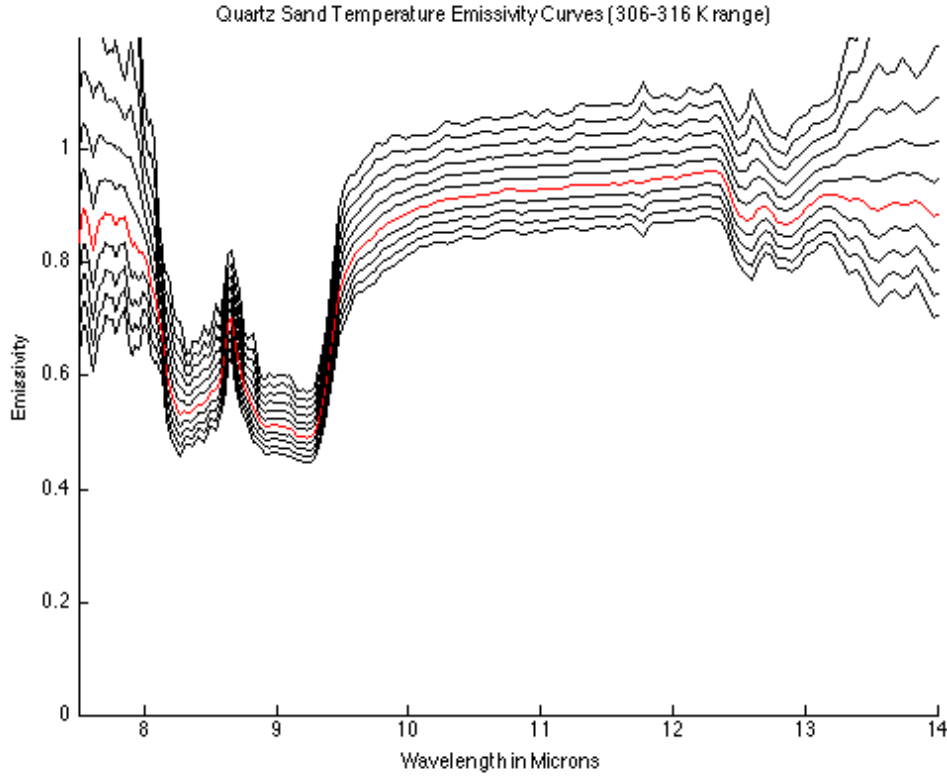


Figure 2.4: Derived emissivity spectra of quartz sand for temperatures between 306 and 316 K. The red line represents the best emissivity estimate and its temperature based on spectral smoothness within a fixed window.

characterized, this method is not ideal.

### 2.6.2 Moving Window Technique

Some attempts have been made by Darling (2003) and others to incorporate a moving spectral window of fixed or varying size. In theory, this would find the ideal window location and size to calculate the smoothest section of the emissivity spectra. In practice, there could be millions of combinations tested to find the smoothest sized window, exponentially increasing computation time. The available python code for this method had significant instabilities as well, and therefore will not be further examined.

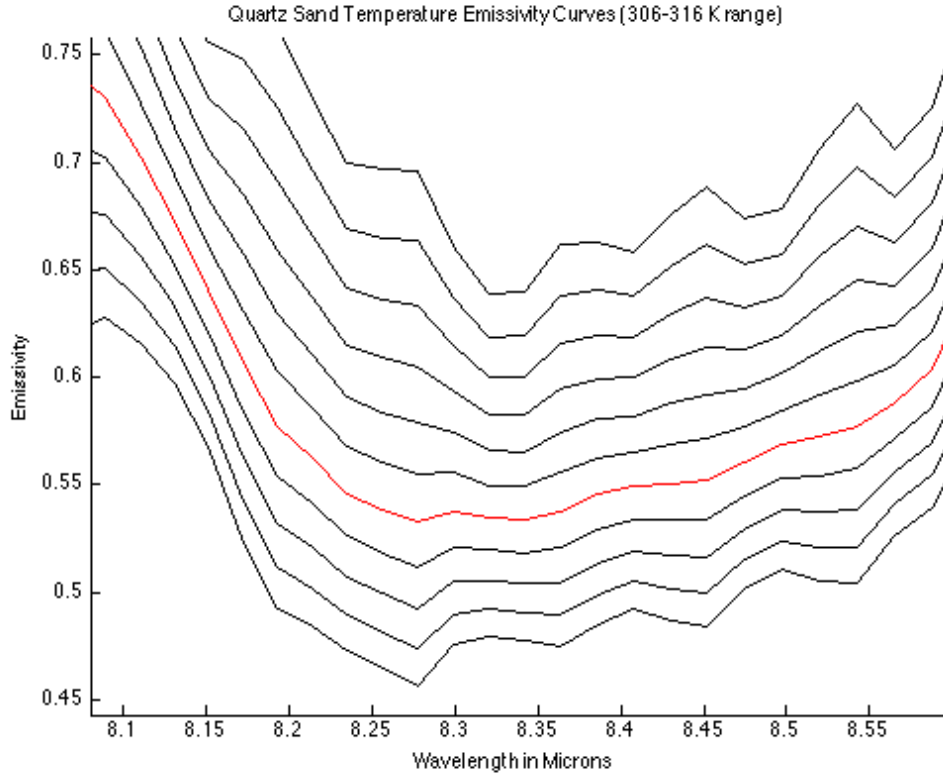


Figure 2.5: Derived emissivity for the user defined fixed spectral window from 8.12-8.6  $\mu m$ . At 312 Kelvin, the emissivity has the smoothest features within the fixed window and therefore represents the best estimate for emissivity.

### 2.6.3 Known Temperature

The final method for temperature emissivity separation of a single spectrum is to simply use a measured infrared temperature of the surface at the time of collection. This directly solves for spectral emissivity making it unnecessary to perform temperature emissivity separation. It is most likely that a known measured temperature is unavailable for any airborne data, but will be available for ground measured data. In practice, this method often does not capture the true temperature at the time of measurement. An Exergen contact probe thermometer needs to be in contact with the material to find its infrared temperature, but as it contacts the material, it shadows it from the sun, affecting the radiance measurement. Having the ground temperature as reference is the best case

scenario for a measurement as truth data is better than estimation in all cases.

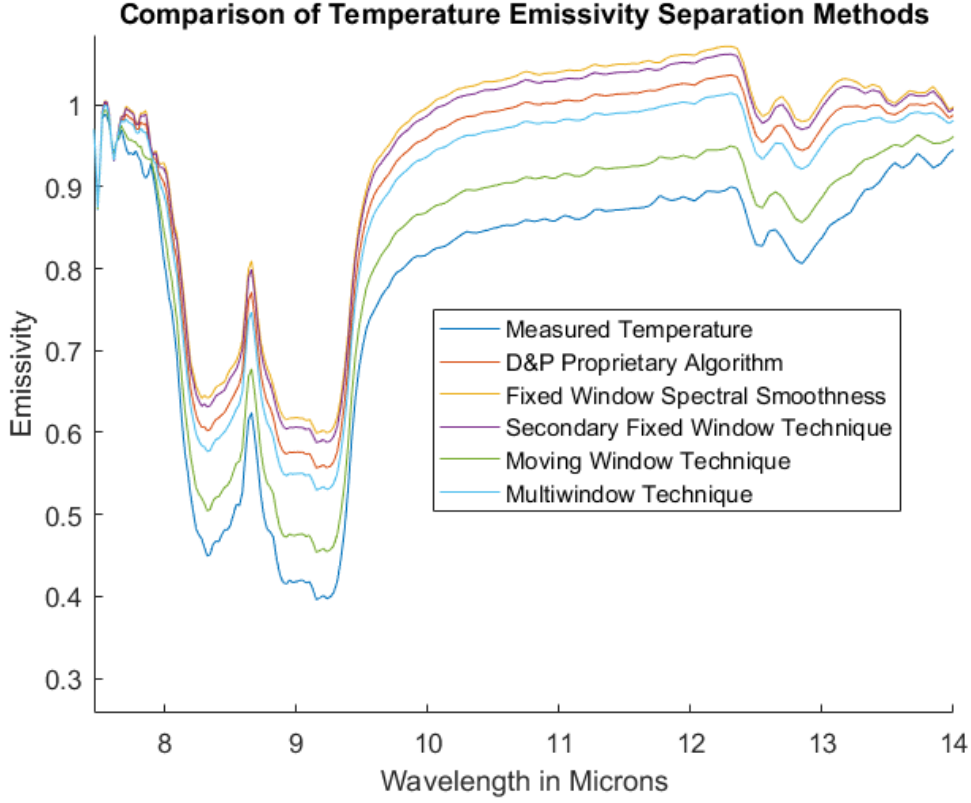


Figure 2.6: A comparison of spectral emissivity derivation from various temperature emissivity separation methods.

As seen in Figure 2.6, the selection of the proper temperature emissivity separation method can affect the resulting spectral emissivity in the LWIR by significant margins. For this example, the fixed window technique has overestimated the signature by about 0.1. Even with a measured known temperature, shadowing of the surface by the thermometer caused underestimation of the spectral emissivity by a small margin.

#### 2.6.4 Full Scene Methods

While several TES methods have been discussed, all examine single pixel output spectra data collected from a non-imaging instrument such as the Designs and Prototypes FTIR. Airborne imagery typically consists of an array of pixels which each have unique spectral



characteristics. Due to the finite pixel size of airborne sensor arrays, pixels often capture light from multiple materials, resulting in spectral mixing. Ground truth (also called reference data) is often not available for airborne imagery and alternative methods for temperature retrieval are necessary.

Unlike ground based measurements, airborne LWIR imagery must also consider path radiance contributions when performing a temperature retrieval process. A standard method for removing atmospheric effects seen in imagery uses the in-scene atmospheric compensation (ISAC) or something similar [4].

Intuition would indicate the best approach to remove atmospheric effects is to measure the physical state of the atmosphere at the time of collection and calculate atmospheric parameters using a radiative transfer model such as MODTRAN [7]. This is not realistic as radiosonde data are rarely available at the site or time of collection. Spectral misregistration between measured and modeled data may amplify the atmospheric effects making the problem significantly worse.

A more realistic approach is to use the hyperspectral data itself. The In-Scene approach to atmospheric compensation (often abbreviated ISAC) determines relative atmospheric parameters like transmissivity and path radiance using only the actual data collected (Young (2002)) which focuses on two main assumptions:

1. Atmosphere is homogeneous throughout the scene
2. A population of near blackbody materials with a range of temperatures is present in the scene and encompass entire pixels

When performing ISAC, all pixels help to estimate atmospheric parameters. First, they are converted into brightness temperature by inverting Planck's equation [9, 7, 8]

$$T_B(L_{bb}, \lambda) = \frac{C_2}{\lambda \ln\left(\frac{C_1}{\pi * \lambda^5 * L_{bb}} + 1\right)} \quad (2.17)$$

where

$$C_1 = 2\pi h c^2 \quad (2.18)$$

$$C_2 = \frac{hc}{k} \quad (2.19)$$

The variables  $h$ ,  $c$ , and  $k$  are the Planck constant, the speed of light and the Boltzmann constant [9, 7, 8]. Temperature is not a function of wavelength, however, so

after calculating all the brightness temperature values, each pixel's highest temperature wavelength is determined. The wavelength band with the most maximum brightness temperature pixels denotes the ideal wavelength for estimating the surface pixel temperature. All maximum brightness temperature pixels in the ideal wavelength are used to create a scatter plot over the full spectral range of the image such as the one seen in Figure 2.7. Measured at-sensor spectral radiance is plotted against the spectral radiance of the blackbody to form a scatter plot.

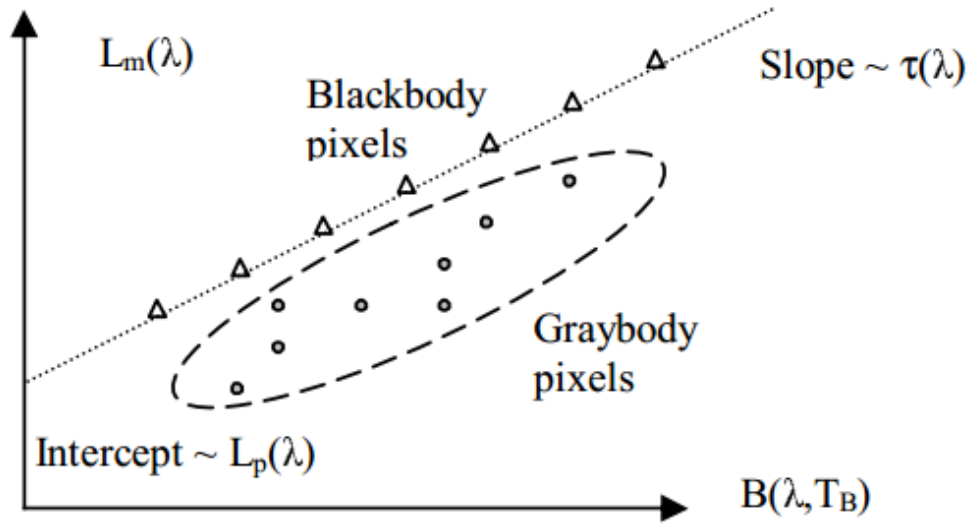


Figure 2.7: A recreation of a standard scatter plot to estimate atmospheric parameters. Plot represents the observed vs Planck radiance for each wavelength. Image taken from Figure 3 of Borel (2003).

A regression line is determined using the highest value from each data bin [7]. The slope of this regression line represents the atmospheric transmission while the Y-intercept represents the path (upwelling) radiance contribution. These values are not perfect as they represent the emissivity relative to the scene as a whole which is unknown. Fitting to the maximum found in the scatter plot will ensure that the values found for transmission and upwelling radiance are the best possible fit given the data set. Once full scenes have been adjusted for atmospheric effects, the necessary data processing can occur.

## 2.7 Material Mixtures and Contaminants

In airborne imagery, pixels tend to fall across more than one single material [10] depending on the sensor ground sample distance (GSD) and instantaneous field of view (IFOV). In some cases, a mixture may sit on the border between two areas, such as on a baseball infield where grass and dirt converge. Mixtures like these are known as areal mixtures. In the absence of multiple scattering between materials, they create a linear combination of radiance received by each material as a result of the spatial separation between the materials. It is more likely that materials combine such that spatial segregation is not present and separating each material's spectral influence becomes more convoluted. These types of mixtures, called intimate mixtures, pose issues due to non-linearities from scattering between particles.

Intimate mixtures often combine a naturally found surface with a rarely found contaminating material. A contaminant is considered any material that at detectable levels, has an effect on the spectral characteristics of a measurement. The contaminating material may be airborne like gases hovering over a factory, or a liquid like oil floating on a water body surface or embedded in the soil. There are profound differences between the three states of matter and how they affect a spectral signature.

### 2.7.1 Gaseous Contaminants

Gaseous contaminants differ greatly from their liquid and solid counterparts in that they are airborne. Being airborne adds complexities in the phenomenology that are not seen in ground based contaminants. The resulting detected signature is a complicated synthesis of the atmosphere, the materials beneath (or behind if viewed horizontally) the gaseous plume assuming the plume is optically thin, temperature contrasts between the ground and plume as well as the density of the gas in that location [11]. Small effects like clutter can have a big effect on plumes. Background clutter has the capability to completely obscure the plume in a scene [12].

While molecules in equilibrium have several types of energy, molecules only create features from molecular vibrations in the longwave infrared [11, 13]. Energy quantization occurs when molecules emit or absorb energy, changing the dipole direction. Because gaseous effluents are airborne, each particle scatters light independently, whereas liquids and solids are tightly packed in comparison and can scatter as if a single particle.

In the example of airborne ammonia ( $\text{NH}_3$ ), a number of narrow absorption features exist when electromagnetic energy creates an overtone, specifically in the  $7.5 \mu\text{m}$  region.

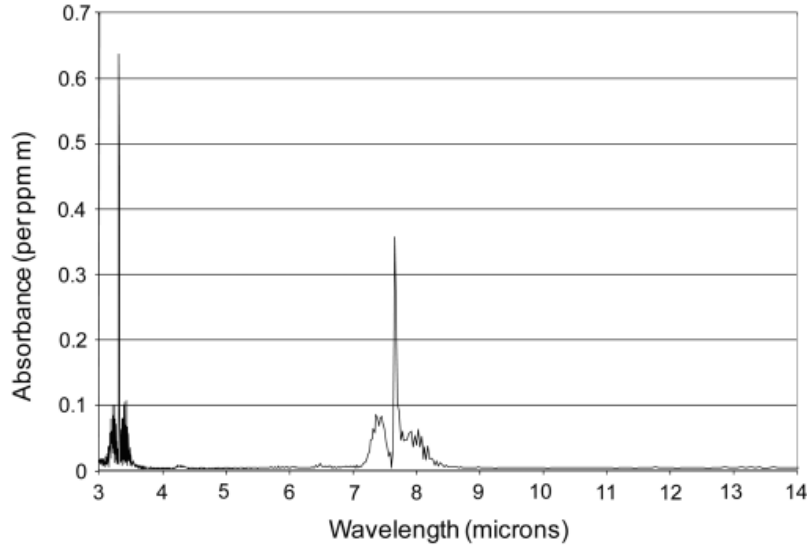


Figure 2.8: Gas absorption spectra of  $NH_3$  from Eismann, Figure 4.18.

Narrow absorption features are commonplace in gas spectra because gas plumes are not cohesive [11]. In reality, detecting narrow absorption features in the measured data does not happen as cleanly as in Figure 2.8 due to contributions by the atmosphere and ground. Often times, identifying a gas plume spectrum requires the residual background spectra from the scene to be extracted [14].

### 2.7.2 Liquid Contaminants

Liquid contaminants have cohesion, but present additional challenges not seen in gases. When gases such as water vapor cool below the dew point temperature, they condense transforming into liquid dew formations on solid surfaces [15]. When dew forms on the surface of a vehicle, modeling by Reinov (2009) suggests that the surface temperature of vehicles changes up to 8° Kelvin in a situation with dew present as compared to when the dew is not present. This particular case highlights the ability of a liquid to act as a thermal heat sink.

Because liquids have no defined shape, they can appear on solid surfaces or in mixtures with different liquids. As a surface contaminant, liquids are best understood when applied as a spray. Archer (2014) showed that several liquids could be well reproduced in simulation tools when they were considered a thin film on a flat surfaces.

Physics based modeling like  $\mu$ DIRSIG tend to over compensate for the effects of liquids on surfaces. In Kerekes (2008), a sample of quartz sand was separated by particle size and coated with SF96 oil. Restrahlen features were nearly eliminated with the presence of the oil, but models completely flatten the spectra of the mixture [17].

### 2.7.3 Solid Materials Properties

Remote sensing has a storied history of collecting imagery of solids using longwave infrared radiation instruments. Instruments like the Airborne Hyperspectral Imager (AHI) have been placed in airborne vehicles such as helicopters to measure disturbed soils in order to find items such as land mines [5]. Others have used mineral features to do mining and mineral identification work [18].

Some natural materials like soils have distinct restrahlen features that help define them in the thermal region [19]. When a material's ionic bonds vibrate, the resulting spectral emissivity contains deep absorption regions called restrahlen bands. Most commonly, they are found in materials containing quartz and can have different shapes depending on the soil composition. Kerekes (2013) demonstrated that when adding SF96 contaminant to a quartz sand, the restrahlen features lessened considerably. This is likely due to an increase in volume scattering from cohesion between the particles with the liquid oil.

Restrahlen features have varying effects for materials when viewed off-nadir. In Figure 2.9, clear magnitude changes in emissivity occur at the absorption features from 8.1-8.6  $\mu m$ . In Figure 2.10, a non-quartz material is measured and no significant emissivity change occurs when the adding angular dependencies.

Another thermal identifier besides Restrahlen bands are Christensen features. These occur when the real portion of the index of refraction of a material undergoes anomalous dispersion [20]. This is when rapid changes in the refractive index of the material approach the refractive index of air at a specified wavelength [21, 22, 23]. Christensen features easily allow radiation to transmit through a material because scattering and absorption are significantly reduced [22]. Both of these features make them ideal for identifying a material. Christiansen features can also be used in situations where the material is known, but the spectrum is slightly bias. Quartz sand is an example where the 7.41  $\mu m$  band should match that of air, but in many cases, the measured spectrum is slightly off from this value.

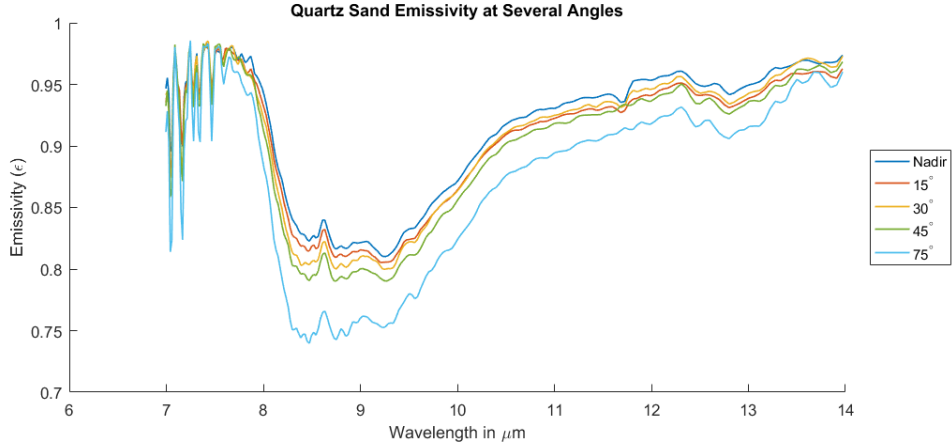


Figure 2.9: Change in emissivity given angle for Quartz sand. Measurements taken at Sand Mountain Recreation Area in Sand Mountain, Nevada.

## 2.8 Particle Size Considerations

While gaseous effluents have no well-defined volume and liquids act as thin films on surfaces, solids materialize in several different constructs. They can form as a lattice of bonded particles, as a loose conglomerate of diversely sized particles, or contain a homogeneously sized set of particles. Despite consisting of the same material, each can yield wildly different spectra. Particle size represents a significant influencing factor to why spectral emissivity measurements differ between each group.

A distinction must be made between the use of the terms particle and grain when describing a solid material. Grains are single crystal structures within a material layer while particles are comprised of at least two or more crystals in an agglomerate structure. This means that a particle must be made up of at least two or more grains.

In Figure 2.11, the spectral reflectivity of three types of quartz are shown, keeping in mind spectral reflectivity is  $1 - \epsilon(\lambda)$  according to Kirchoff's law [10]. The solid line represents a single polished piece of quartz, the dashed line contains only loose coarse particles and the smallest dashed lines represent loose finer particle quartz. In the spectral region containing the two main restrahlen features, it is clear that as the material particle size distribution changes, the contrast in these bands decreases. Volume scattering largely contributes to this precipitous drop in the restrahlen features [21].

Volume scattering occurs when electromagnetic energy passes through a material

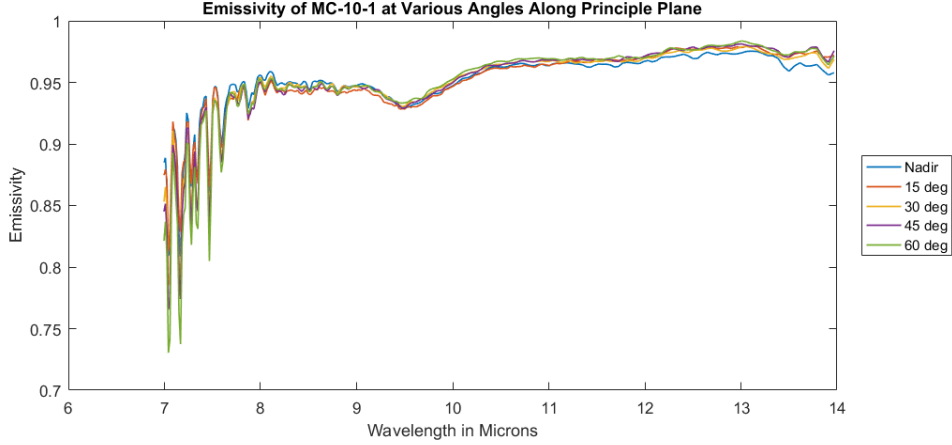


Figure 2.10: Little change in emissivity given angle occurs for another size that is not quartz. Measurements taken at the Nevada Automotive Testing Center in Nevada.

and back toward a sensor [23]. A solid piece of quartz will have tightly packed particles which will reduce volume scattering and increase surface scattering [21, 18]. When only fine particles are present, the contrast of the restrahlen bands decreases because fine particles are typically separated by a distance larger than the wavelength of light. This results in particles independently volume scattering [18]. Coarse particles typically only surface scatter, but may have clinging powder sized particles attached to them, increasing volume scattering by filling porous space between the coarse particles.

While Figure 2.11 shows two particle sizes, materials are usually made up of many grain sizes. Figure 2.12 explores the differences between eight groupings of particle sizes separated by sieves. Moersch and Christiansen corroborate the ideas explained by Salisbury and Wald in more detail [21, 24].

Particles of all sizes have been explored as natural contaminants on vehicle surfaces and even in the visible when examining planetary bodies [17, 15, 25]. Fines are materials having a particle size smaller than  $45\mu m$ . They are commonly referred to as powdered materials and in natural settings make up a small portion of a sample. In the example of the AHI sensor detecting land mines, detection is only capable because of our knowledge of the finest particle materials. The role of fines to a spectra has not been explored independent of a full material distribution. When a soil is disturbed, coarse underground particles brought to the surface are typically coated in electrostatically attached fine particles [2, 26]. Over time, these small particles detach from the coarse

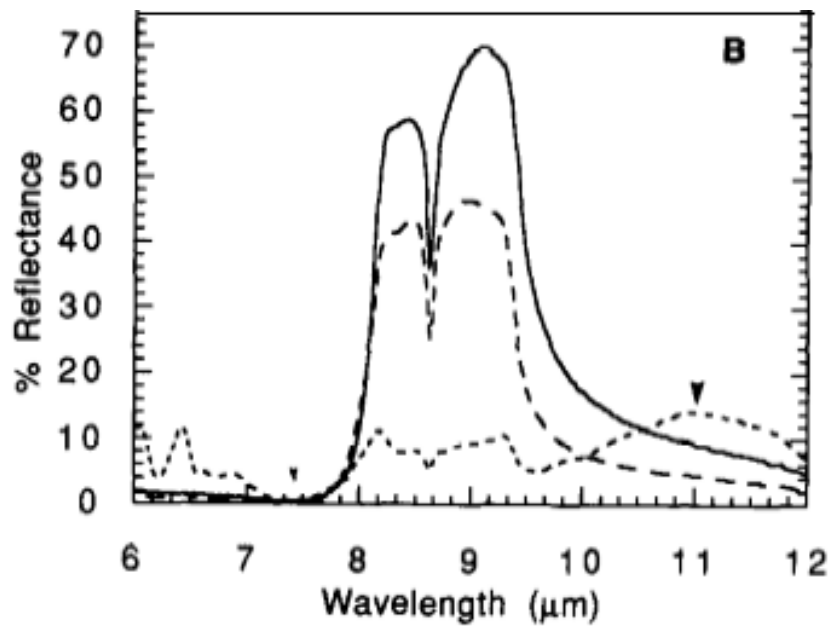


Figure 2.11: Reflectance change of quartz material between different particle sizes. The solid line represents a polished piece of quartz, the dashed line is the reflectance of large quartz particles ( $75\text{--}250\mu\text{m}$ ) and the small dashed line is the reflectance of fine particles ( $> 75\mu\text{m}$ ). Taken from Salisbury and Wald (1992), Figure 1B

particles from wind gusts, rain and other weathering effects, causing them to appear more like the surrounding undisturbed soils, thus reducing the spectral contrast of this feature. Immediately after a hole in the ground is created and filled in, the fines from the soil are present on the surface, changing the observed spectral characteristics. As time passes, these filled holes become more and more difficult to detect as the particle size used for identification is weathered from the soil.

## 2.9 Chemical Composition

Another important factor that affects the spectral characteristics of a material are its chemical composition and structure. Both of which are related in how they affect the final target spectrum. Chemical composition refers to the way that the target material is defined by its index of refraction information,  $n$  and  $k$ . When used in conjunction with other parameters of the material, the complex index of refraction ( $n + ik$ ) can be



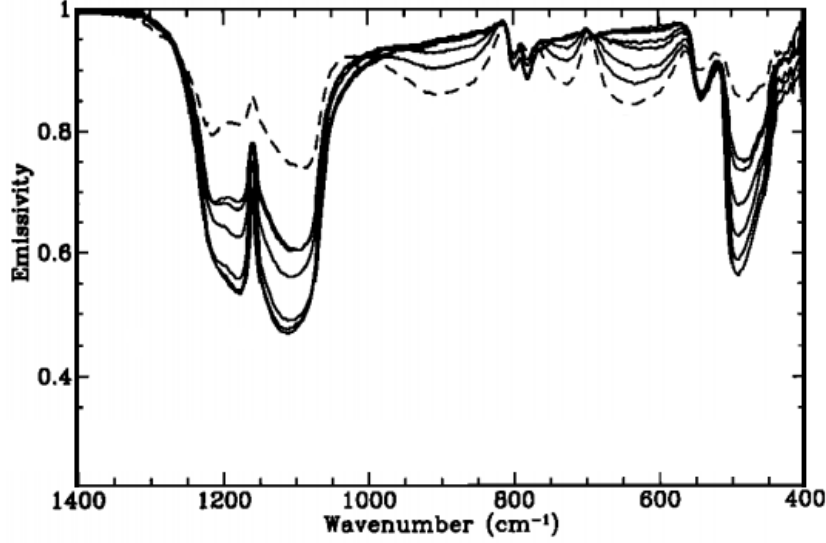


Figure 2.12: Emissivity of quartz particle sizes ranging from 15 to 277  $\mu m$  on a wavenumber( $cm^{-1}$ ) scale. Note that  $1000\text{ }cm^{-1}$  is approximately  $10\text{ }\mu m$ . Taken Figure 6a from Moersch and Christiansen (1995)

used in first principles modeling of materials [27]. These models have been employed at times to characterize chemical warfare objects and toxins for stand-off detection by the military for the unique spectral features of the agents in the infrared region [28]. Given the similarity to the military applications, industrial effluents could theoretically also be examined in this range.

It is a non-trivial problem to attempt to acquire the complex index of refraction of materials in the longwave infrared. There are however several different methods that could be used to extract usable spectra, each with unique challenges. The longer established method is called the single-angle reflectance method, which has been used in research for several decades. Experimentally, the reflectance of a material is measured in wavenumber space against that of a perfect reflector over a large spectral range [27]. In Blake (2017), materials were measured using a Bruker A510/Q-T reflectance accessory that had the capability to be outfitted with different optical components to obtain as large of a spectrum as possible ( $5000 - 50\text{ }cm^{-1}$ ).

The complex index of refraction information can then be derived from the Kramers-Kronig Transform (KKT) which uses the experimentally measured reflectance in wavenumber space. This relationship is described as

$$\phi(\nu_m) = \frac{2\nu_m}{\pi} \int_0^\infty \frac{\ln(\sqrt{R(\nu)})}{\nu^2 - \nu_m^2} d\nu \quad (2.20)$$

where equation 2.20 solves for the phase function  $\phi(\nu_m)$  with the measured reflectance. The best solution to the complex index of refraction will be evaluating the largest possible spectrum of wavenumbers in the integral (ideally infinite wavenumbers). Equation 2.20 can be manipulated to solve for both  $n$  in

$$n(\nu) = [1 - R(\nu)]/[1 + R(\nu) - 2R^{0.5}(\nu)\cos(\phi(\nu))] \quad (2.21)$$

and  $k$  in

$$k(\nu) = 2R^{0.5}(\nu)\sin(\phi(\nu))/[1 + R(\nu) - 2R^{0.5}(\nu)\cos(\phi(\nu))] \quad (2.22)$$

The largest issue with this method is that it requires a significant spectral range of measurements in order to properly work. In the example case described in Blake (2017), spectra were measured between 5000 and 50  $cm^{-1}$ . This corresponds to a wavelength range of 2.0 - 200  $\mu m$ .

Another method that can be employed is to compress materials into a disk and directly measure them using a IR-ellipsometer. Ellipsometry uses changes in the polarization state of light, specifically the amplitude ( $\tan[\psi]$ ) and phase difference ( $\Delta$ ) to calculate the index of refraction. Linearly polarized electric fields, both parallel and perpendicular to the incident plane, are used as illumination and amplitude and phases shifts are measured. These shifts in amplitude and phase difference are related to the parallel and perpendicular fields of light as seen in Fresnel equations by

$$\frac{r_p}{r_s} = (\tan(\psi)e^{i\Delta}) \quad (2.23)$$

where  $r_p$  represents the parallel field and  $r_s$  represents the perpendicular field. Measured data is input into a Levenberg-Marquardt algorithm to calculate the index of refraction at each wavelength [27]. The main issues with this method are that if materials are compressed into disks incorrectly or poorly placed in the ellipsometer, the measurements may cascade error and result in poor index of refraction derivations.

Material structure can be used to help identify previously derived index of refraction data by using x-ray diffraction. The crystalline structure of the material (monoclinic, tetragonal, cubic, hexagonal etc) will have unique intensity peaks at specific angles that

can be used to identify its structure. Each type of structure will have a distinctive index of refraction that could already have been measured and placed in a spectral library.

## 2.10 Solid Contamination Properties

The physical properties of solids are unique in comparison to gases and liquids. As stated in Section 2.7, solid materials act as unique particles with varying particle sizes which can have affects on optical properties. The location where the solid material is found must also be considered and can be separated in to many cases. The presence of solid contaminants is demonstrated as:

1. Natural contaminants on natural surfaces
2. Man-made contaminants on natural surfaces
3. Natural contaminants on man-made surfaces
4. Man-made contaminants on man-made surfaces

An example of man-made materials and surfaces are road asphalt covered in styro-foam peanuts. Man-made contaminant materials may also be considered a material that is not native to the area. Man-made surfaces such as concrete, asphalt and brick tend to lack distinct spectral characteristics in the LWIR. This research focuses on the effects of solid powder contaminants. Powders are considered to be particles that are less than  $45\text{ }\mu\text{m}$  in diameter. In many cases, powders are much smaller than that criteria, even on the order of the wavelength of light that interacts with them.

Several tests were completed to determine the validity of a solid material being a powder and understand its chemical composition and grain structure. An example material is silicon carbide obtained from Washington Mills seen in Figure 2.13. This material is listed as the dust collected fines from the mineral mine, which indicates that it passed through their smallest sieve and should follow the requirements of a powder. To confirm its material purity and geometric shape for modeling, a series of x-ray diffraction measurements of each material. The silicon carbide material results are shown in Figure 2.14 and demonstrate that when the it is composed of hexagonal structured silicon carbide grains based on intensity peak matches to that structure in a spectral library. Materials were also sent out to be measured using a Woollam IR-VASE

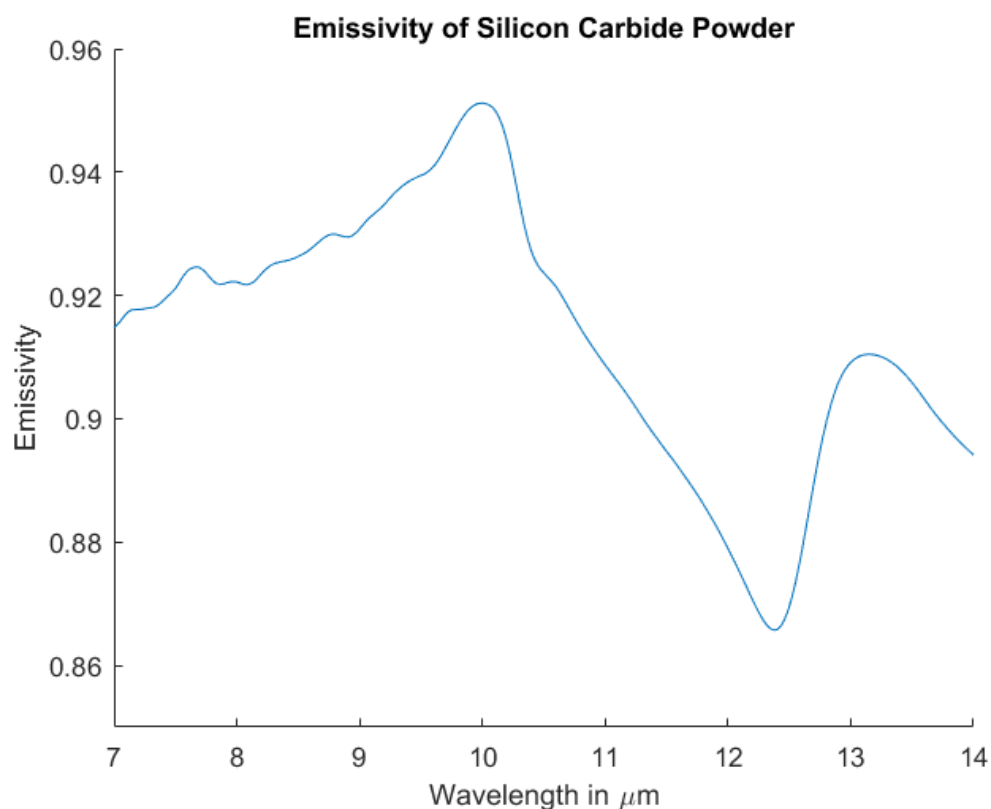


Figure 2.13: Pure silicon carbide powder emissivity.

Mark II ellipsometer at a lab in Lincoln, Nebraska. This was done to materials that had no discernible intensity peaks or contained multiple structures or materials.

Another test done is for the particle sizes of each particle and the effective particle size distribution. In large particles, size analysis can be completed by passing a large amount of material through a set of sieves in a sieve shaker. Because small particles tend to clump together, sieves are not as effective a method to do a particle size distribution. Instead particle size analysis is done by utilizing a scanning electron microscope (SEM).

The process for collection of SEM images starts by preparing the samples for the microscope. A small aluminum stub is covered in a carbon tab which acts as an adhesive to both the aluminum and the powder. Since the powdered materials are not naturally conductive, the materials must go through the process of sputter coating. A Gold Palladium material coats the powder coated carbon tab with a few nanometers of

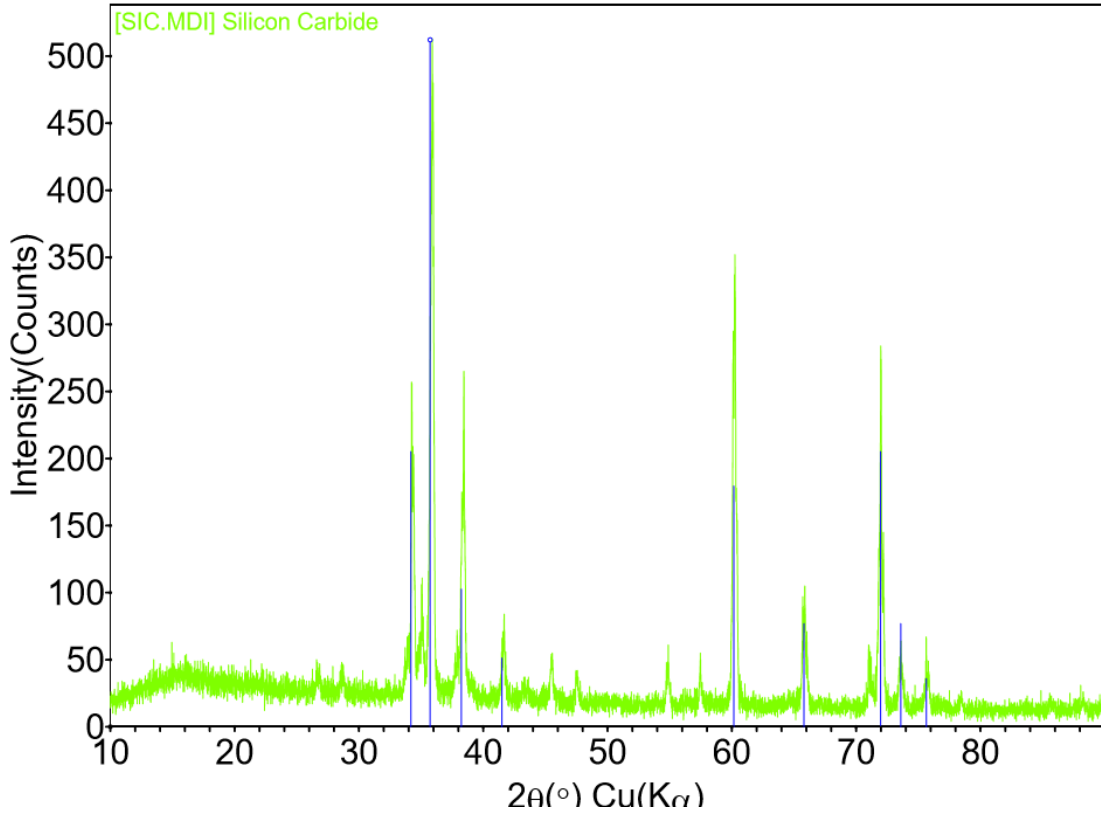
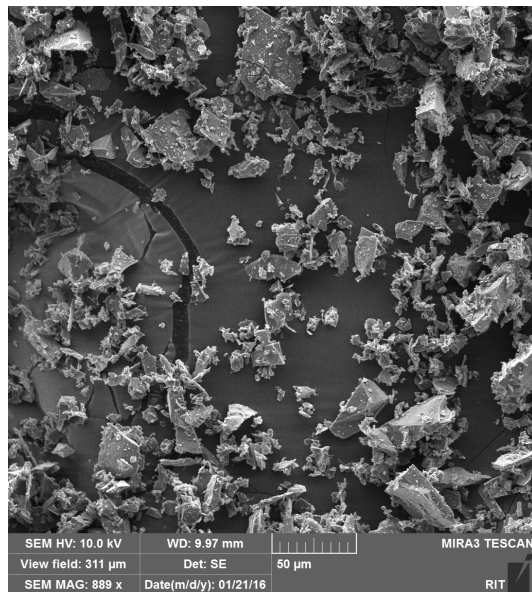


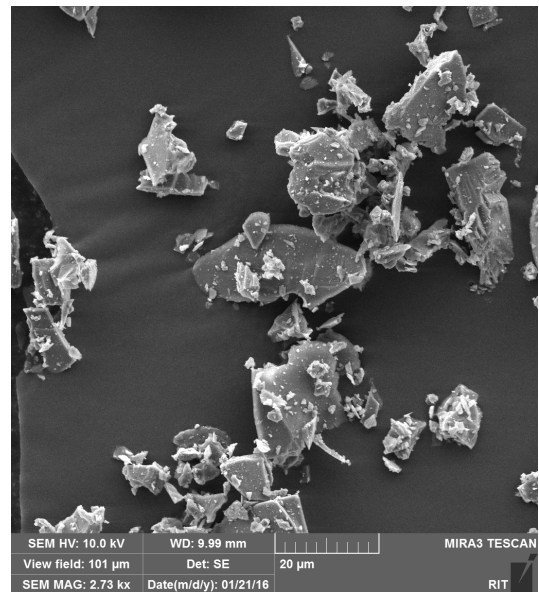
Figure 2.14: X-ray diffraction images of silicon carbide powder. Data was collected in the material science department at the Rochester Institute of Technology in August 2016.

material, making the surface conductive.

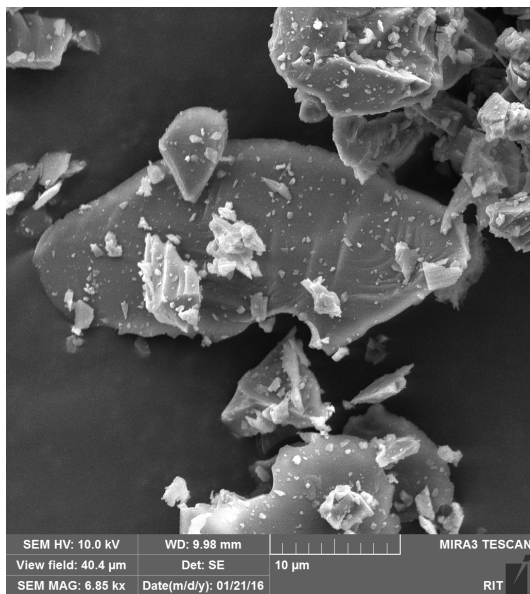
The material is now prepared to be imaged in the SEM. An electron gun within the instrument shoots electrons through several magnetic lenses towards the powdered tab. Electrons interact with the conductive surface and a signal is measured by the SEM of the surface one pixel at a time until an image is built up. Figure 2.13 shows the analysis of the silicon carbide at various zoom levels and projects a physical ruler next to each image. Each image demonstrates that the particles found in the Washington Mills sample are less than  $50\ \mu\text{m}$  in diameter. Particle size distribution on small sized materials can also be performed by examining the rate that an amount of material drops through a graduated cylinder of liquid over a long period of time.



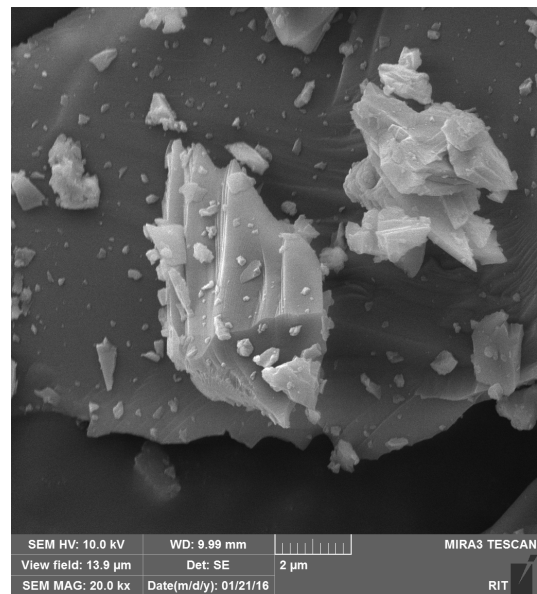
(a) SEM image of silicon carbide powder at 889x zoom



(b) SEM image of silicon carbide powder at 2730x zoom



(c) SEM image of silicon carbide powder at 6850x zoom



(d) SEM image of silicon carbide powder at 19970x zoom

Figure 2.15: Scanning Electron Microscope (SEM) images of silicon carbide powder at various zooming distances



## Chapter 3

# Theory

While non-linear material mixtures are commonplace in the real world, they are exceedingly difficult to recreate from a theoretical perspective. Currently, only a few models exist that can create an emissivity spectrum from knowledge of the two materials being intimately combined as well as a few parameters about each material. Of those, the Non-Conventional Exploitation Factor Data System contamination model is one of the strongest available commercially. It uses the NEF database of spectral reflectance data to create mixtures at any theoretical mixture level.

### 3.1 NEFDS Contamination Model

The Non-Conventional Exploitation Factors Data System (NEFDS) is a comprehensive spectral library of materials managed by Cortana Corporation that contains thousands of material reflectances on nearly every material on Earth[29]. The library is unique in that a material may have several unique spectral reflectances, each corresponding to various characteristics or conditions applied to that material. Such factors addressed include reflectance changes as a result of composition differences, moisture content, weathering and texture. The library itself contains over 25,000 individual reflectances with some materials having been measured several times over the course of years. Given the extensive nature of the library, many remote sensing applications utilize the database to help support new frontiers in research.

Cortana Corporation expanded upon its database to explore the functionality of interactive applications of their library that assist in research. One such application was a contamination model that could generate spectral reflectance information for non-



linear intimate mixtures between a substrate surface and a contaminant. Currently, RIT has access to version 15.0 of this model; later versions likely have significant changes to parameters. Version 15.0 of the model uses two reflectance measurements and a user defined mixture percentage to model the reflectance of the mixture. The contamination model evolved from their original linear mixture model

$$R(t) = R_s e^{\vartheta t} + R_\infty (1 - e^{-\vartheta t}). \quad (3.1)$$

The mixture reflectance  $R(t)$  was a combination of information from the reflectance of the substrate ( $R_s$ ) as well as the pure contaminant ( $R_\infty$ ). Each reflectance signature was modulated by the effective layer thickness  $t$  and a model fit parameter  $\vartheta$ . This parameter represents the contaminant scattering coefficient as a scalar value while also assuming that no multiple scattering effects occur either in the contaminant layer or between the contaminant and the sparsely covered substrate surface [29]. In actuality, wavelength dependencies exist for scattering in the examined spectral region. The linear mixing model is the only version of the contamination model that make the assumption that scattering can be generalized to a single value. The single scattering coefficient can be detailed further as

$$\vartheta \cong \frac{\rho_s}{\rho_q} \frac{3}{2D}, \quad (3.2)$$

which utilizes the relationship between the powder mass density ( $\rho_s$ ), a single particle mass density ( $\rho_q$ ), and the average diameter of a particle ( $D$ ). This statistical model indicates that particle size effects significantly change the linear model results as they approach the magnitude of the wavelength of light, suggesting that wavelength dependencies are a result of particle Mie scattering [29].

The largest challenge with Equation 3.1 lies in effectively incorporating contaminant layer thickness into the model. Consider a situation where so little contaminant exists on the surface that no consistent and measurable layer of contaminant is present. The model will fail as the parameter is not quantifiable. Removing contaminant layer thickness as a model parameter and replacing it with another parameter or set of parameters assists in accurately representing spectra of low contaminant mixtures. Another issue arises in the model when high amounts of contaminant are present. The shift in the thickness parameter's magnitude causes the model to become insensitive to thickness and produce diminishing returns to the parameter. Objectively, this makes the model's

thickness parameter unreliable and necessitates a parameter substitution for the term. The NEFDS linear mixing model was adjusted considerably to incorporate these changes as seen in

$$R_m(\lambda) = fR_s(\lambda) + (1 - f)R_c(\lambda), \quad (3.3)$$

which substitutes  $R_\infty$  with the contamination reflectance ( $R_c(\lambda)$ ). This adjustment also groups together the conglomerate of parameters and renames them as the area fraction of incident light through a contamination layer ( $f$ ). Essentially, the area fraction represents a non-linear electromagnetic radiation extinction method that mirrors the attenuation of light commonly seen in Beer's Law as transmission. Initially, the area fraction is written as

$$f = e^{-\alpha(\lambda)Nt}, \quad (3.4)$$

where  $\alpha(\lambda)$  describes the spectrally dependent extinction cross-section and  $N$  represents the particle number density. The extinction cross-section is also sometimes referred to as the extinction coefficient in Beer's Law when discussing measuring the radiance through a plume. It represents the product of the extinction coefficient ( $Q_E$ ) and the geometric cross-section of the contaminant particle ( $\sigma$ ). Utilizing a few principles of radiative transfer theory, additional equations will be substituted to eliminate thickness from the model. This increased the complexity of the radiation extinction term exponentially.

When the contaminating material coverage density is so large that the volume of particles begin to stack and become closely packed, the model becomes insensitive to number density. In order to address this insensitivity, the contamination model needs to create an effective number density as a replacement to number density [29]. The reason a standard number density representation fails in this model is that an incorrect assumption is made that the amount of light passing through a thin layer of particles is negligible compared to the open space found in between the particles [23]. This affects the area fraction of light and is only true for sparsely packed media, which is the majority of cases examined for this research. A substituted equation for the effective particle density ( $N_e$ ) is shown as

$$N_e = \frac{-N * \ln(1 - \phi)}{\phi}, \quad (3.5)$$

where  $\phi$  represents the fraction of the layer containing the contaminant or fill factor.

Essentially, Equation 3.5 is the product of the particle number density ( $N$ ) and a porosity coefficient [23]. Equation 3.5 can act as a substitute for  $N$  in Equation 3.4 and address issues surrounding thicker layers of contaminant.

Following the substitution, the thickness parameter still exists, therefore a relationship was developed to remove its dependencies from the model. This relationship was used to eliminate both the particle layer density and thickness in the exponential term. The relationship is given as

$$\frac{n}{A} = Nt, \quad (3.6)$$

where  $n$  represents the number of particles and  $A$  is the given area. The fraction is essentially representative of an area coverage density where its substituted components represent that same parameter, but use more realistic and measurable variables.

Now the area fraction contains no information regarding thickness or number density, but measurable quantities with the exception of the packing fraction ( $\phi$ ). In a situation where the coverage density was very small, a good assumption would be that the packing fraction will approach zero while for large coverage densities, the fraction would approach particle geometry. A phenomenological model for the packing fraction is used to eliminate the packing fraction seen as

$$\phi = \phi_0(1 - e^{-\beta \frac{n}{A}}), \quad (3.7)$$

where  $\phi_0 = .67$  and  $\beta$  is considered the rate at which the particulate layer approaches the asymptotic limit of packing for the packing fraction [29]. In the case of  $\phi_0$ , that value represents the density for spherical particles, which are common.

While the representation of  $\beta$  in the NEFDS contamination model is as a rate of change to the packing fraction, it is essentially a fitting parameter. There is no quantifiable way to know the rate of change in an instantaneous measurement of a material. The parameter also has no wavelength dependencies and unit analysis shows the units are in squared centimeters per gram. In the forward model, this parameter is considered a fit parameter.

Once applying all the model substitutions above, the resulting area fraction of light is significantly more complex than that found in the linear area mixing model. The

NEFDS Contamination Model Parameter Definitions	
Parameters	Parameter Definitions
$\alpha(\lambda)$	Spectral Extinction Cross Section of Contaminant
$n$	Number of particles
$A$	Area of interest ( $cm^2$ )
$\frac{n}{A}$	Contaminant coverage density. Equivalent units of $\frac{g}{cm^2}$
$\beta$	Rate of packing fraction change through contaminant layer
$\phi_0$	Volume of particle = $\frac{2}{3}$
$R_s$	Substrate Reflectance
$R_c$	Contaminant Reflectance

Table 3.1: NEFDS Contamination Model parameters and their respective definitions

non-linear area fraction of light is now

$$f = \exp\left[\frac{\alpha(\lambda)\frac{n}{A}\ln[1 - \phi_0(1 - e^{-\beta\frac{n}{A}})]}{\phi_0(1 - e^{-\beta\frac{n}{A}})}\right], \quad (3.8)$$

which when applied to the mixture equation is able to create non-linear mixtures between two materials.

The mixture reflectance is now represented by physical parameters that are practical, real, and stable. Each parameter in the area fraction now only represents a property of the contaminant alone.[29] In total, one spectrally dependent parameter and two scalar parameters are used in the model. A fourth parameter is naturally set to the assumed shape of a particle ( $\phi_0 = 0.667$ ). Once all substituted equations for the area fraction of light have been adjusted and input into the linear area mixing model, the final form of the NEFDS contamination model is created. The new non-linear model takes the form

$$R_m(\lambda) = R_c(\lambda)\left(1 - \exp\left[\frac{\alpha(\lambda)\frac{n}{A}\ln[1 - \phi_0(1 - e^{-\beta\frac{n}{A}})]}{\phi_0(1 - e^{-\beta\frac{n}{A}})}\right]\right) + R_s(\lambda)\exp\left[\frac{\alpha(\lambda)\frac{n}{A}\ln[1 - \phi_0(1 - e^{-\beta\frac{n}{A}})]}{\phi_0(1 - e^{-\beta\frac{n}{A}})}\right], \quad (3.9)$$

and uses reflectance data for contaminant and substrate materials from the NEFDS spectral library. Each term is defined in the table below.

### 3.1.1 NEFDS Contamination Model Parameters

While the model is now larger and more complex, it only carries four parameters beyond the reflectance information. There are two scalar parameter, one spectrally dependent parameter and one variable that remains constant regardless of situation. The spectrally dependent extinction cross section ( $\alpha(\lambda)$ ) references the total loss of energy due to absorption and scattering in a medium of the contaminating material alone. Since it is only dependent on the contaminant, there should not be any change to the parameter based on the level of contaminant present. Unlike its counterpart in the linear area mixing model, the extinction cross section contains the effects of multiple scattering and is wavelength dependent.

One of the scalar parameters  $\frac{n}{A}$ , represents the area coverage density of the contaminant on a surface. This could also be referred to as the physical amount of material over a given area [29]. The parameter has two components: the number of particles ( $n$ ) and the area of coverage ( $A$ ). While it is possible to measure the number of particles, it lacks practicality in a real experimental situation, especially when considering materials with particles on the order on hundreds of nanometers in diameter. A reasonable alternative to an exact particle count is to use a measured contaminant mass within that area. Unit analysis dictates that either number of particles or grams are acceptable in the finalized equation. For imaging systems, this assumes a consistent coverage density across each pixel.

The second scalar parameter  $\beta$  is defined by the NEFDS contamination model documentation as the rate of change in the effective packing fraction of the contaminant [29]. This definition is neither intuitive or physically descriptive enough to understand. When analyzing the units for each parameter of the forward model, the  $\beta$  parameter ends up having inverse coverage density units  $\frac{cm^2}{g}$ , which are easier to explain from a physical standpoint. A low value for  $\beta$  indicates that the contaminating material particles are likely to be stacked and concentrated in a smaller area. Higher values for  $\beta$  suggests that particles are spread across a large area and unlikely to be stacked. In contamination model version 15.0, this parameter was created through a first principles derivation and remains independent of wavelength.

Technically speaking,  $\phi_0$  could be considered a third scalar parameter that represents the fill factor of a single particle. In the forward model, the model assumes that most particles are spherical with a estimated fill factor of two-thirds. For the purposes of this research, the spherical particle assumption is maintained. Even if variation occurs

between particles the average shape from the distribution will represent the spherical approximation

Despite the uniqueness of the NEFDS contamination model to create non-linear emissivity mixtures, its current extent within the NEF database is limited to use of just over a dozen materials. These limitations make the model irrelevant to current hyperspectral applications.

### 3.2 Extinction Cross Section

In attempts to directly measure the extinction cross section parameter found in the NEFDS contamination model, a mathematical solution was created that in theory would find a novel solution for the cross section of particles compressed into a disk. Mathematically, the extinction cross section could be calculated using Beer's Law because the parameter is contained within the transmission term. A standard Beer's Law equation appears as

$$I(\lambda) = I_0(\lambda) * e^{-N\alpha(\lambda)Z}, \quad (3.10)$$

where  $I(\lambda)$  is the measured radiance of a contaminated surface,  $I_0(\lambda)$  represents the radiance of a pristine surface,  $N$  represents the volume density of the contaminant,  $Z$  represents the optical path length through a layer and  $\alpha(\lambda)$  is the cross section. This form of Beer's law is sometimes used in cases of sensors staring through a gaseous plume or layer of atmosphere where path length and volume density will have an impact on the resulting radiance. Since this experiment involves a solid powder layer, the path length term is not necessary. Volume density must also be replaced with number density to keep unit analysis consistent. This can be accomplished by dividing out the depth of the material disk from the volume density as the disks represent a well characterized volume density. This reconfigured Beer's law equation for powdered materials now appears as

$$I(\lambda) = I_0(\lambda) * e^{-n\alpha(\lambda)}, \quad (3.11)$$

with number density having units of  $\frac{g}{cm^2}$  and path length now removed by the only considering the extent of the disk. Rearranging this equation to solve for the extinction cross section results in

$$\alpha(\lambda) = -\left(\frac{1}{n}\right) \ln \left[ \frac{I(\lambda)}{I_0(\lambda)} \right]. \quad (3.12)$$

In a singular sense, with knowledge of one disk's number density, equation 3.12 can be applied to solve for the cross section. Disks of increased number density will likely have large differences in the amount of electromagnetic energy that can pass through them. Therefore a robust solution that incorporates several disks can be created by again rearranging equation 3.12 to appear as

$$\ln \left[ \frac{I(\lambda)}{I_0(\lambda)} \right] = -n\alpha(\lambda) \quad (3.13)$$

which takes the format of the standard linear equation  $y = mx + b$ . Using measurements of several number densities, a semilogarithmic plot can be created using equation 3.13 that defines a linear plot of the log-ratio to number density at each wavelength. The slope of this line will represent the extinction cross section while the intercept in theory should be zero or nearly zero. If an intercept of any significance does exist, backing it out would place it in the transmission portion of Beer's law as

$$I(\lambda) = I_0(\lambda) * e^{-n\alpha(\lambda) + \gamma(\lambda)} \quad (3.14)$$

where  $\gamma$  represents the wavelength dependent y-intercept in the previously mentioned calculations. There is no concrete definition as to what this error term represents physically, but the error is spectrally dependent.

### 3.3 Signature Injection

Target signatures can be injected into an airborne hyperspectral image as synthetic target data using several methods. Aerial emissivity imagery came from a 2015 collection of data from the Blue Heron LWIR sensor which performed a radiance collection over an asphalt parking lot in the Gate, New York region. The radiance image was converted into emissivity space for target injection. Synthetic target signatures were created using estimated parameters from the parameter inversion model discussed in Chapter 4 as inputs to the forward contamination model seen in equation 3.9. The pure contaminant reflectance signature comes from the empirically measured dataset ( $R_c$ ), while the substrate signature ( $R_s$ ) was created from the selected background pixel corresponding to the location where the synthetic target was placed.

The purpose of placing synthetic targets in a scene using the parameter estimates from the parameter inversion model was to assess the performance of detection algorithms using target pixels with a wide variety of properties without varying the target signature used in the algorithm. Targets varied based on the coverage density from the estimated parameter set, but were also given varying sub-pixel fractions ( $\delta$ ) for total pixel coverage. As an example, a sub-pixel fraction of  $\delta = 0.8$  indicates that 80% of the pixel has an intimate mixture while the remaining portion contains just the pure background substrate. A visual table of targets within the image containing different combinations of these two properties was created.

Target detection is an application of remote sensing where a user attempts to find any occurrences of a similar matching pixel in a hyperspectral scene to a spectral signature provided as reference. Image pixels are tested against this reference spectrum and assigned a detection score which can be compared to a user defined threshold. Image pixels whose detection statistic is above (depending on detection algorithm) the threshold are assigned as targets while those below the threshold are not given any distinction. If a pixel that does not incorporate any of the material of interest, but has a score above the defined threshold it is considered a false alarm. Missed detections and false alarms are common given the nature of the problem. Detection difficulties increase when considering the desired material may only exist in a few number of pixels in the scene and may not fully encapsulate an entire pixel area (sub-pixel).

Statistical methods of detection such as the adaptive cosine/coherence method (ACE) attempt to solve the detection problem by using prior knowledge of the spectral signature and testing every pixel in the scene against it. The equation for the ACE detector is

$$D_{ACE1} = \frac{((t - m)' \Sigma^{-1} (t - m))^2}{\sqrt{(t - m)' \Sigma^{-1} (t - m)} \sqrt{(x - m)' \Sigma^{-1} (x - m)}} \quad (3.15)$$

where  $t$  represents the target spectrum,  $m$  represents the background mean,  $x$  represents the test pixel from the scene and  $\Sigma$  defines the background covariance of the image. While ACE is considered as one of the best detection algorithms, detection performance is susceptible to a number of problems related to signature mismatch. Manolakis (2010) cited problems including atmospheric propagation, sensor noise, and intrinsic spectral variability that can contribute to mismatch of the test pixel to the target spectrum. Statistical algorithms in general are more likely to have mismatch due to these factors as they all require the background covariance matrix for determination. While all



important, little discussion was placed on the value of using variant target signatures based on properties of test pixels. Given that the properties of target pixels could be significantly different while simultaneously only accounting for a handful of pixels in the scene, using an unrepresentative target spectrum for detection could cause target pixels to go undetected despite both signatures being the same material. This mismatch is especially prominent in some cases where in-scene targets are of low density coverage or are sub-pixel in nature as spectral signatures deviate from the pure material signature in these situations. An analysis of how target detection with an specific type of target spectrum changes the ability of a test pixel to be detected will help define situations to use more representative target spectra than just a pure material signature.

### 3.4 Simulated Contaminant Scenes

While empirical measurements assist in the confirmation of the accuracy of the parameter inversion algorithm, they are not perfect. Measurement errors occur that can cascade through a series of calculations, leading to a misrepresentation of the derived physical parameters in the inversion algorithm. By design, simulated data cannot have measurement errors because the scenes are created for ideal conditions and model parameters are set by the user. One potential method for simulating data is  $\mu$ DIRSIG, which uses scenes that can be created in Blender or in a text file. Like the NEFDS contamination model,  $\mu$ DIRSIG can create intimate mixtures between a surface and a sparse layer of contaminating material, however it uses the index of refraction information and absorption coefficient to perform its calculations. Conditions of a scene including the number of particles, size of particles and density of coverage can easily be controlled by the user.

As a simulation tool,  $\mu$ DIRSIG relies upon a first principles, physics based ray tracing model to evaluate the BRDF of a surface and its polarization components at a sub-pixel level [30]. This model considers surfaces as having several facets within a single pixel which captures influences of particles that are not locally flat. Objects are created using a program like Blender and assigned optical properties ( $n$ , *absorptioncoefficient*) based on which materials are needed. The absorption coefficient is easily found using the imaginary component of the index of refraction at each wavelength  $k$ . Ray-tracing solvers in  $\mu$ DIRSIG and DIRSIG trace rays from the surface back through until reaching a illuminating source such as the sky or sun. In  $\mu$ DIRSIG however, the entire hemisphere is treated as a series of detectors that collect rays to capture an entire BRDF scan [30]. Output results come in a variety of forms, including as a bi-directional reflectance

distribution function (BRDF) or as individual Stokes vectors. The first Stokes vector will provide the information needed to create a single emissivity spectrum that will be used in the parameter inversion algorithm.



## Chapter 4

# Methods

The accurate estimation of a contaminant mass from empirical remote sensing data is a complex task. The motivation for finding this information is to be able to quantify the smallest amount of a material that can be detected under specific conditions. This information could also pose useful in an environmental application such as pollution monitoring, or in risk assessment for hazardous effluent materials. A technique to estimate the amount of contaminant and other parameters takes advantage of both empirically derived and simulated results. The process is detailed from initial ground based physical measurements to deriving physical properties from signatures injected into remotely sensed hyperspectral data. An overview of the entire process can be seen in Figure 4.1 below.

Experimentally measured LWIR mixture emissivity spectra were input into a parameter inversion algorithm that calculates the physical parameters of the NEFDS contamination model using intimate mixture spectra. Once estimated, improvements to the inversion model were attempted, including the direct measurement of individual parameters. The parameter inversion model results were then used to create synthetic target signatures within real airborne LWIR hyperspectral images. Targets were made original by varying the properties of density and sub-pixel fraction into specific combinations. By making each target block a unique combination of the two parameters, a determination of the ideal spectral signature to use in target detection for each combination can be made. This helps inform ways to better employ target detection methods in hyperspectral scenes. Target detection was performed on the images with the ACE algorithm and several varied target spectra. Target detection scores for every pixel were calculated and the best input spectra was determined. From this, a map of the ideal

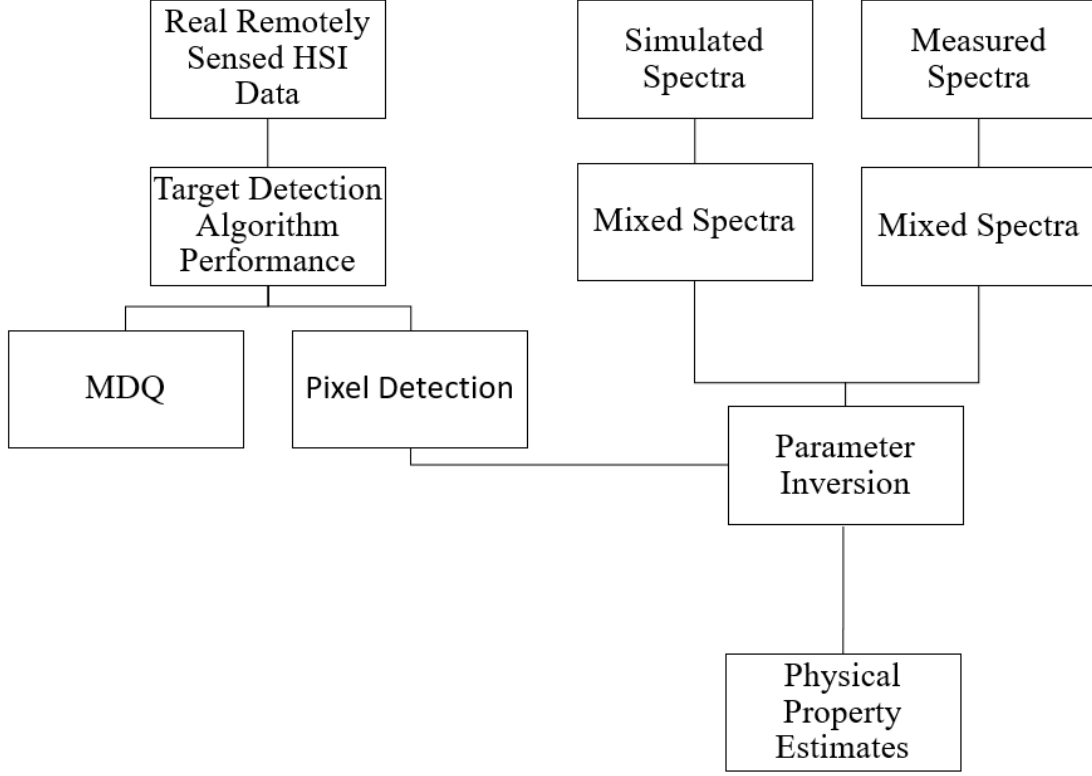


Figure 4.1: A flow chart depicting an overview of the project.

target spectra for each combination of pixel coverage and density was made.

Attempts at first principles simulations of intimate mixtures using  $\mu$ DIRSIG were also made to try and create an LWIR spectrum similar to those experimentally measured. The goal was to make intimate mixture spectra with known parameters that could help confirm the fidelity of the parameter inversion model.

## 4.1 Measurements

In order to reduce the impact of environmental biases on contaminated surface measurements, both laboratory and field equipment were utilized in the experimental process. Laboratory data provided more realistic signatures not found in outdoor hyperspectral scene collections. Temperature is one of several factors that influence a LWIR spectral signature outdoors [10]. If wind, rain or clouds are present, then the temperature of

the measured surface and atmosphere will have temporal inconsistencies throughout the collection period. Indoor laboratory measurements have no environmental biases, but are not as comparable to real remote sensed data. Therefore, it is important to examine both types of collected data as a cross check.



Figure 4.2: One inch thick aluminum plate painted with Krylon 1602 Ultra Flat Black spray paint.

Most field measurements were made on the roof of the Chester F. Carlson Center for Imaging Science on the Rochester Institute of Technology campus on various days throughout the summers of 2015, 2016 and 2017. The roof was ideal for measurements because of its height above surface obstacles. At that height, no major trees or buildings can occlude portions of the sky hemisphere. The rooftop surface is covered with a thick rubberized tar which heated quickly in the morning and maintained surface temperature continuity, resulting in a large difference between the sky and surface. Atmospheric effects such as wind and clouds were greatly diminished by examining weather forecasts and selecting days with clear skies and little to no wind or humidity.

Measurements also occurred in Silver Springs, Nevada at the Nevada Automotive Test Center approximately one hour east of Carson City. Nevada provided an ideal situation to record a large amount of data in optimal environmental conditions. From an

environmental standpoint, Nevada has very warm air temperatures and near zero humidity during summer months. Clouds typically only appear during afternoon hours when the FTIR instrument is less useful due to self shadowing at nadir. Central Nevada has the benefit of being very sparsely populated and does not have many trees or buildings, making the sky hemispherical occlusion a non-factor.

### 4.1.1 Substrate and Contaminant Selection

#### Substrates

Multiple types of substrates and contaminants were selected for this project, ensuring that a diverse collection of material combinations could be constructed for measurements. A strict set of criteria was implemented for selecting both contaminant and substrate materials for consistency. In the case of substrates, the requirements were that

1. Substrate surfaces must hold a consistent temperature over a long period of time
2. Substrate surfaces must be relatively flat, smooth and not physically mix with contaminants
3. Surfaces be well characterized in the longwave infrared spectral range
4. Substrates must be available and easily transported

As discussed in Chapter 2, having a consistent temperature throughout the measurement set significantly increases the accuracy of measurements so that there is improved performance in the temperature emissivity separation for each spectrum. Controlling the smoothness of the substrate simply mitigates another factor that can affect the measurements. Substrates with spectrally flat signatures are preferred initially in order to identify contaminant features easier. As characterization was achieved, some additional complex substrates were considered including a hardened soil surface which had its own strong spectral features.

For initial experiments, a one inch thick aluminum sheet was used and painted with Krylon Ultra Flat Black 1602 spray paint as seen in Figure 4.2. This spray paint has a well known flat signature in the longwave infrared region. The aluminum sheet has a smooth surface without texture to reduce effects of surface roughness. Since metals in general tend to have a low thermal conductivity, they can retain heat for longer

longer periods of time. Aluminum is not as thermally conductive, however a flat black painted piece of steel the same size as the aluminum was also used. These should appear spectrally the same as the surface is coated with the same material, however the steel retains heat much better than the aluminum.

Two other simple surfaces used in experiments were an asphalt slab and a concrete slab. Like the black painted aluminum and steel, asphalt and concrete also have flat spectral signatures in the longwave infrared and hold temperature well. The major difference between the two is that asphalt has much more pronounced surface texture with cracks being present throughout the layer. Both materials have spectrally flat LWIR signatures. The one soil substrate examined was of a soil surface from the Nevada desert that was flat and hardened from the sun. While it did have spectral features, the soil had physical properties more in line with asphalt as cracks were present from being dried out.

### **Contaminants**

The requirements that needed to be met for powdered contaminants were less strict than the substrates. Each contaminant simply needed to be made of solid material and consist solely of powder sized particles. Powder materials are considered solids that have particle sizes less than  $45\text{ }\mu\text{m}$  in diameter. Acquiring spectrally interesting materials of this size proved challenging, but several materials were found, four of which are discussed in detail. Several manufactured powder materials (silicon carbide, fused silica, white and brown aluminum oxides) came from Washington Mills. The remaining two were a red chalk powder from Irwin Construction and a Quartz calibration sand. The red chalk powder is a composite of relatively larger calcium carbonate particles coated with smaller red iron oxide dust. The quartz has some larger particle sizes while the rest fit the exact definition of a solid powder material. Spectral emissivity measurements were made for each material both as pure material and as progressively more contaminant was added to a substrate surface.

#### **4.1.2 Powder Deposition Technique**

The most challenging and quantifiable aspect of experimentally applying powdered contamination to surfaces was doing so in a repeatable fashion. The first attempted deposition technique involved the deposition of materials via a kitchen flour/sugar duster acquired from a kitchen supply store that would normally be used in baking applica-



tions. While the duster had a convenient application squeeze handle, the design was clearly not ideal for this specific application. The mesh grading was too wide to hold reasonably large amounts of material and squeezing the handle failed to consistently drop equal amounts of material each time.

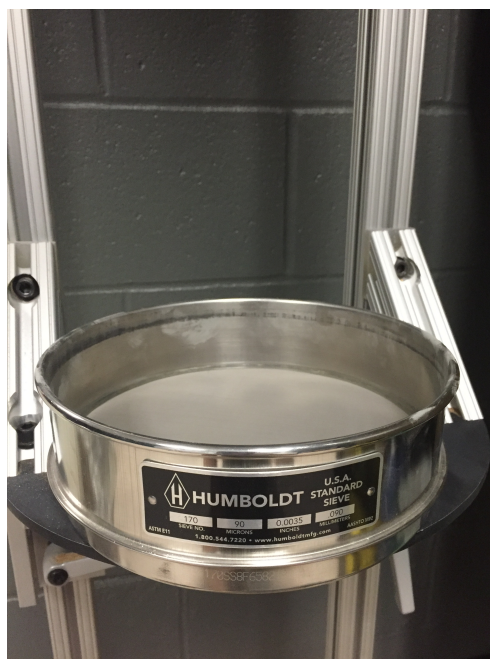


Figure 4.3: Humboldt sieve used to apply contaminants to the substrate surfaces.

Improvements to the deposition technique were made over time that applied powder materials through actual mesh sieves seen in Figure 4.3 that have significantly improved deposition consistency. Sieves chosen were two to three times the size of the largest particles present so that material can effectively pass through without excessive force. Material was released from a consistent height of just above the desired surface in order to prevent material from being carried off by light surface winds. Once a force was applied to the side of the sieve, a small amount of the powder leaves the sieve and falls onto the surface. Mass measurements were made of the sieve before and after each application was completed with the difference being the amount applied to the surface. This technique currently provides consistent deposition of materials considering all sources of error. After each deposition occurs and after a short period to allow the substrate and contaminant to reach thermal equilibrium, a spectral emissivity measurement was

taken. One unfortunate aspect to this technique is that the sieve area is several inches in diameter larger than the instrument IFOV. Because of this, the derivation of total contaminant mass is made using a subset of the area under which the contaminant is deposited.

#### 4.1.3 LWIR Instrumentation

##### **Spectral Emissivity Measurement: FTIR**

The main instrument used to measure the emissivity of objects in a field setting is the portable Designs and Prototypes Fourier Transform Infrared Spectrometer Model 102F. Light enters the  $4.8^\circ$  foreoptic and is detected on a Mercury Cadmium Telluride (HgCdTe) liquid nitrogen cooled detector with a spectral sensitivity ranging from 2-16  $\mu\text{m}$  [31]. Realistically, the strongest portion of the LWIR, ranging from 7.0 to 14  $\mu\text{m}$  provides ample electromagnetic energy for the sensor to detect accurately. The midwave range is highly inaccurate during daylight hours as solar radiation is equally dominant as thermally emitted radiation in this region, but could conceivably be used during night hours. The current sensor also does a poor job detecting photons in the shortwave spectral range. In the LWIR, more than 218 individual measurements spaced in bands approximately 30 nanometers wide are possible with this sensor. [31, 32, 33].

The instrument itself attaches to a standard camera tripod and sits one meter off the surface as seen in Figure 4.4. The foreoptic has an IFOV of  $4.8^\circ$  which projects a three inch circular spot size from a meter tall tripod. A digital inclinometer can help adjust the foreoptic view angle so that a nadir viewing angle can be achieved. Off-nadir measurements can be made up to  $60^\circ$ , but as the angle changes, the spot size transforms into an ellipse and the spot area increases. As seen in Table 4.1, the area difference between a nadir measurement and  $60^\circ$  off axis on the instrument stand is quite large ( $34\text{in}^2$ ). Angular measurements were not considered for this research as it is difficult to estimate masses with inconsistent spot sizes.

A single measurement of surface emissivity requires four individual measurements of different properties to eliminate specific terms in radiance space. Two blackbody measurements are made with one cooler than the estimated surface temperature and one warmer than the estimated surface temperature. The blackbody used was a temperature controlled instrument attachment that quickly modifies itself to the desired user input temperature. Both the cold and warm blackbody measurements bookend the sample and downwelling correction radiance measurement. The latter removes atmospheric



Figure 4.4: Designs and Prototypes FTIR 102 instrument set up.

downwelling effects from the scene by collecting only electromagnetic energy that reflects off a highly reflective Infragold plate. Atmospheric path radiance is negligible from one meter above the surface as not enough atmosphere is between the surface and instrument to have an effect. Temperature emissivity separation (described in Section 2.5) was performed on data when a ground temperature was not available and from this an output emissivity spectrum was computed. Field measurements more closely resemble airborne collected data, but are more error prone because they contain environmental influences from the surroundings. Laboratory measurements are not realistic to airborne collected data, but can help inform an accurate measurement of a material in a controlled setting.

### **Spectral Emissivity Measurement: Reflectometer**

Once field measurements are complete, laboratory comparisons can be made using the Surface Optics Corporation 400-T directional reflectometer. Since no method exists to completely remove atmospheric and environmental effects from a thermal field measurement, laboratory measurements can act as a pseudo ground truth to those in the field.

D&P Spot Size Differences by Angle				
View Angle	Distance to Aperture (in)	Spot Size Major Axis Diameter (in)	Spot Size Minor Axis Diameter (in)	Spot Area ( $in^2$ )
Nadir	30.5	2.557	2.557	5.134
15°	31.5	2.710	2.647	5.633
30°	35	3.328	2.952	7.717
45°	44	4.908	3.616	13.936
60°	60.75	9.535	5.113	38.290

Table 4.1: Design and Prototypes Model 102F spot size differences by angle.

Upwelling and downwelling are not present in reflectometer measurements because the instrument is in contact with the surface of interest throughout the measurement process [34, 35].

A typical spectrum collection by this instrument ranges from 2-25  $\mu m$  with an adjustable spectral resolution that is normally set to  $4cm^{-1}$  and a triangle apodization method [35]. A benefit to requiring the instrument to be in contact with the desired surface is that the instrument aperture does not need to be large to make measurements. In this case, it is a circular opening only half an inch in diameter.

Rather than measure the emissivity of an object, which requires a thermally cooled sensor, the Surface Optics Corporation 400-T measures the reflectance of a surface. This can be done despite surfaces at room temperature having a peak wavelength exitance of around  $10\mu m$  by using a high temperature internal heating source. This internal source is a silicon carbide globar which heats to a temperature of 1650 K and exits as a collimated infrared radiation beam [34]. A parabolic mirror focuses the beam to a reflecting mirror that passes the energy onto the surface of interest. Reflectance is used in the parameter inversion algorithm and the emissivity is calculated by using the known relationship between emissivity and reflectance, described by Kirchhoff's law. Since the instrument needs to be in contact with the surface, there is no true collection geometry.

A Michelson interferometer modulates the collimated beam to create interference patterns detected by two infrared detectors. The combination of the multiple interference patterns create a Fourier domain representation of the sample directional reflectance spectrum. Between each sample measurement, the instrument switches a chopper (seen in Figure 4.5) from open to closed and measures the internal source off a gold mirror as a reference [34]. The sample measurement is divided by the reference value and mul-



Figure 4.5: Surface Optics Corporation 400-T Reflectometer. The aperture (seen in gold at the top of the instrument) is roughly half an inch in diameter.

tiplied by a calibration value to get the final sample reflectance. Proprietary software can perform measurement correction by spectrally smoothing the measured directional reflectance based on user input criteria.

## 4.2 Estimation of Physical Parameters

Parameters used in the calculation of a reflectance mixture in the NEFDS Contamination model (see Chapter 3) were found to be informative to the physical characteristics of materials. Since the model only functioned in the forward state, there was no way to use already measured mixture spectra to find out physical properties of the mixing materials. The method proposed looks to invert this forward model in order to estimate these parameters for intimate mixture spectra.

Inverting the contamination model to estimate physical parameters is a complex process. A single step optimizing algorithm cannot mathematically determine scalar and wavelength dependent parameters simultaneously. Instead a complex three-step inversion model encompassing multiple separate optimization processes (seen in Figure

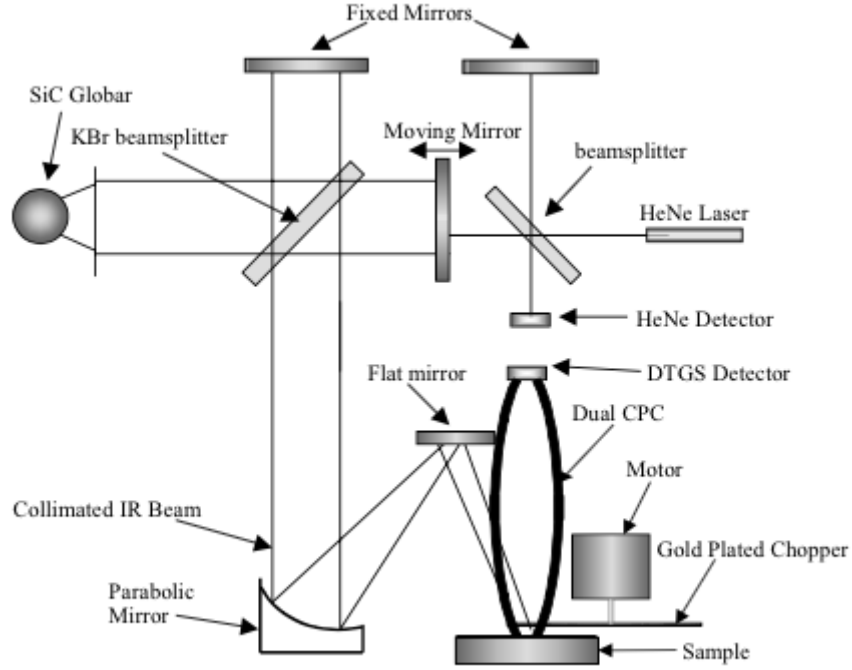


Figure 4.6: Diagram of inner workings of SOC-400T reflectometer. Taken from SOC-400 manual.

4.7) estimated the unknown parameters iteratively. The forward version of the NEFDS contamination model takes substrate and contaminant spectra along with a user defined coverage percentage to derive a mixture reflectance signature. The parameter inversion model requires three spectral signatures; the bare substrate, pure contaminant and mixture spectra. The output result from the parameter inversion model are estimates of the three unknown parameters  $(\alpha(\lambda), \beta, \frac{n}{A})$ . The first step in this process estimates all three parameters as if they were scalars. A general minimization will appear in:

$$\min_x \|f(x)\|_2^2 = \min_x (f_1(x)^2 + f_2(x)^2 + \dots f_n(x)^2), \quad (4.1)$$

where each  $f_n(x)^2$  represents a parameter in the model. Specifically, the technique used in the first step is called a trust-region reflective optimization. A trust region is a subset of an objective function that is estimated with a given model. Good agreement between the expected improvement and actual improvement expands the trust region over a

larger range and poor agreement contracts it. This process continues until reaching a solution or hitting a boundary condition.

Mathematically, the objective function is  $f$  while a function  $q$  is applied across a small neighborhood  $N$  around a specified point  $x$ . The neighborhood represents the trust region where minimization occurs and is represented as

$$\min_s \{q(s), s \in N, \}. \quad (4.2)$$

Once agreement is found (typically a threshold marker is set) where  $f(x + s) < f(x)$ , the neighborhood expands by  $s$  and finds a new minimization. The process continues until reaching a defined convergence threshold or until the number of iterations reaches its maximum. In order to prevent the optimization from hitting a boundary condition, 100,000 iterations were completed with each computation.

Results from the first optimization routine provide initial scalar estimates for each parameter. Unlike  $\beta$  and  $\frac{n}{A}$  which are both scalar parameters,  $\alpha(\lambda)$  is wavelength dependent and requires a vectorized solution. The second optimization step creates a solution for  $\alpha(\lambda)$  by rearranging equation 3.9 into the form of

$$\alpha(\lambda) = \ln \left[ \frac{R_m(\lambda) - R_c(\lambda)}{R_s(\lambda) - R_c(\lambda)} \right] * \frac{\phi_0(1 - e^{-\beta \frac{n}{A}})}{\frac{n}{A}(\ln(1 - \phi_0(1 - e^{-\beta \frac{n}{A}})))}. \quad (4.3)$$

Along with the mixture, substrate and contaminant spectra, the initial parameter estimates for  $\beta$  and  $\frac{n}{A}$  are also input into 4.3, allowing for the direct calculation of  $\alpha(\lambda)$ .

Despite its simple appearance, finding the correct  $\alpha(\lambda)$  presents the largest hurdle to calculating a complete solution due to the presence of the logarithmic fraction. There are four possible results of the argument of the logarithm that have large consequences to finding a real result. This interior fraction of the logarithm contains differences between the substrate and pure contaminant and the differences between the mixture and pure contaminant. For further cases, this operation represents the contrast ratio of the materials. When the mixture spectrum is enveloped by the substrate and contaminant spectra, the contrast ratio will be positive and the resulting logarithm produces a real result. When the mixture spectra does not lie between the two pure material reflectance signatures, the logarithm produces an imaginary component. If any of the mixture spectra within a data set contain spectral locations that create an imaginary component, the data was assumed to be poor and those specific wavelengths were eliminated from the spectra and calculations continue as if those points were not collected. When this

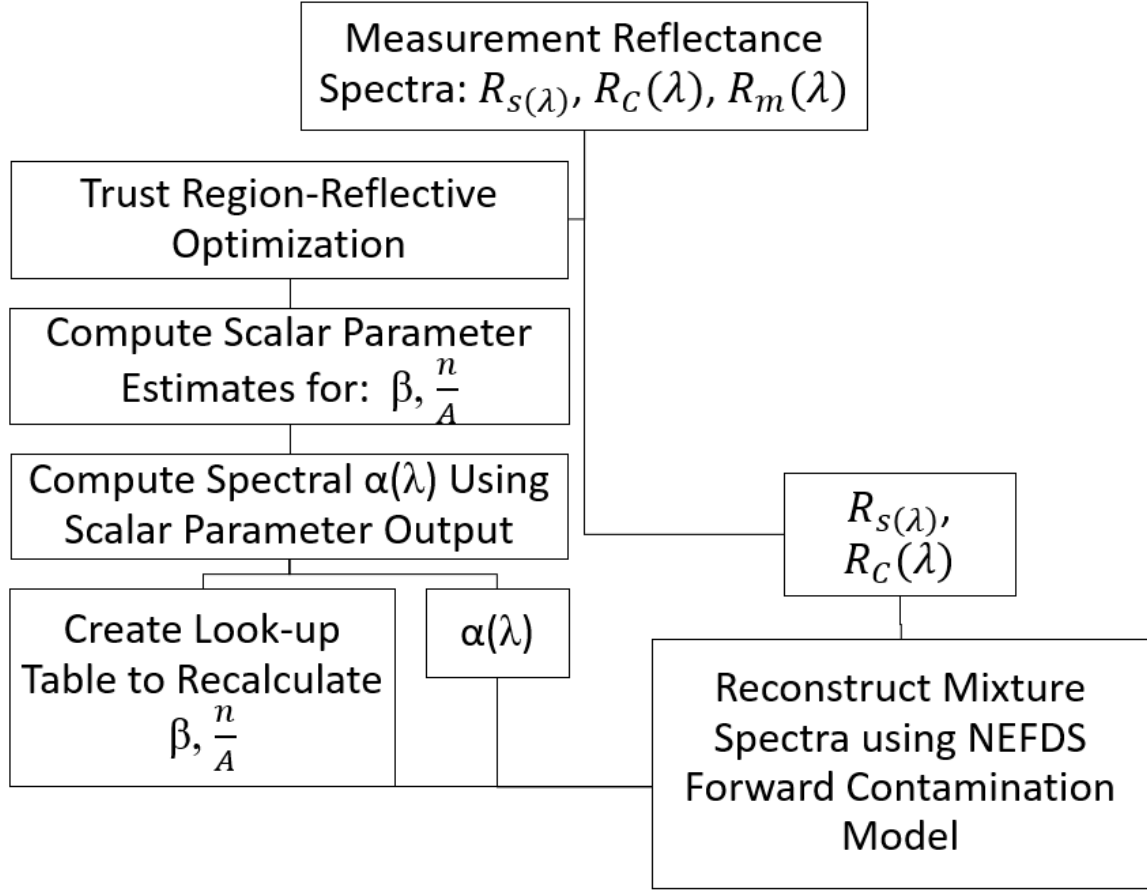


Figure 4.7: Flow Chart of model parameter inversion process.

occurs at a point for one mixture spectra, that point is eliminated for all mixtures in the dataset. This prevents the extinction cross sections from being different sizes.

Once solutions were estimated for  $\alpha(\lambda)$ , the third optimization estimated the two scalar parameters. Instead of using the trust-region reflective algorithm as in step one, a look-up table was instead generated. Reflectance mixtures were calculated using the NEFDS forward model with every possible combination of the two scalar parameters as long as the values fell within their respective boundary ranges. Each mixture reflectance was compared to the physically measured mixture reflectance using a point wise sum squared difference formula. The combination of scalar parameters that best minimized the sum-squared difference between measured and modeled results were surmised to be the correct scalar parameter values. Combined with  $\alpha(\lambda)$ , these three parameters de-



scribe physical properties of contaminant laden mixtures as estimated from the mixture measurement and the NEFDS model.

Many times, a non-linear optimizer will find a local minimum where results appear to be acceptable, but in reality a better global minimum may exist. The first optimization process undergoes multiple trials that randomize starting locations in order to reduce local minimizations. Starting points are randomized by selecting a starting point from a random number generator seeded by the clock time. For this experiment, the number of starting locations varied between one and one hundred starting locations per run. Having more randomized starts than that increased computation time exponentially, but did not appear to dramatically improve results.

Once model parameter estimation was completed, estimated parameter values were used as inputs into the original forward version of the NEFDS contamination model to cross check with measured reflectance mixtures. Five parameter inputs are used in this final step:  $R_s(\lambda)$ ,  $R_c(\lambda)$ ,  $\alpha(\lambda)$ ,  $\beta$ , and  $\frac{n}{A}$ . The output result for each case is the intimate mixture reflectance spectrum converted into emissivity that should be a perfect match to the measured spectrum.

It is important to note that in each of the optimization steps within the parameter estimation algorithm, parameter boundary conditions are in place. These conditions bound the potential estimates to realistic values. In the case of the coverage density, the boundary conditions match those in the NEFDS forward model of 0.001 - 0.0125  $\frac{g}{cm^2}$ . The extinction cross section was given non-negative boundary conditions up to 200  $cm^2$ . Since the rate of change in the effective packing fraction ( $\beta$ ) acts as a fitting parameter with units of area, the boundary conditions were not clearly defined by literature. Currently, this parameter is set to non-negative values up to a value of ten. Recent analysis indicates that this parameter can likely be set with a maximum that is two orders of magnitude larger based on unit analysis without having significant impact on the magnitude of other estimated parameters.

An additional property can be computed from the parameter inversion model results that can estimate the mass present on the surface using coverage density. This can occur by using an assumption that the powder material was deposited with an relatively equal distribution across the area of the sieve. Simple mathematics computes total mass as

$$M_{Total} = \frac{n}{A} * A_{Sieve} \quad (4.4)$$

which uses the coverage density and sieve area. The product of the two parameters

results in units of grams as desired and represents the derived mass for the mixture. The sieve area used to calculate the measured mass has a diameter that is seven inches wider than the IFOV of the instrument sensor where the measurement occurred. If there is uneven application across the sieve area as opposed to the sensor IFOV, the derived total contaminant mass will be over or underestimated. Both are equally possible as sparsely contaminated surfaces are rarely equally distributed over large areas.

### 4.3 Direct Cross Section Measurement

In the NEFDS contamination model, the extinction cross section (or just cross section) is used to calculate the mixture spectrum between two materials. This parameter only references the extinction and scattering of the contaminating material per wavelength and therefore should be consistent regardless of the amount of material on a surface. Several attempts were made to directly measure the extinction cross section parameter from various powder materials. Since direct measurement of this parameter is a novel idea, improvements were made to each iteration of the experiment and are documented in this section.

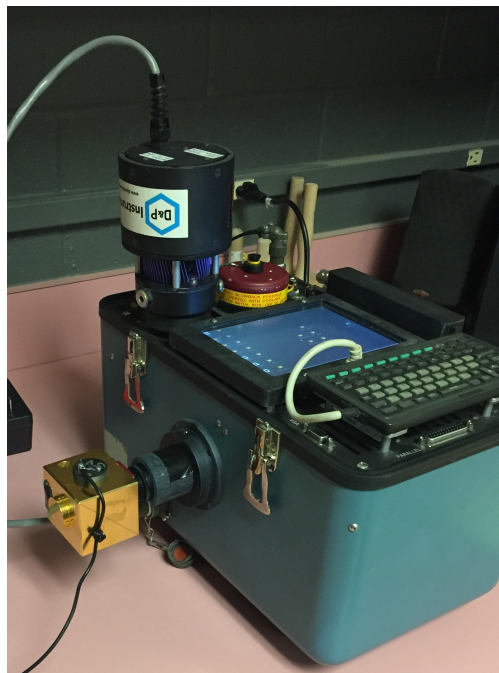


Figure 4.8: Labsphere 2 inch infragold integrating sphere.

As seen in Figure 4.8, the integrating sphere was initially directly attached to the instrument optic of the D&P via a 3-D printed connection piece. Direct attachment was supposed to eliminate any transmission loss from the gold mirror foreoptic and improve overall signal. This was thought to be important since the radiance levels being measured were low, however it was later determined that the foreoptic was needed to disperse an internal cool reflection from the liquid nitrogen dewar.

### 4.3.1 Light Source

Since the measured cross section will be entirely contained within the infrared spectrum, a light source had to be chosen that could contribute significant energy in that range. The original light bulb provided in the sphere was a electronic light bulb and not adequate in either wattage or in measurable energy in the longwave infrared range. A new bulb purchased from Electro-Optical Components was used instead called the EK-537X steady state IR emitter. This bulb has a radiating temperature around 1173 Kelvin (900 celcius) and 2.4 Watts of power. The wavelength of maximum radiating temperature was around  $2.5 \mu m$ , but the overall contribution in the longwave infrared range was significantly larger than the previous bulb.

A major hurdle to measuring electromagnetic energy across the longwave infrared range with a light source is that the bulb must reach a thermal equilibrium with its environment for consistency. Experiments were performed to determine when this ideal time should occur. As apparent in Figure 4.9, the light source does shift upwards over time, but after approximately two hours, the rate of change in radiance is insignificant. Figure 4.10 demonstrates this at several wavelengths in the spectral range of interest and seems to indicate that after the first hour, there is little variation in signal within the integrating sphere.

### 4.3.2 Integrating Sphere Experimental Design

In the first rendition of the experiment, powder was placed inside an output port cap in two amounts and packed into the same volume of space. Each amount would produce a different number density as the mass shifted but each was contained in the same volume. Measurements of the radiance from the pristine sphere as well as the sphere with both amounts of material inside were measured. Two ratio values at each wavelength were produced from these measurements.

Using equation 3.12, a wavelength-by-wavelength profile of the negative logarithm of

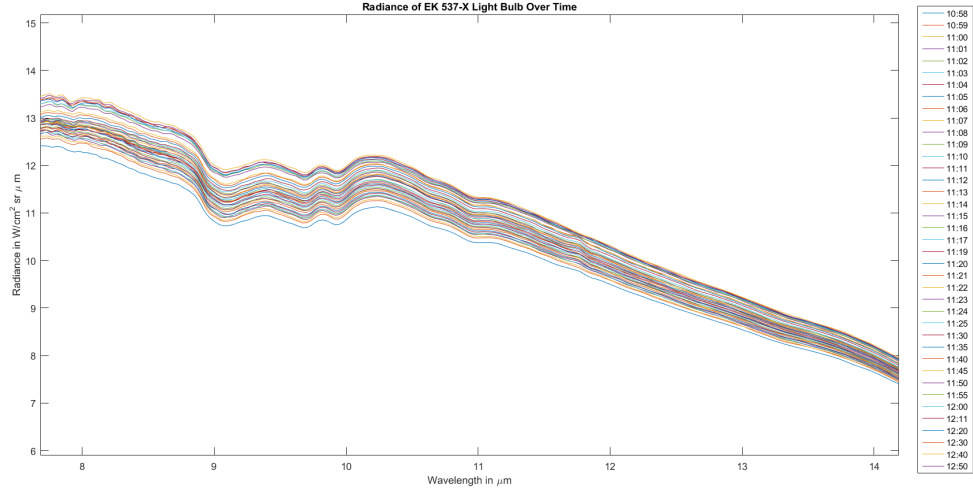


Figure 4.9: Measured radiance at intervals across two hour period for EK-573X IR emitter light bulb

that ratio per measured number density was produced. In theory, this semi-logarithmic plot should have created a straight line with a near zero intercept at each wavelength. The slope of the line would represent the extinction cross section at a specific wavelength and the cumulative build-up of these slopes would represent the entire spectral parameter. In an ideal situation, a direct cross section measurement should closely correlate to the estimated cross sections from the parameter inversion model in both spectral shape and magnitude. This would help confirm the fidelity of the model and allow for the insertion of the measured cross section into the parameter inversion model and remove a point of error from the scalar parameter estimates.

Unfortunately, due to the size, depth, and shape of the cap, it was nearly impossible to pack varying amounts of contaminant into the same size area with any level of certainty. The cap has a half inch diameter circular area with a depth of 0.03 inches. With a volume of 0.0966 cubic centimeters, the region where contaminant is placed is extremely small and high levels of uncertainty exist. A solution to this problem is to create a stable, consistent density layer by pressing the material into compressed disks.

The benefit to creating compressed disks of material instead of dumping and packing powder into the cap of the integrating sphere is that densities are well known and disks can be placed at any orientation inside the sphere without spilling over. In the

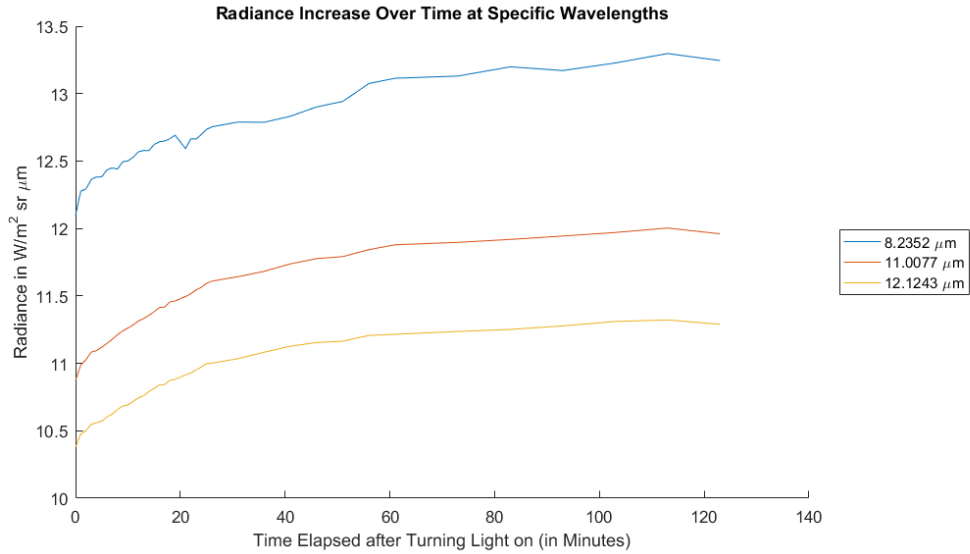


Figure 4.10: Radiance shift at three wavelengths over two hours for EK-573X IR emitter light bulb.

integrating sphere setup, a disk can be placed vertically in the port directly in line with the foreoptic of the instrument or placed between the foreoptic and integrating sphere directly. In the case of both experimental designs, the radiometry is the same because the light originates within an integrating sphere. Secondary reflections are trivial in magnitude to the transmitted and direct reflected energy interacting with the sphere.

Another benefit to measuring the radiance ratio of disks is that a third experimental design is possible. Instead of using an integrating sphere with disks of varying contaminant density, those same disks can be placed directly on the foreoptic of the instrument while facing a blackbody radiation source. Disks were held with a lens holder at close proximity to the foreoptic lens and near the CI SR-80 blackbody radiator. Electromagnetic energy reaching the sensor was transmitted through the disk of pure potassium bromide or contaminant mixture. This situation does not contain a large contribution from secondary reflections or disk emissivity because the disk is only present in the experimental design for a few seconds so as not to be influenced by the radiating temperature of the blackbody source.

### 4.3.3 Disk Making

In order to make disks with varying densities of contaminant materials, a binder was required that held the powder together under immense pressure while not affecting the incoming signal. The best options for materials that have these characteristics in the longwave infrared are several types of salt. More specifically, potassium bromide (KBr) powder, which is highly transmissive from  $0.25 - 25\mu m$  is the most commonly used binder substance. Potassium Bromide powder was purchased from Sigma-Aldrich and had 99.99999% purity, which constitutes laboratory grade spectrophotometric salt. Although potassium bromide is mostly transmissive in the longwave infrared, it is also hygroscopic, therefore its signature can be easily disrupted by water absorption that permanently degrades the disk quality.

Both contaminating materials as well as the potassium bromide salt were ground with a mortar and pestle until reaching a fine powder state. Grinding each material into this state brought the particle size of both materials to the same level and allowed the materials to mix intimately and evenly throughout the sample. Prior to making the disks, the potassium bromide along with all other contaminant materials were independently placed in a industrial scale drying oven for 36-48 hours at 110 Celcius. Placing them in conditions above the boiling point of water for long periods of time ensured that there would be no water vapor absorbed by the sample that could degrade the disk signature. Following the extensive drying process, the materials were immediately placed inside a thick sealed plastic bag with desiccant packs that absorbed atmospheric water vapor and kept samples dry. The samples were then transferred to the material science laboratory to prepare for the disk pressing process.

Since the radiance of several density levels needed to be measured for each material, a high end scale with the capability of accurately measuring to one ten-thousandth of a gram was used to measure the materials. At high contaminant amounts, binding the material into a disk was difficult. Therefore, disks were made with amounts less than 20% contaminant to 80% potassium bromide. In chemistry, IR spectroscopy indicates that disks should be 0.2-2% material with the remainder being KBr, but even with a high end scale, lowering the amount of material to that level is extremely difficult.

Disks were created with an X-Press 3630 hydraulic press as seen in Figure 4.11. This press has the ability to apply up to 40 tons of evenly distributed force onto a surface for a pre-programmed amount of time. Several different size options were available for this hydraulic press made with 13, 32, and 40 millimeter diameter dye casts. Disks could



Figure 4.11: X-Press 3630 40 ton disk press.

be made up to 10 millimeters thick, but ideal sizes ranged from 3-5 millimeters. Each size disk required different forces for slightly varied amounts of time in order to achieve similar results. Disks that were 40 millimeters needed 30 tons of force, while the 13 millimeter disks only needed 6 tons.

For this experiment to be valid, density needed to vary, but the volume of space the disk contained could not. Therefore, disks were calculated to have the same height for each contaminant ratio. First, the volume of space was determined by finding the cubic centimeter volume for the desired height. The volume density of the potassium bromide binder was then used to calculate the amount of that material which would be necessary to encompass the disk space. To incorporate the contaminant into the disk, a percent volume was selected and the mass of the binder at that volume percentage was found and removed from the total. Then the density of the contaminant was multiplied by this removed volume to calculate the amount of contaminant to add without changing

the size of the disk.

The materials were measured and combined in a container where they were shaken up for several minutes to ensure that the materials were properly combined. That mixture is then placed inside a dye cast for pressing. In ideal situations, a disk of just potassium bromide should appear completely transparent when removed from the dye cast. Transparency indicates that no air has been trapped within the disk and that the material and that no water vapor was absorbed by the binder material prior to pressing it. In practice, a perfectly transparent disk is difficult to achieve even when proper procedures are followed as water vapor is present throughout the atmosphere.

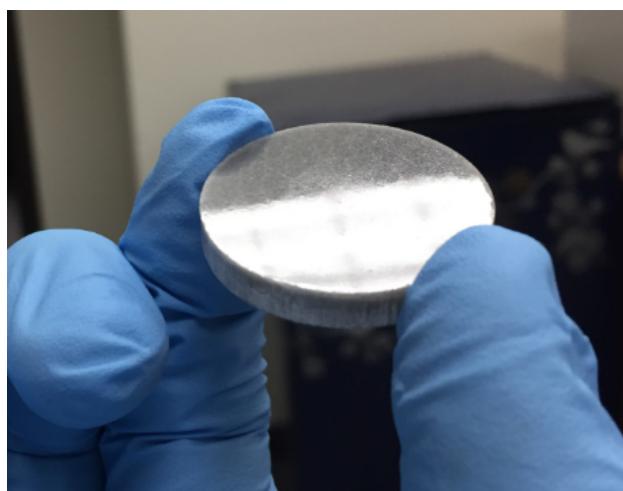


Figure 4.12: A disk compressed with silicon carbide powder and bound with potassium bromide.

Once placed inside the dye cast, the powder mixtures were pressed for 5-7 minutes depending on disk size. Following the compression period was a 3-5 minute period of slow decompression of the dye cast. This is done slowly because quick depressurization can cause structural deformities and cracks within the disks. Following the depressurization, the disks were removed from the dye cast and directly placed in a bag with large desiccant packs and sealed. This bag was then placed inside another bag with large desiccant packs and sealed. This is to ensure that any water vapor within the atmosphere is not absorbed by the hygroscopic mixture of potassium bromide with the contaminant. After long periods of inactivity, the disks were placed in the drying oven for several hours to bake off any potential absorbed water vapor.



## 4.4 Scene Simulation

After real measurement collections have occurred and been tested with the parameter inversion model, similar recreated mixtures can be modeled using a simulation tool like  $\mu$ DIRSIG. This powerful simulation tool can confirm the viability of the parameter inversion model estimates for contaminant mass. Surface mixtures are created in Blender based on material properties of the substrates and powder contaminants found using the scanning electron microscope images to create particles.

The Blender mixture recreation allows for known randomized placement of particles, indicating that the placement of particles is such that a large group can be removed in the data file without changing the overall distribution found in the scene. The intent of randomizing particle placement is to be able to adjust the coverage density without concentrating particles in a single portion of the substrate area across the field of view. This may have a subtle effect on the  $\beta$  parameter, but should not change the estimated coverage density.

The geometric properties applied to the powders in simulation originate from the scanning electron microscope (SEM) images, x-ray diffraction analysis of the powder's crystalline structure and analysis of the technical data sheets. From this information, good estimates of the particle size distribution and particle shape can occur. X-ray diffraction data contributes to determining the correct optical constants to apply to each material in the actual simulation. In lieu of a database of known constants for any of the materials, a compressed disk of each of the materials with potassium bromide binder were sent out to JA Woollam in Lincoln, Nebraska. JA Woollam has a special longwave infrared ellipsometer that can directly measure the optical constants  $n$  and  $k$  for each material. While  $k$  is not directly used in  $\mu$ DIRSIG, it can be used to calculate the absorption coefficient by using

$$abs = \frac{4\pi k}{\lambda} \quad (4.5)$$

where  $\lambda$  is the wavelength at each  $k$  value in units of centimeters. Once the absorption coefficient is determined,  $\mu$ DIRSIG can model the scene geometry for a mixture spectrum. Due to unforeseen challenges in obtaining the index of refraction information, data for similar products from other customers was provided by JA Woollam instead of the exact materials used in this study.

## 4.5 Signature Injection

The collection and analysis of airborne hyperspectral imagery with target signatures present is useful in examining the fidelity of the concepts developed in laboratory and field experiments. These types of experiments are typically placed under ideal conditions, where real world effects such as atmospheric contributions, scene occlusions and other conditions may change desired results. Target rich airborne data is also useful in the assessment of detection algorithms when the desired targets are well characterized at ground level. In most cases, available hyperspectral data either does not contain pertinent target signatures or signatures exist, but are not well characterized at ground level. When airborne data available without targets, one method that can be employed is to inject synthetic targets within the scene using intimate mixture modeling.

Assuming the comparison between the empirically measured spectra and the parameter inversion modeling was reasonably successful, the parameter estimates from this step can be used to inject these targets into the longwave hyperspectral scene. Airborne data was provided from the Blue Heron longwave hyperspectral sensor of a collection undertaken in the fall of 2015. The Blue Heron sensor is a 256 pixel linescanner with 250 bands in the longwave infrared ( $7.5 - 13.0\mu m$ ). Unlike standard linescanner, the Blue Heron sensor is attached to a gimbal or turret and flies circularly around a target point. Because measurements are taken around a point, the imagery appears georeferenced or orthorectified imagery despite not being either. Provided data has a sensor ground sample distance (GSD) of  $0.25m^2$ .

Airborne data was first converted into surface emissivity space through the longwave atmospheric compensation tools in the ENVI software program. Once an emissivity space map was obtained, the hyperspectral data was converted into reflectance space with Kirkoff's law. Hyperspectral scenes were chosen based on the availability of large uniform surfaces such as parking lots or sidewalks within the scene. Large areas were needed to place as many targets of varying condition as possible. The example scene used for this experiment contained a parking lot that occupied approximately 30-40% of the entire image. Physical property estimates ( $\alpha(\lambda), \beta, \frac{n}{A}$ ) from the parameter inversion model combined with the hyperspectral scene reflectance signatures as well as the measured pure contaminant signature to create an intimate mixture. Each target was created as a 3x3 block of pixels on a parking lot surface from the airborne data. Each of the three rows of target blocks represented a different coverage density parameter, most empirical datasets had three discernible coverage densities. Each column of tar-

get blocks represented a variation of sub-pixel fraction. Ten columns of target blocks existed; the right-most column was a full pixel representation of target mixtures. Each subsequent column to the left lowered the sub-pixel fraction by 0.1 (some renditions of this created sub-pixel fractions that decreased in different amounts). Once completed, a synthetic target map contained 27 3x3 target blocks, each using a unique combination of coverage density and sub-pixel fraction. Finally, the targets were blurred and turned back into emissivity space.

Every hyperspectral map underwent target detection using the adaptive cosine estimator (ACE) algorithm and several different types of targets. Since each target block contained unique features, performing a target detection algorithm on the scene with different types of targets should be informative as to which type of target worked best in each situation. Four target signatures were used for target detection analysis; the pure target spectrum from experimental measurements as well as three emissivity signatures created with the NEFDS forward model. To make target spectra more realistic to the scene, the substrate signatures from the experimental dataset was replaced with an average spectrum from 16 pixels of the parking lot surface in the airborne scene.

## 4.6 Signature Injected HSI Data

An opportunity arose in November of 2016 that allowed for the collection of airborne longwave hyperspectral data from the same Blue Heron sensor that was used for signature injections, where targets could be deployed onto the surface being measured. This was the ideal situation as targets were actually in the scene and ground based reference data was collected to compare to the airborne collection. Measurements were made using the Designs and Prototypes 102F FTIR during the airborne collection. Target detection algorithms similar to the ones performed in the simulated data were carried out on the real data and a preliminary assessment was made on this data.

Another benefit to this data collection was that it provided the chance to assess the point spread function of the sensor which was previously unknown. This was done by analyzing the line spread function created by the existence of a straight line of pixels where aluminum foil was placed to create target boundaries. The aluminum line was narrow enough to be sub-pixel and create the spread needed to assess the LSF and PSF. The point spread function is simply a three dimensional representation of the line spread function. The importance of obtaining the point spread function was that synthetic targets injected into the scenes from the 2015 collection could now be blurred

to the correct optics of the sensor. Without this blur, all targets would appear without the effects of the sensor optics wavefront limitations and look out of place relative to the background scene. The calculated point spread function was a 5x5 matrix that is two pixels wider than the target blocks. This means that all target pixels will receive contributions from background pixels due to the sensor optics. In the case of target block edge and corner pixels, the contribution will be exceedingly larger.



## Chapter 5

# Results

This chapter presents and discusses the results that have been achieved during the course of this study. Most of the work focused on obtaining physical parameter estimates from the inversion model that was created from the NEFDS contamination's forward model. These parameter estimates lead to the derivation of total contaminant mass present on the surface. Improvements to the model were attempted through direct measurement of the wavelength dependent extinction cross section term. Target detection analysis of the mixture signatures injected into airborne data was performed to determine best practices for the ACE detection algorithm when attempting to detect small levels of powdered contaminant on various surfaces. Longwave airborne imagery containing real targets was also analyzed using target detection algorithms and the mass estimation method presented above. An assessment on the consistency of measurements with the FTIR instrument is also presented.

For the first summer of data collections, contaminant mass knowledge was unavailable due to the lack of a scale with high enough resolution. Inversion model results under these conditions were placed in an appendix as they can be informative to the model, but cannot be confirmed with reference data. For all results shown below, mixture spectra without reference data on the mass amounts were labeled numerically from least to most contamination (least contaminant present is 'Mixture 1,' most contaminant is 'Mixture n'). Results discussed in this chapter do contain measurements of the contaminant mass for each collected spectrum. A mixture in this case is considered a substrate surface that contains a contaminating material, not a physical mixture of two materials.

## 5.1 FTIR Instrument Analysis

### 5.1.1 Blackbody Characterization

In order to properly characterize the D&P FTIR system, measurements were made to examine the spectrum of a well controlled external blackbody source programmed to a specific temperature over an extended period of time. Blackbodies are designed to maintain a set temperature as defined by the user for long periods of time so that radiating electromagnetic energy can be used for calibrating an instrument. This particular experiment utilized an in house CI SR-80 blackbody set to 297.15 Kelvin where measurements were collected at small temporal intervals over three straight hours. This time scale allows for the identification of any significant thermal drift in the FTIR instrument. As evident from Figures 5.1 and 5.2, the measurements of the blackbody over this time scale demonstrated consistency not only in the longwave infrared, but across the entire instrument spectral response. Because the blackbody can be programmed to the hundredth of a degree ( $2 - 15\mu m$ ) and essentially remains locked in place without variation except for subtle drift correction, any deviation between spectra can be considered a result of error within the FTIR. In the peak wavelength range (around  $9.6\mu m$ ), the variation in the data remains small. Using equation 2.3 along with the set temperature, the calculated peak wavelength for the blackbody should be  $9.752\mu m$  and given that the blackbody has not been calibrated in several years, a small deviation from the set point is not surprising.

A calculation for the standard deviation of the instrument radiance measurement over the three hour time interval was also computed in Figure 5.3. The standard deviation can be described as roughly equivalent to the average distance to the mean spectrum at each wavelength. In Figure 5.3, the standard deviation never exceeds 0.1 radiance units at any point across the measured instrument spectrum. In the longwave infrared range ( $8-14\mu m$ ), the standard deviation was less than 0.2 radiance units. This indicates that on average, each wavelength has essentially the same value for the entire three hour time interval and almost no error exists in the instrument. This was further supported by Figure 5.4 which shows the calculated variance or spread in the data at each wavelength. The variance in the longwave infrared range was calculated to be essentially zero.

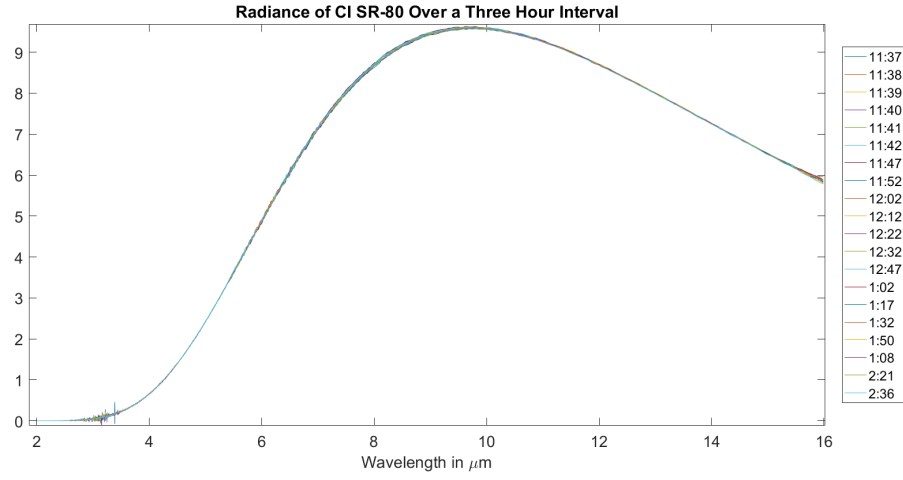


Figure 5.1: Measured Radiance of a Blackbody Using the CI SR-80 blackbody with the D&P

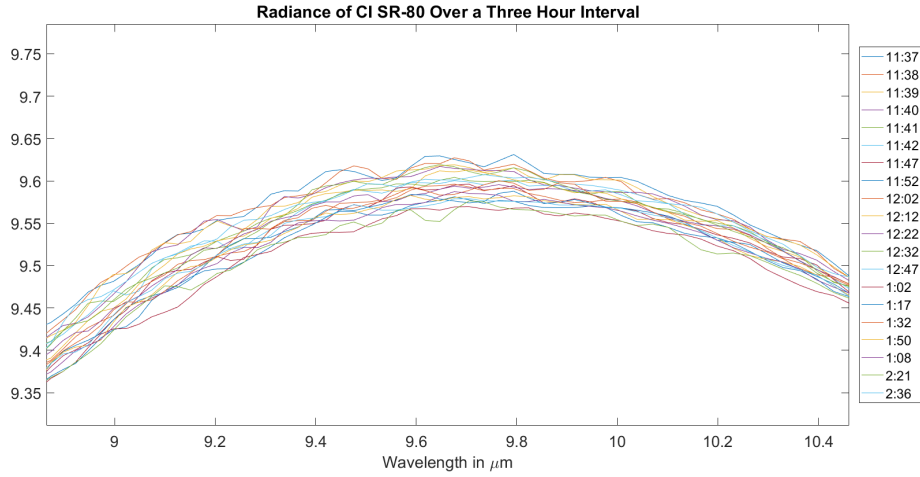


Figure 5.2: A close up look at the location of peak blackbody radiance for each time interval measurement using the D&P.

Finally, peak wavelengths for every blackbody measurement were determined and plotted relative to the elapsed time from the initial measurement. This was performed to establish if there was a consistent directional thermal drift occurring in the instrument. The maximum wavelength varies from  $9.65\mu m$  to  $9.8\mu m$  between all measurements which translates to blackbody temperatures between 296.15 and 300.15 degrees, but no trend



was seen. Overall, the measurements indicate that the FTIR instrument is incredibly consistent from measurement to measurement and that any error is likely a result of another aspect of the measurement process. It also indicates that there is no consistent thermal drift in any direction as the peak wavelengths do not shift in one singular direction. Despite this low error, precautions were put in place to ensure power fluctuations from the building did not incidentally cause variations in the measurements. When this FTIR instrument was used in a laboratory setting, its power source was connected to a high end power regulator. In field settings, the instrument was connected to high quality charged batteries and the voltage was closely monitored. In addition, after the summer of 2015 collection, the instrument was sent for a much needed recalibration and upgrade. This reduced the error associated with normal wear and tear of instrument use.

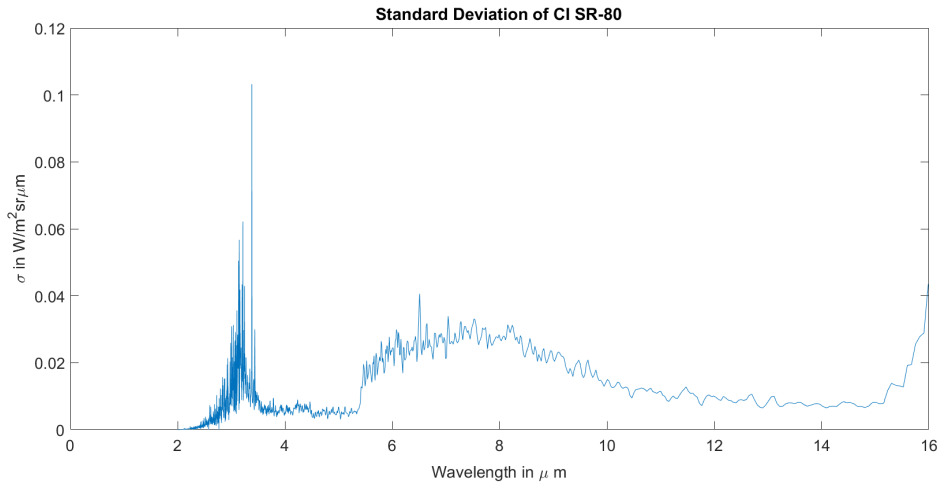


Figure 5.3: Calculated standard deviation for the blackbody as measured by the D&P

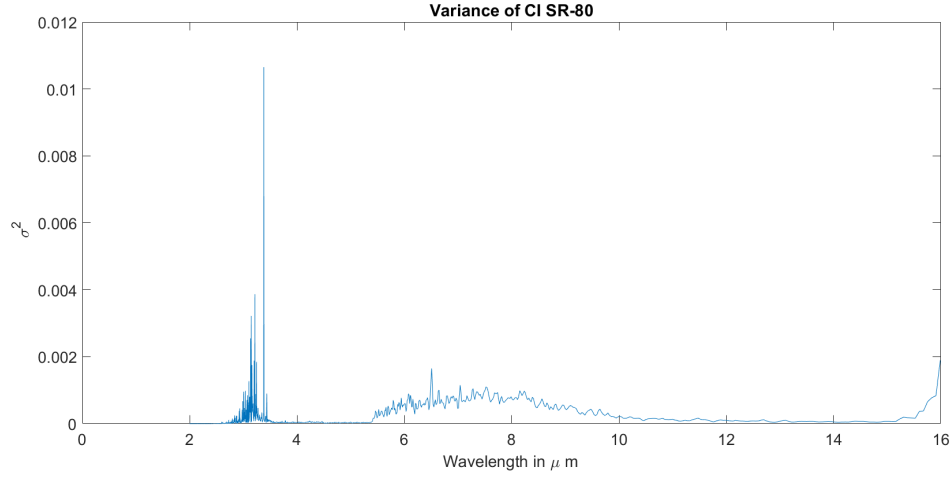


Figure 5.4: Calculated variance of the blackbody radiance for the D&P

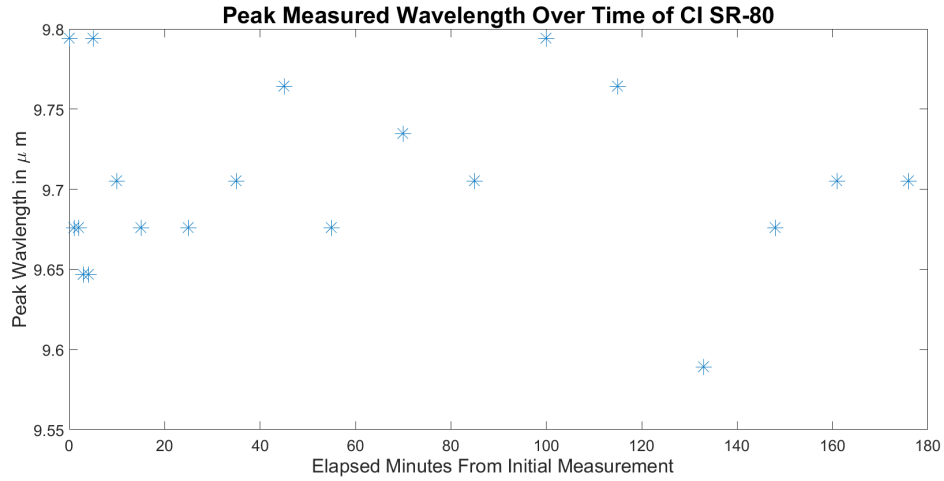


Figure 5.5: The measured peak wavelength of the CI SR-80 blackbody measured by the D&P

### 5.1.2 Effect of Nitrogen Dewar

During an investigation into potential direct measurements of the extinction cross section parameter, it was discovered that when removing the foreoptic of the instrument, the radiance increased in a contaminated sphere as opposed to a pristine one (experiment described in detail below). This is counter-intuitive as the materials used had a lower

reflectance than the infragold found on the surface of the sphere. This is attributed to an outside influence breaching the closed system. The belief was that this error occurred due to experiment design. When the location of the material disks were moved to be directly in-line with the sensor, the effects were reduced. This led to the idea that there were internal reflections occurring from the liquid nitrogen dewar, which sits just behind the sensor. It is likely that the foreoptic mirror which was removed from the set-up dispersed internal reflections from the dewar away from reaching the sensor. When this mirror was removed, the internal reflections from the dewar were reverberated back towards the sensor by the highly reflective integrating sphere surface. Therefore the foreoptic was included in the direct extinction cross section measurements.

## 5.2 microDIRSIG Modeling

The purpose of examining the  $\mu$ DIRSIG simulation tool was to see if a first principles ray tracing model could effectively create emissivity mixtures with clearly defined surface conditions that could be used as a comparison to the estimates found with the parameter inversion model. If they were capable of creating similar mixtures, then measured data could be foregone for spectra with isolated characteristics for a more rigorous study. Ultimately, the largest challenge in the operation of  $\mu$ DIRSIG is the acquisition of the complex index of refraction for the materials in the longwave infrared range. Typically, a database of  $n$  and  $k$  data will not have information outside of the visible and near infrared range. The only commercially available index of refraction data found for any material in this research (hexagonal silicon carbide) had  $n$  values fall below one at critical wavelengths, indicating that light was actually speeding up as it passed through the material. Since this is not physically possible, the only other option was to attempt to directly measure the properties.

Johnson (2017) described several methods for which this could be done, however the most realistic option given instrument availability was to send compressed disks of material out to JA Woollam to be measured with an ellipsometer. Measurements from this instrument failed in part due to the preparation of the compressed disks of material. Powders were not ground into small enough particles using a mortar and pestle for the mixture of the contaminant and binder to be homogeneous. As a result, ellipsometer measurements were not measuring the contaminant, but a conglomerate material of potassium bromide particles and contaminant particles. Another issue that occurred was that some disk surfaces has slight bowing which prevented optical alignment in the

ellipsometer. This was an unforeseen error as the bowing of the disk was not visible to the naked eye. Ultimately, the measurements did not work, but measured properties of very similar items from other customers were provided in place of failed disk measurements.

Complex index of refraction data was provided for two materials, fused silica and silicon carbide powder, but both occurred as wafer materials instead of powder disks. Refractive index measurements provided by JA Woollam were made in-plane of these wafers, but beyond this knowledge, no other information was available from the company. Attempts to run a  $\mu$ DIRSIG simulation with the complex index of refraction data provided by the company proved to not be successful for a number of reasons. The silicon carbide simulations were not successful as the provided data did not match a known partial index of refraction match from a database and therefore would not have been a representative signature. Fused silica failed in the simulations as the model setup did not contain enough photons to generate a complete signal on the entire array. Unfortunately, the buildup of signal was not improved upon when adding additional photon bounces and adjusting the array.

The acquisition or measurement of full spectral complex index of refraction data could prove to be a promising future work project to obtain necessary information that can perform first principles simulations of surfaces with controlled properties. Until this information is easier to acquire, simulating contaminated scenes in the longwave infrared range will remain a challenge.

### 5.3 Direct Extinction Cross Section Measurements

In an attempt to reduce the complexities surrounding the parameter inversion model described in Chapter 3, attempts were made at directly measuring the extinction cross section parameter. This parameter is material specific and does not rely on variation in contaminant amount as a modulation tool. The direct measurement of the parameter would allow for the removal of two of the three steps necessary in the inversion model. Direct measurements were completed through the creation of disks with different densities of contaminating material in them and measuring their radiance changes as explained in Chapter 4. Initially the measurements were undertaken inside a two inch diameter infragold integrating sphere from Labsphere, however this design later shifted to looking through a blackbody source. Results from both methods are presented below.

### 5.3.1 Integrating Sphere Measurements

The extinction cross section estimates present the largest hurdle to good estimations for the coverage density parameter. Since the extinction cross section has wavelength dependencies, the inversion algorithm needed to dedicate two separate steps and valuable computation time to help determine its value. The direct measurement of this parameter would simplify the method and help reduce the computation involved by directly feeding a parameter that is consistent regardless of mixture.

As discussed in Chapter 4, the initial experimental design used an infragold black-body with a strong thermal emitting light to try and extract a single extinction cross section. Disks of several different number densities were placed inside the integrating sphere and their radiance ratio with the pristine sphere was measured. At each wavelength, the ratio for each disk was input into equation 3.13 and plotted on a semi-logarithmic plot. The slope of the line created by the semi-log plot represents the extinction cross section at that wavelength, and the intercept should be zero although error does exist in calculations.

The measured radiance ratios for two amounts of silicon carbide powder in the integrating sphere can be seen in Figure 5.6. Both ratios are slightly greater than one in this example; this occurs as a result of an internal reflection from the liquid nitrogen dewar reflecting off the surface of the integrating sphere (described above). Since infragold is highly reflective, the energy from this internal reflection returns and reaches the sensor. This became more apparent when the disks were moved from the bottom of the sphere to directly in-line with the sensor. In this setup, the ratios dipped slightly below one, but were still adversely affected by the reflection. Once the foreoptic was placed back into the optical system, the internal reflection was dispersed without issue.

Despite having solved this problem of internal reflections adding undesired signal to the ratio measurements, additional problems remained in the design. Placing disks inside the infragold sphere meant that the sphere was occasionally handled and opened, changing the thermal characteristics of the sphere. Since the light takes multiple hours to reach thermal equilibrium, any handling of the sphere or exposure to the outside air will change its properties and have an effect on the measurements. This is especially true given the low nature of the signal applied by the light source.

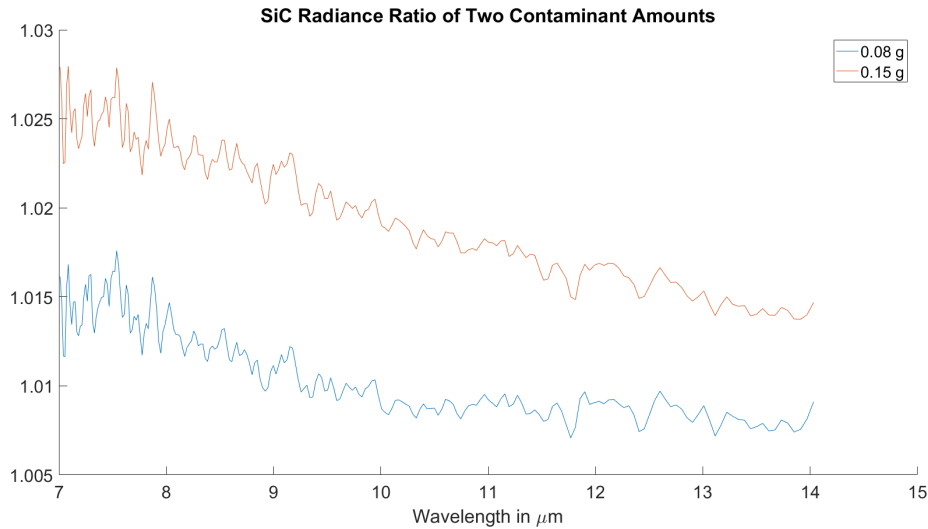


Figure 5.6: Radiance Ratio between the pristine integrating sphere to one with two amounts of silicon carbide contamination.

An example of the type of issue that can occur due to using an integrating sphere can be seen in Figure 5.7. Red chalk powder was added in low percentages to potassium bromide disks and measured inside the integrating sphere. This design incorporated the changes mentioned to account for dewar reflections. Despite having clearly defined differences in number density, the ratios do not behave linearly. Physically, unless the material added to the sphere is more reflective than the surface of the sphere, the ratio should decrease with added material. In Figure 5.7, the lowest ratio appears to occur in the disk with the lowest percentage of contaminant. The expected behavior should be a decreasing ratio with increasing contaminant percentage as more energy will be scattered in higher density layers. These errors are a result of the internal environment (i.e. temperature) of the integrating sphere being inconsistent due to the need to replace disks by opening the sphere.

Despite only one example being shown, almost every collection of the disks had this phenomenon occur where ratios stayed below one, but failed to follow a standard trend. Several efforts were made to simplify the process using the integrating sphere, however nothing significant could be done to fix the process without making it unviable.

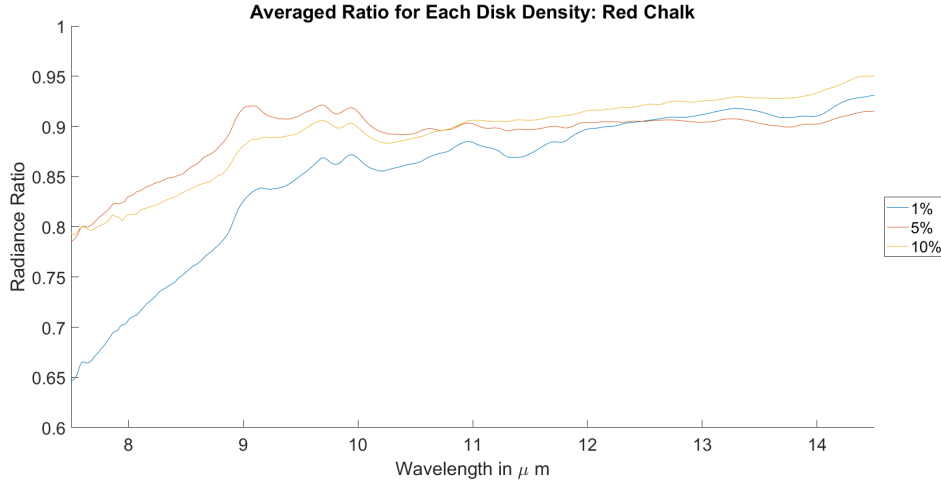


Figure 5.7: Extinction

### 5.3.2 Blackbody Measurements

Given the failures of the previous design, the promise of success in examining the cross section with a blackbody was obvious. The CI-SR80 blackbody could provide a significantly stronger signal than the integrating sphere light bulb could while not requiring much time to reach equilibrium. An optical lens holder could be used to hold a disk such that the foreoptic of the instrument could be completely covered by it with a tight seal. Disks were made to be 40 mm in diameter while the foreoptic of the instrument is just 25.4 mm. Staring through the disk towards a blackbody radiation source would measure the radiation loss between a disk without contaminant from a disk with contaminant. Since the blackbody could be set to a specific temperature and remain there indefinitely, a temperature of 50.00°C was chosen and the disk was placed as close as possible to the source. This temperature produced a peak exitance around 9 μm and a stronger signal than found in the sphere light bulb. Because the disk would be present for a short period of time, the energy emitted by the disk itself has a negligible effect on the measurement due to its relative temperature to the blackbody and should not need to be accounted in the final computation.

#### Fused Silica

For this experiment, four, 40mm diameter disks were created with 0.042, 0.0869, 0.1305 and 0.1741 grams of fused silica and the remaining volume containing potassium bromide

binder. Because all disks were designed to be the exact same dimensions (3.5 mm thick), each contained a different number density. As a percentage, the fused silica in the three disks represented 0.5, 1.0, 1.5 and 2.0% of the total amount of material present. Radiance was measured of the blackbody through each disk as well as a disk of just binder material and used to calculate a single spectrum extinction cross section. Since the experiment only placed the disk in the lens holder for a few seconds and only measured photons that were transmitted through the disk, no secondary effects needed to be accounted for in the calculations.

Figure 5.8 shows the resulting extinction cross section for fused silica using the measured output from all four disks. If this spectrum were to be placed in the parameter inversion model, the model would fail. This is because the magnitude of this parameter is far too low and would force the estimated coverage densities for mixtures to exceed pre-defined boundary conditions. The NEFDS contamination model is only valid for low density mixtures approximately between 0.001 and  $0.01 \frac{g}{cm^2}$ . Slight divergence from these conditions may still have validity, but in order to accommodate extinction cross sections seen in Figure 5.8, the model would need to have validity for coverage density amounts at approximately  $0.1 \frac{g}{cm^2}$  or higher. In equation 3.8, it becomes clear that the main factors that have an effect on the final results are the coverage density parameter and the extinction cross section. Both parameters are found in the numerator of the exponential, while the  $\beta$  parameter can only be found in ancillary exponential terms within the main exponent. If the scale of the  $\alpha(\lambda)$  or  $\frac{n}{a}$  parameters is reduced, the other must compensate for this change. Because the measured extinction cross section parameters are an order of magnitude lower than inversion model estimates, compensation must occur in increasing the coverage density parameter.

### Red Chalk

Three disks were used for the calculation of the extinction cross section for red chalk powder with 0.0643, 0.1316, and 0.1964 grams of red chalk. A fourth disk would have been made, but the amount of powder left was too small to make a fourth disk. The three disks made represent between 0.5 and 1.5% contaminant by volume within the disk. Measurements of the extinction cross section can be seen in Figure 5.9. The spectrum calculated for the extinction cross section from these disks looks very similar to the emissivity spectrum found in empirical measurements for an optically thick layer



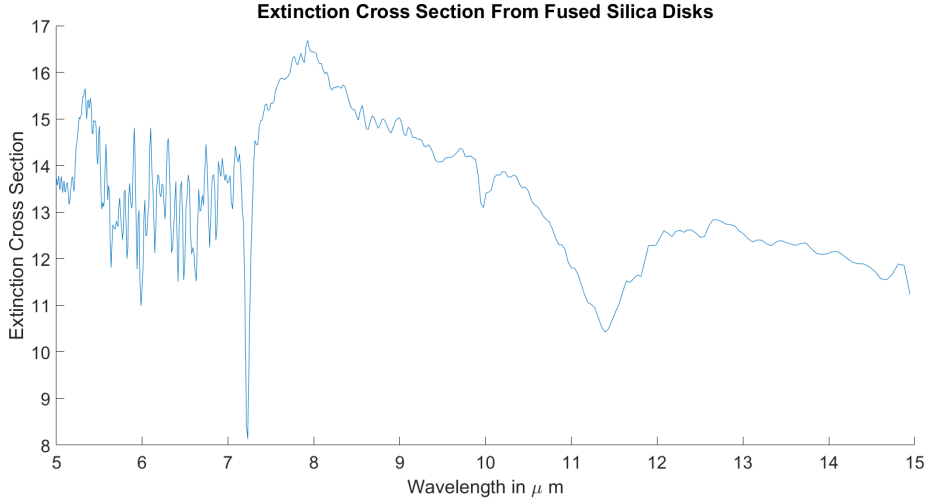


Figure 5.8: Derived extinction cross section parameter found from blackbody transmission measurements of compressed disks of fused silica powder.

of material. Like the previous example, the magnitude of this spectrum appears to be at least an order of magnitude smaller than what could be used in the model.

### Silicon Carbide

In the final example material, silicon carbide disks were measured with a blackbody using four different amounts of material per disk (0.0406, 0.1269, 0.1920, and 0.2549 grams). Unlike the example of red chalk powder, the calculated spectrum for the extinction cross section had no real similarities to its pure material spectral emissivity. Radiance ratio measurements for all four cases appeared remarkably close, regardless of contaminant amount present. This lack of disparity in ratio signatures may have resulted in a spectrally unremarkable signature for the extinction cross section. Like both previous examples, the magnitude results for the material are significantly lower than expected and could not be used in the inversion model.

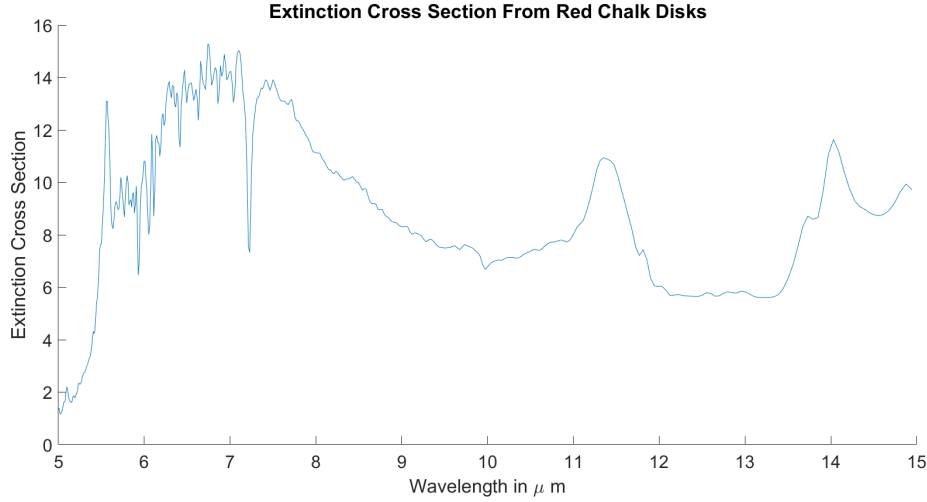


Figure 5.9: Derived extinction cross section parameter found from blackbody transmission measurements of compressed disks of red chalk powder.

### 5.3.3 Integration into Parameter Inversion Model

In an ideal situation, the measured extinction cross section should be able to be incorporated into the parameter inversion model and reduce the computational steps necessary to estimate the two other parameters ( $\frac{n}{a}$  and  $\beta$ ). Since the magnitude of the computed extinction cross section is too low and the only other parameter that can affect the magnitude has pre-defined conditions, the inaccuracy must exist in the measured extinction cross section.

Disks were made for this experiment to contain between 0.5% and 2.0% contaminant by volume. When broken down into area density, it appears that several of the disks had larger coverage densities than the forward model's boundaries for the parameter. As described in Chapter 3, substitutions were made in the model to address scenarios where the volume density parameter became insensitive due to particles being closely stacked. While extremely low, the amount of contaminant used in the creation of the disks could be too large to be used to calculate the extinction cross section parameter.

As a test of the fidelity of the calculations, the extinction cross section parameters were recalculated using only disks that had a coverage density within the boundary conditions of the forward model. In two cases (red chalk and fused silica), the only disk

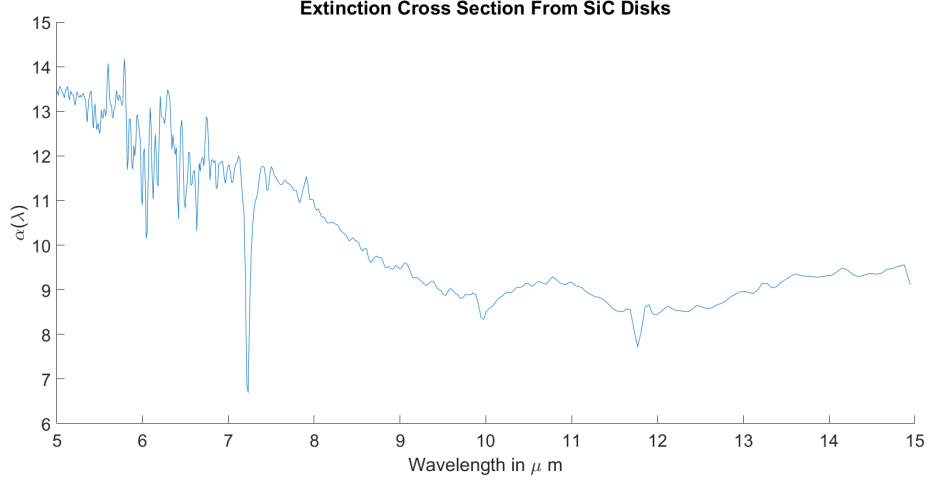


Figure 5.10: Derived extinction cross section parameter found from blackbody transmission measurements of compressed disks of silicon carbide powder.

used was the lowest density disk. Silicon carbide was able to incorporate the second smallest disk as well. To improve the fit of the model, an assumed y-intercept point at the zero point on the semi-logarithmic plot was added to the calculations. There should be no radiance shift between a pure potassium bromide disk and one without any added contaminant. Therefore the logarithm of the ratio should be zero at zero coverage density for all wavelengths. Adding this point improves calculations and forces data to behave in a physically realistic way.

When only incorporating the disks that fell within the area density seen for the NEFDS contamination model, the calculated fused silica extinction cross section increased five-fold from its previous calculation. The estimates in the LWIR section of the spectrum for  $\alpha(\lambda)$  were as high as  $80 \frac{cm^2}{g}$  at some wavelengths which was much closer in magnitude to the desired magnitude to run through the parameter inversion model, but still too low. These results are presented in Figure 5.11. Similar, but reduced improvements can also be seen in Figure 5.12 where the extinction cross section for red chalk powder increased in magnitude a very small amount, but nowhere near the amount necessary to bring it on par with the expected input for the parameter inversion model. The same is true for the silicon carbide disk results found in Figure 5.13 where estimates increase by a factor of three, but remained far too low for the inversion model.

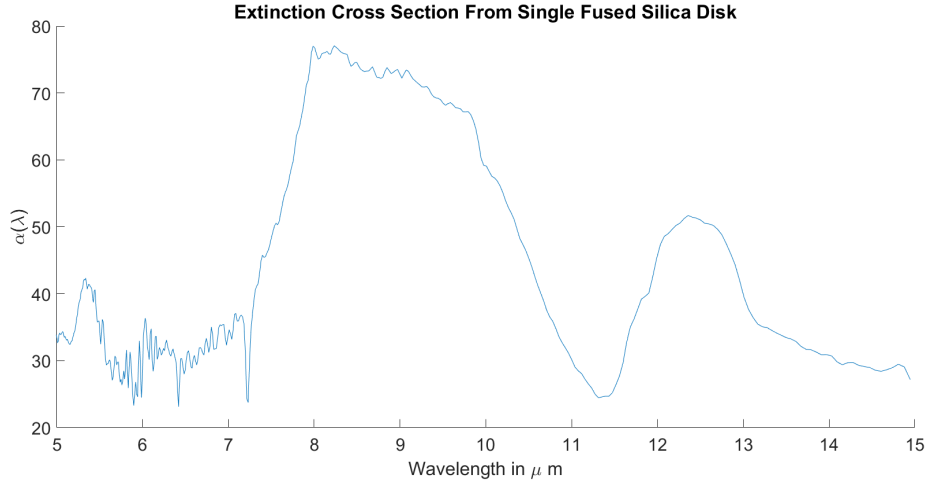


Figure 5.11: Derived extinction cross section parameter found from blackbody transmission measurements of lowest number density compressed disk of fused silica powder.

It appears that calculations for the extinction cross section parameter have a somewhat logarithmic quality to them. As volume density increases, the slope of the logarithm of the radiance ratio appears to decrease demonstrating the diminishing returns discussed in the NEFDS contamination model documentation. At volume densities within the boundary conditions of the density of the forward model, these results came closer to the inversion model estimates. If more disks were made at lower densities within this range, a better calculation could occur that more accurately reflected the results seen in the inversion model estimates.

Another possibility exists that because of forward contamination model units, the desired parameter is not the extinction cross section, but the extinction cross section per gram ( $\frac{cm^2}{g}$ ). To attempt to mitigate this, tests were conducted that used the number of particles as a substitution for grams in the calculations. This produced results that were on the order of previous computations or slightly smaller.

Finally, there is speculation that the compression of the material into disks may change its crystalline structure and therefore its material properties. Further analysis should be done on this aspect to ensure that the material properties do not shift when under this amount of pressure.

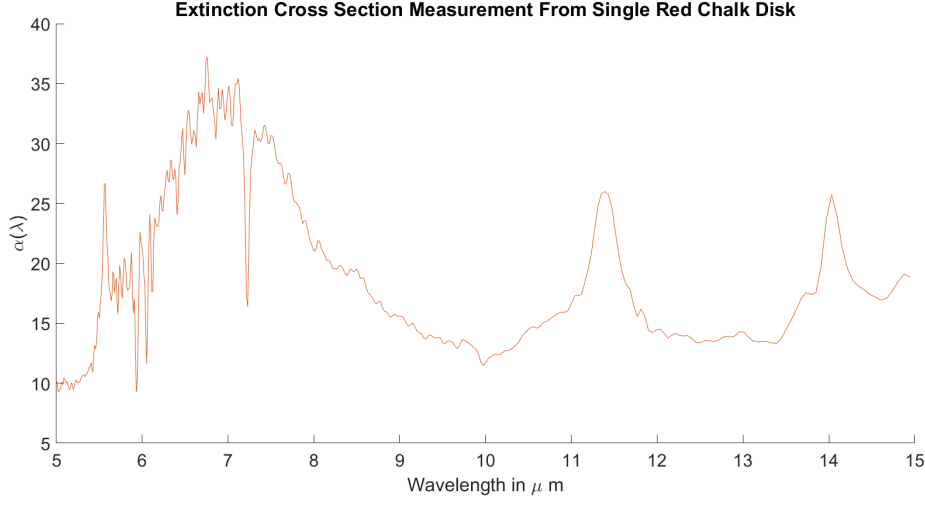


Figure 5.12: Derived extinction cross section parameter found from blackbody transmission measurements of lowest number density compressed disk of red chalk powder.

## 5.4 Parameter Inversion Estimate Results

As discussed in Chapter 4, a parameter inversion model was created to estimate physical properties of sparsely contaminated surfaces. This model used three spectral reflectance signatures as inputs (pure materials and a mixture spectrum). A process was put in place using a 10 inch diameter sieve to apply various amounts of contaminant to a surface for analysis. Contaminant mass amounts were measured during the application and allowed to reach thermal stability before spectral collections occurred. A total of five (in most cases) measurements were made for each data collection period. In addition to the three sparsely contaminated surface measurements were collections of both the bare pristine substrate and an optically thick layer of contamination. The five measured spectra were then input into the parameter inversion model to estimate physical parameters.

### 5.4.1 Scalability Test

To ensure that model results are properly scaled, a mixture spectrum was created with the NEF forward contamination model and three synthetically created parameters values for  $\alpha(\lambda)$ ,  $\beta$ , and  $\frac{n}{a}$  and then run through the inversion process. A properly scaled model will compute estimates for each parameter on the same order (and preferably the same values) as used to create this spectrum. The mixture was made with the pure

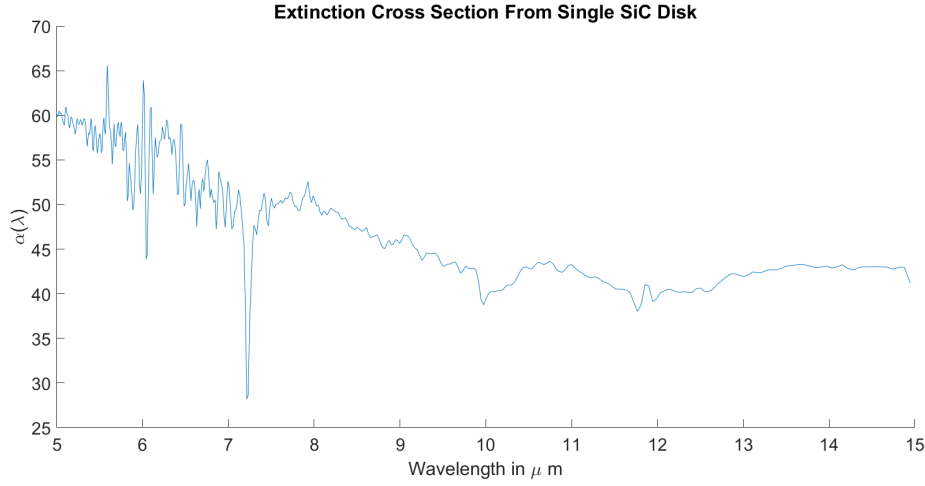


Figure 5.13: Derived extinction cross section parameter found from blackbody transmission measurements of lowest number density compressed disk of silicon carbide powder.

silicon carbide and concrete spectra with parameters for  $\beta$  and  $\frac{n}{A}$  of 4.8 and 0.0052 respectfully. The extinction cross section was created with a uniformly distributed random number generator centered around  $120 \frac{cm^2}{g}$ , which represents a typical magnitude for the parameter.

Since stochastic variability exists in the optimization step of the inversion model, the synthetic mixture spectrum was analyzed 20 times with the inversion model and statistical averages for each parameter were found. After 20 runs, estimates for the coverage density parameter ( $\frac{n}{A}$ ) averaged  $0.0056 \frac{g}{cm^2}$  with a standard deviation of 0.0013. The  $\beta$  parameter estimate is a fitting parameter, but had an average value was 4.2 with a 3.6 standard deviation. If run a larger number of times, the coverage density parameters would likely converge even closer to the actual values assigned during the synthetic mixture creation. Similar results occurred for the extinction cross section with the magnitude only slightly varying from its actual spectrum. These results indicate that the optimization routine incorporated into the inversion model is properly scaled and a viable solution to use.

### 5.4.2 Measured Results

#### Fused Silica

There were several types of materials analyzed on various surfaces, some of which are described in this section. Additional combinations of substrates and contaminants are placed in the appendix. Single examples of three materials (fused silica, red chalk and silicon carbide powders) are considered in this chapter. The first example shown is of fused silica powder obtained from Washington Mills. This material was classified as dust collected fine particles by the company, meaning that all particles within the material were small enough in size that they were not trapped by any sieve mesh available.

The fused silica powder in this example was deposited onto a dry, hardened soil surface in the Nevada desert in varying amounts. This type of situation would normally be problematic due to the inherent complexities of soils as a result of the properties described in Chapters 2 and 3. Despite properties such as particle size distribution, specific material type and crystalline structure being unknowns, this experiment worked because the surface had been so dry. At the time of measurement, the surface had been allowed to dry for a long time resulting in a cement like surface with large deep cracks where particles were not acting independently, but as a surface.

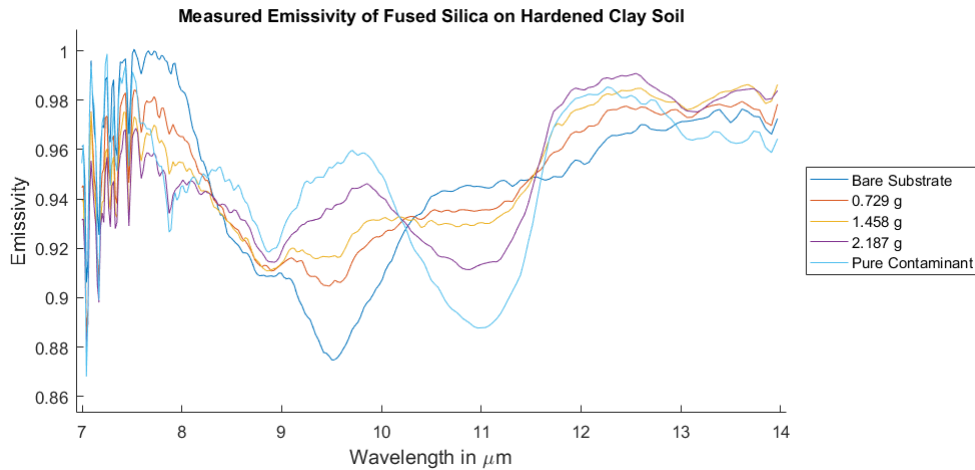


Figure 5.14: Measured emissivity of various amounts of fused silica powder on hardened clay soil in Nevada. Also captured are emissivity measurements of the hardened clay soil without contaminant and an optically thick layer of fused silica.

Figure 5.14 demonstrates a typical data collection of three amounts of material applied to this surface. As material accumulates on the soil surface, the characteristics of the soil become engulfed into the fused silica signature. Confluence points occur around 10.3 and 11.5  $\mu m$  where the emissivity of all combinations of the two materials do not shift regardless of the contamination amount. As evident by the spectral signatures, mixtures that fell between the bare substrate and pure contaminant spectrum existed in the enveloping space between the two signatures. If there existed a point that fell outside of these boundaries, the measurement contained error.

### Red Chalk

The second example material as seen in Figure 5.15 shows the same progression of a red chalk composite powder placed on a portable concrete slab in varying amounts. This chalk comes from Irwin Tools and can be found in hardware stores for making cut lines on large pieces of wood. Since the chalk powder is not of scientific quality, the exact composition is not known. Technical safety data sheets indicate that it contains roughly 75-80 % by volume of calcium carbonate ( $CaCO_3$ ) and 20-25 % by volume of red iron oxide powder ( $Fe_2O_3$ ). While both materials are of powder size, the red iron oxide particles are smaller in a relative sense than the calcium carbonate (see Figure B.2). Larger calcium carbonate particles are coated in the smaller red iron oxide particles as a result of the materials intended application as a line marker.

From a spectral perspective, the sparse applications of this powder on the concrete surface are relatively flat. The major exception to this occurs between 11 and 12  $\mu m$  where a large well defined emission feature occurs and is instantly followed by a significant absorption feature that is best seen in the largest application of the material. This collection was made in September 2017 at the Rochester Institute of Technology.

### Silicon Carbide

The final example material came from Washington Mills and was a silicon carbide powder. This material, like the fused silica, was called dust collected fines meaning it passed through all available sieves at the site. Analysis indicated that particles were all less than 50  $\mu m$  in diameter. Like previous examples, three well defined amounts of material were applied to a concrete surface that demonstrated a progression of features in the



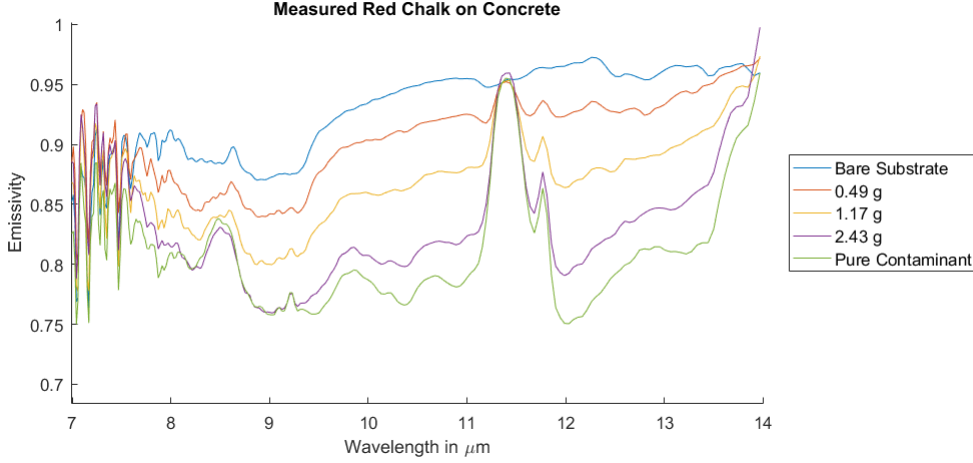


Figure 5.15: Measured emissivity of various amounts of red chalk (Calcium Carbonate and Red Iron Oxide) powder on a concrete surface. Also captured are emissivity measurements of the pristine concrete and an ultra thick layer of red chalk.

mixture. Silicon carbide powder has a relatively high emissivity across the longwave infrared range, but somewhat distinctive features. A very small absorption features exists at  $9 \mu m$  while a drawn out gradual descent in emissivity occurs from  $10$ - $12.5 \mu m$ . This is followed up with precipitous rise in emissivity from  $12.5$ - $14 \mu m$ . This example like the fused silica was collected in the Nevada desert where environmental conditions were optimal.

### 5.4.3 Contrast Ratio

In the process of estimating the three parameters of the NEFDS contamination model, a determination of the contrast ratio must occur. The contrast ratio represents the ratio between the differences of the substrate and mixture to the contaminant. Its calculation occurs within the natural logarithm found in the extinction cross section calculation seen in equation 4.3. Independent of equation 4.3, the contrast ratio can be represented as

$$ContrastRatio = \frac{R_m(\lambda) - R_c(\lambda)}{R_s(\lambda) - R_c(\lambda)} \quad (5.1)$$

Unlike the calculations for the extinction cross section, the contrast ratio should

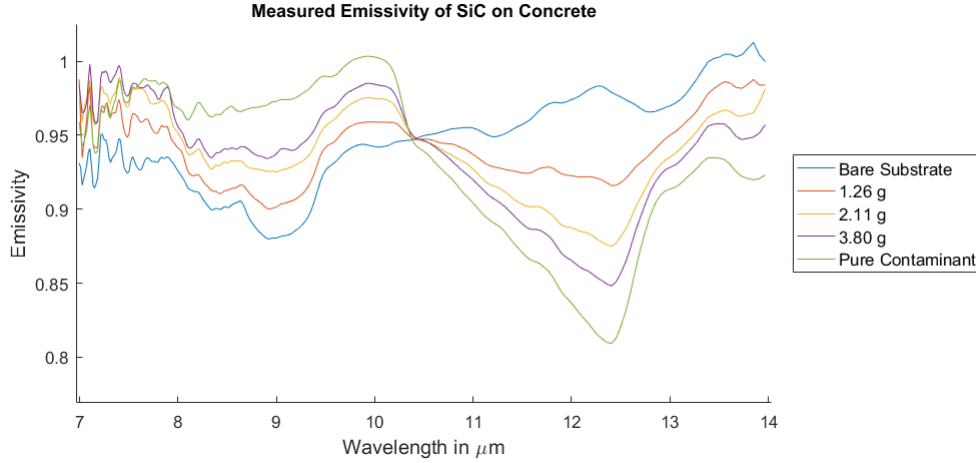


Figure 5.16: Measured emissivity of various amounts of silicon carbide powder on a concrete surface. Also captured are emissivity measurements of the pristine concrete and an ultra thick layer of silicon carbide.

always change with different amounts of contaminant. Recall that the extinction cross section represents the scattering and absorption of the contaminating material and therefore does not vary with differing amounts of material. The contrast ratio described in equation 5.1 has the same denominator for a combination of two materials, but its numerator will change with changes to the mixture spectrum. At small amounts of material, the mixture spectrum should appear more similar to the substrate spectrum, resulting in a contrast ratio closer to one. As more contaminating material is added to the surface, the mixture spectrum approaches the spectral shape of the pure contaminant, resulting in a numerator that approaches zero. So the expectation is that the contrast ratio approaches zero at all wavelengths as more and more material is added to a surface.

### Fused Silica

In the example of fused silica on the hardened soil surface, the contrast ratio at a large majority of wavelengths behaves as expected. Between 8.5 and 9.0  $\mu\text{m}$ , there are overlapping sections of contrast ratio for two contaminant amounts. This occurs because in the measured spectral emissivity data, the variation in signature at these locations is extremely small and measurement error has shifted one mixture slightly above another mixture.

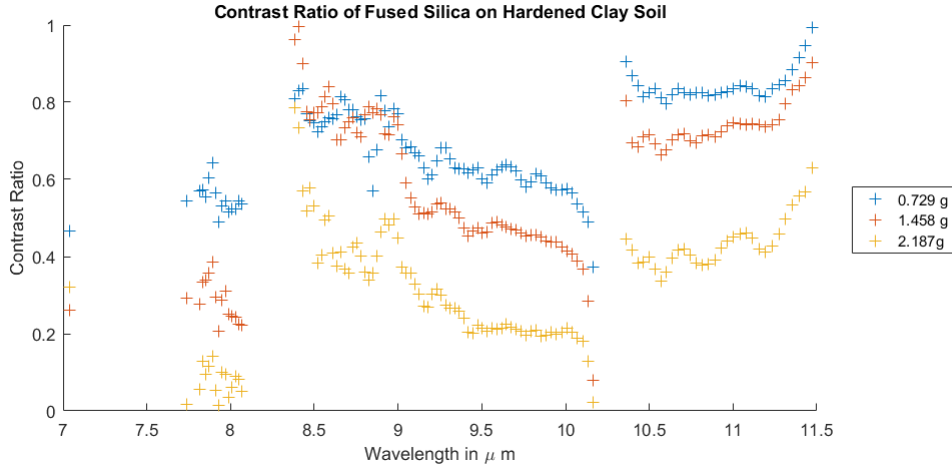


Figure 5.17: Contrast ratio of fused silica powder in three amounts.

### Red Chalk Powder

In the example of red chalk powder, the behavior of the contrast ratio falls more in line with the expected results. Figure 5.18 shows the contrast ratio for the three amounts of contaminant on the surface. As the amount of material increases on the surface, the contrast ratio decreases. Each contrast spectrum appears relatively flat, but decreases clearly at each wavelength. Some points were intentionally not shown in either Figure 5.17 or 5.18. Points at these wavelengths represented locations where one contaminant amount fell outside the boundaries of the pure material reflectances. When this occurs the contrast ratio become negative and the natural logarithm that uses the contrast ratio for calculators has an imaginary component. For simplification purposes, the model eliminated wavelengths where this occurred for the every spectrum in the dataset. The example of fused silica has several locations that were removed for this reason, while the red chalk powder only has this occur in a small section around  $8.5 \mu m$  and two points near  $11.5 \mu m$ . In the latter wavelength location, the error results from small variations between all five emissivity measurements. Given that the magnitude of the five emissivity spectra at this location only change by less than 0.01, even a slight change in the experiments conditions (environmental or otherwise) could shift a mixture spectrum outside normal conditions. In the  $8.5 \mu m$  range, the error is a result of a mixture that was spectrally close enough to the pure contaminant spectrum that similar changes in the experimental conditions could have the same effect as the other section.

As an important note, the inversion model can continue to work even when removing many datapoints for the contrast ratio calculation. Estimates for the contrast ratio and extinction cross section can occur as long as there is at least one wavelength in the mixture spectrum that has validity to complete the calculations. Calculations will be more robust when measurements have more valid datapoints to perform the calculations.

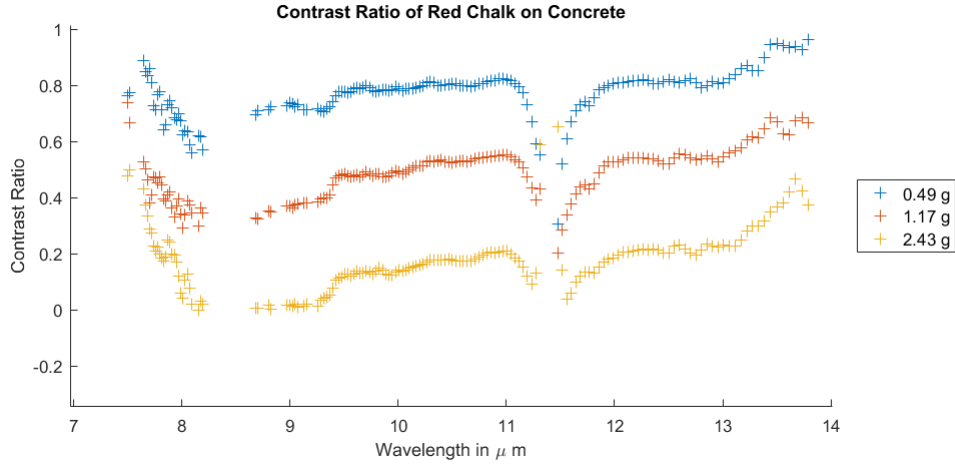


Figure 5.18: Contrast ratio of red chalk powder in three amounts.

### Silicon Carbide

In the final contaminant example, the contrast ratio for silicon carbide is shown in figure 5.19. This example demonstrates the best case scenario as every single wavelength except one at  $10.36 \mu m$  where every single spectra crosses over the same location. Contrast ratios appear mostly flat and decrease as the mixture amount increases. The benefit to having complete and properly trending contrast ratio calculations is that they improve the calculations for the extinction cross section and scalar parameters in future steps to the inversion model. When large spectral regions of the contrast ratio are removed, future calculations are based on smaller sample sizes which leads to increased uncertainty in the validity of the measurements. The silicon carbide example shown has 99.5% of the measured wavelengths which will improve certainty for parameter calculations.

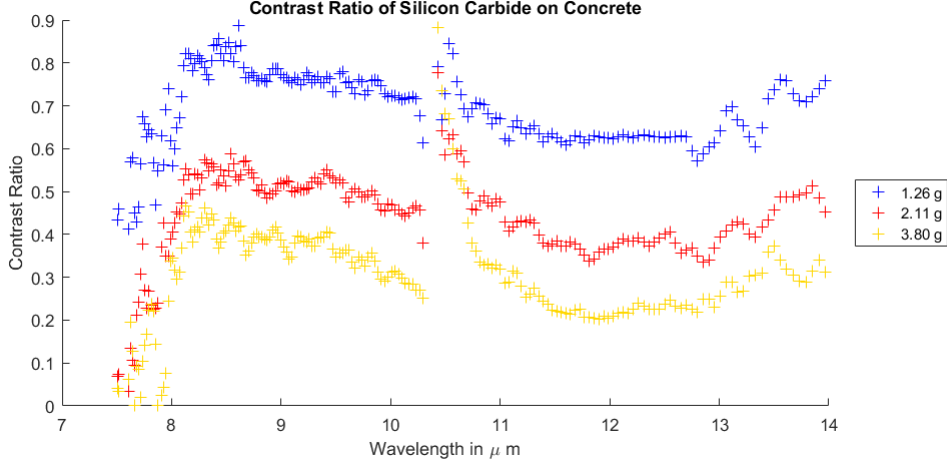


Figure 5.19: Contrast ratio of silicon carbide powder in three amounts.

#### 5.4.4 Estimated Extinction Cross Section

Once the contrast ratios for each mixture were calculated, they could then be input into the direct computation of the extinction cross section parameter. This wavelength dependent parameter was initially calculated as a scalar average across all wavelengths in the first optimization routine. To solve for the extinction cross section, the NEFDS forward model was manipulated algebraically to isolate the extinction parameter as seen in equation 4.3. Contrast ratios were determined for each amount of contaminant and locations where contrast ratios became negative were removed from the calculations.

The mathematically derived extinction cross section represents the scattering and absorption that occurs as a result of the contaminating material only. This means that regardless of the amount of material present on the substrate surface, there should not be variation in the extinction parameter.

#### Fused Silica

The calculated extinction cross sections are shown in figure 5.20. Three amounts of material (0.729, 1.458 and 2.187 grams) were applied to a concrete surface. The calculated extinction cross section for each amount demonstrates reasonable agreement between the three spectra for valid wavelengths. Units for this parameter are square centimeters ( $cm^2$ ), meaning that the numerical representation is an effective area.

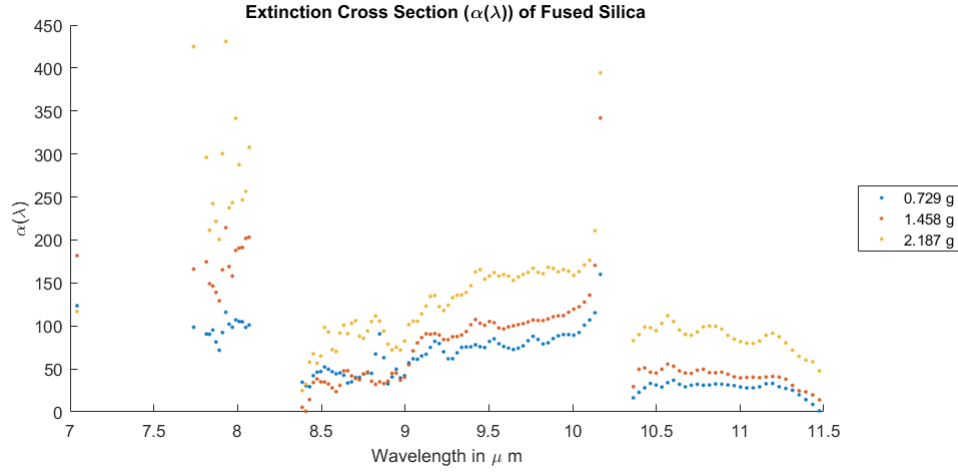


Figure 5.20: Extinction cross section estimates for each contaminant amount of fused silica powder. Due to measurement error, sections of the estimated spectra between beyond 11.5 microns and between 8.0 and 8.25 microns are not considered for final estimates.

### Red Chalk

The second example material, red chalk has extremely good agreement between two of the three contaminant amounts. At almost every wavelength of the spectrum, the 0.49 and 1.17 gram sample calculations are in complete agreement for the calculated extinction cross section. The third spectrum representing the 2.43 gram sample has a significantly larger magnitude than the others, but matches well in terms of spectral shape. As in the previous example, due to measurement error pushing some mixture spectra outside of the enveloping boundaries of the pure material reflectances and negating the contrast ratio term, there are large portions removed from these parameter estimations. These regions were eliminated in this example because the variation from mixture to mixture of the emissivity spectra were so small that even normally negligible error contribution in a sample measurement caused problems. Around  $11.5 \mu m$ , every spectral emissivity measurement falls within 0.01 of the other four samples in the set so this problem was expected. From a radiometric prospective, due to the low differentials between spectral curves create asymptotes in the calculated extinction cross section. While mathematically correct given the inputs, the formation of asymptotes for these locations is likely an artifact of the radiometric model for computation and not apart of

the actual property of the materials.

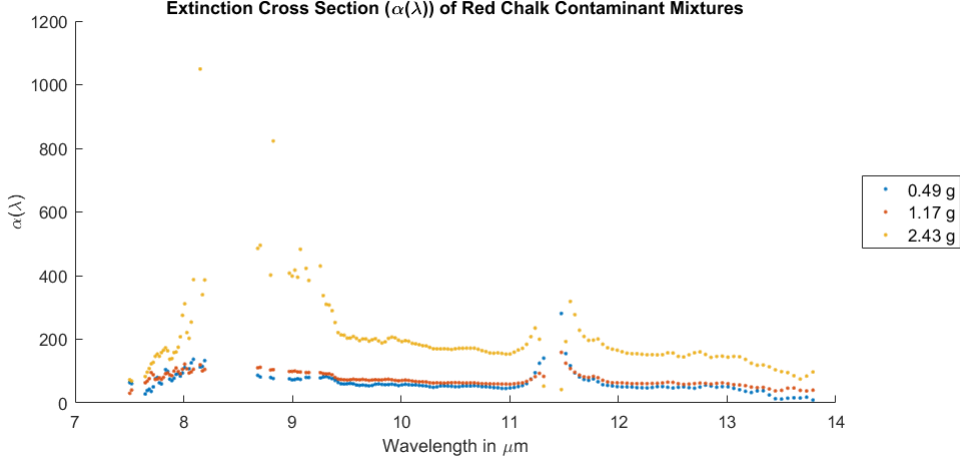


Figure 5.21: Extinction cross section estimates for each contaminant amount of red chalk powder. In ideal cases, limited variation will occur between each measurement. This example has variation in the largest amount of contaminant present, but good agreement between initial two estimates.

### Silicon Carbide

Silicon carbide powder demonstrated the best example of agreement between contaminant amounts as shown in Figure 5.22. This example only had one point eliminated due to a negative contrast ratio at  $10.36 \mu\text{m}$  and found nearly perfect agreement between all three calculated extinction spectra. Each spectrum was flat and had asymptotic trends occurring around  $7.5 \mu\text{m}$  and  $10.4 \mu\text{m}$  where confluence of emissivity spectra occurred. As in the case of red chalk, these locations are likely artifacts of the radiometric model to compute the extinction cross section. This result represents the best case ideal situation as the extinction cross sections are in agreement and almost every point is available for further calculations.

#### 5.4.5 Comparisons Across Measurement Sets

As a verification that the model was performing the estimation of the extinction cross section correctly and consistently, overlays of calculated cross sections for multiple data collections are compared. Despite the environmental conditions and the amounts of

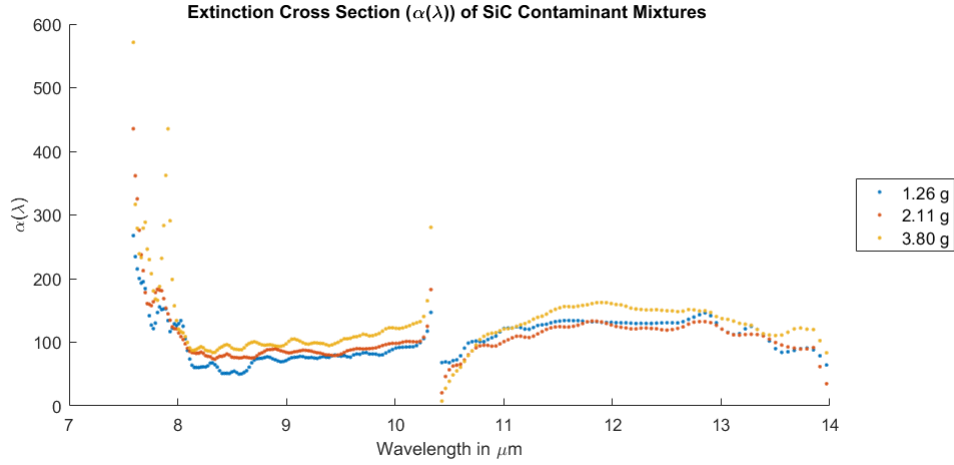


Figure 5.22: Extinction cross section estimates for each contaminant amount of silicon carbide powder. In ideal cases such as this, limited variation will occur between each measurement.

contaminant applied for each collection being slightly different, the properties of the parameter imply that there should be agreement regardless. This was done in lieu of a database comparison as there is seemingly no spectral library of extinction for longwave infrared materials publicly available. Comparing multiple collections helps to ensure that the estimates are not randomized based on a single collection.

### Red Chalk

In Figure 5.23, a comparison of the estimated extinction cross section parameter from three sets of collections taken on three separate occasions is shown. Each collection is labeled with  $D\#$  to indicate which collection the spectrum belongs to and each are followed by a letter, indicating the contaminant amount order in each collection. So spectrum  $D2a$  is from collection two and represents the estimated extinction cross section from the smallest amount of material in that set. Two collections had contaminant mass available and the third was collected before a methodology for empirically measuring mass was developed. With the exception of two outliers, the estimates for these three data collections appear in good agreement across the entire longwave infrared, indicating agreement in the model for this specific material, not just a single data collection.



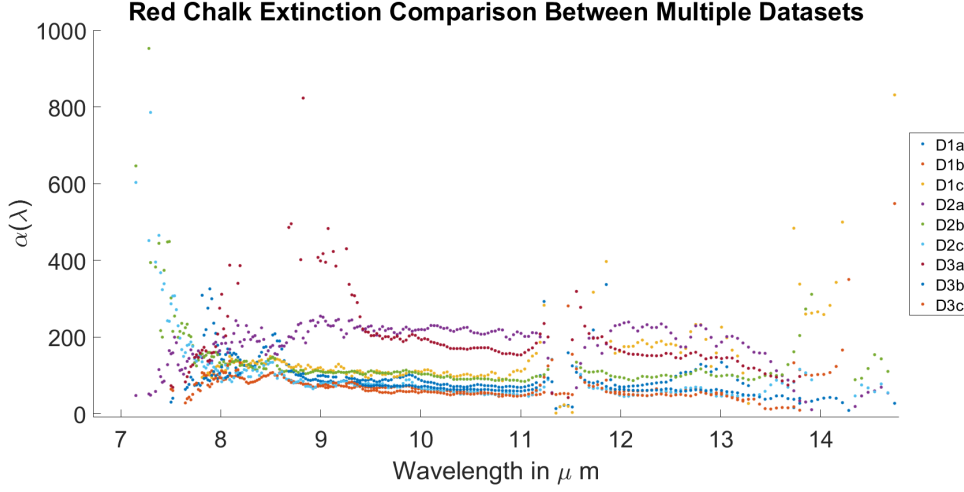


Figure 5.23: Extinction cross section estimates for each contaminant amount of red chalk powder. In ideal cases, limited variation will occur between each measurement. This example has variation in the largest amount of contaminant present, but good agreement between initial two estimates.

### Silicon Carbide

In Figure 5.24, the same comparison was performed for the silicon carbide powder. This figure overlays four data collections taken in multiple states over two years. Collections with measured contaminant mass data are included with collections that do not have mass data. While the example collection from the previous section contained all but a single datapoint for each of its cross section calculations, some collection sets presented here were missing up to 40% of the wavelength range due to collection error leading to a negative contrast ratio. This comparison only intends to demonstrate the agreement that occurs between data collections for a given material. Like the red chalk example, the silicon carbide powder demonstrates reasonable agreement between all collected results. This demonstrates that the fidelity of the algorithmic process to estimate the extinction cross section parameter for a given material regardless of contaminant amount or environmental variation that may occur on a given collection day.

#### 5.4.6 Scalar Parameter Estimates and Mixture Reconstruction

Estimates for the scalar parameters  $(\beta, \frac{n}{A})$  are determined using the look-up table method from the third step of the parameter inversion model (see Chapter 4. These

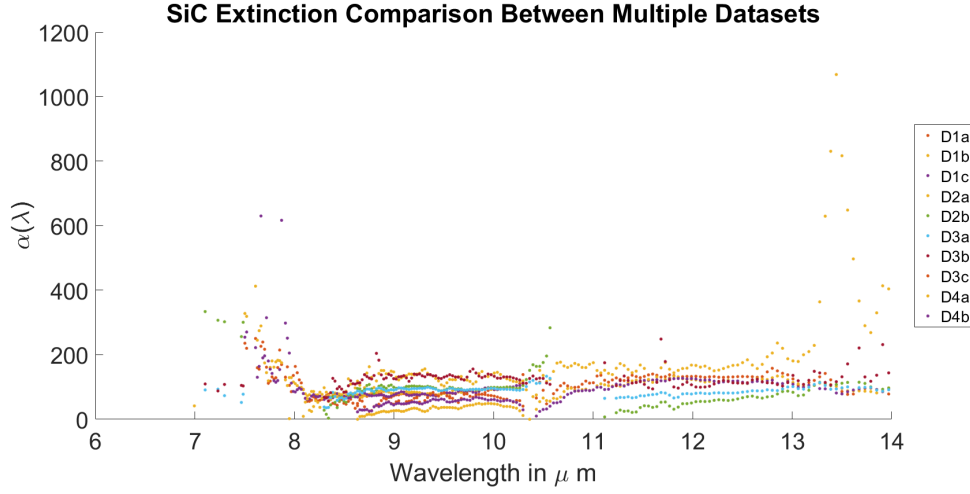


Figure 5.24: Extinction cross section estimates for each contaminant amount of silicon carbide powder. In ideal cases such as this, limited variation will occur between each measurement.

parameters represent properties of the contaminant particle stacking as well as the area coverage density of the contaminant respectively. The look-up table used the direct extinction calculations described in the second step of the inversion model alongside the pure material reflectance spectra. Every possible combination of the two scalar parameters was determined and input into the forward model to create mixtures that were then compared to the empirically measured spectrum. The combination of scalar parameters that yielded the lowest sum squared difference between the empirical results and the calculated results represented the best fitting combination of parameters. As a visual check, the parameters were then used in the forward model to overlay the resulting mixtures with their measured counterparts.

### Fused Silica

Fused silica was applied in three amounts (0.729, 1.458, and 2.187g) on a hardened soil surface. Once passed through the parameter inversion model, the scalar estimates for the particle stacking parameter ( $\beta$ ) indicated that the material had some stacking occurring between particles. Values for this parameter were relatively low compared to the given boundary conditions, having values of 3.481, 2.221 and 5.841  $\frac{cm^2}{g}$ . Given that the forward model used this parameter as a fitting parameter, the boundary conditions

within the forward model were not clear, therefore they were set between zero and ten units. Since the surfaces examined have a sparse nature, it is possible that the upper condition on  $\beta$  could be increased orders of magnitude. The effect of this parameter is relatively small compared to the other parameters because of its location within the model, so changing its upper boundary should not have a significant effect regardless.

Estimates for the area coverage density parameter demonstrate consistency with the observable conditions of the experiment. When material was added to the surface, the estimated coverage density parameter increased as expected (0.005, 0.006 and 0.0093  $\frac{g}{cm^2}$ ). Each of these scalar parameters can be seen in Table 5.2. When combined with the estimated extinction cross section parameter, the modeled emissivity spectra for each mixture show near perfect agreement with the measured spectra. Figure 5.25 shows how each modeled spectra using the parameter estimates and measured spectra compare. While a section of the spectrum from 12-14  $\mu m$  was eliminated in estimating the extinction, the modeled and measured spectra are in good agreement for wavelengths that were considered.

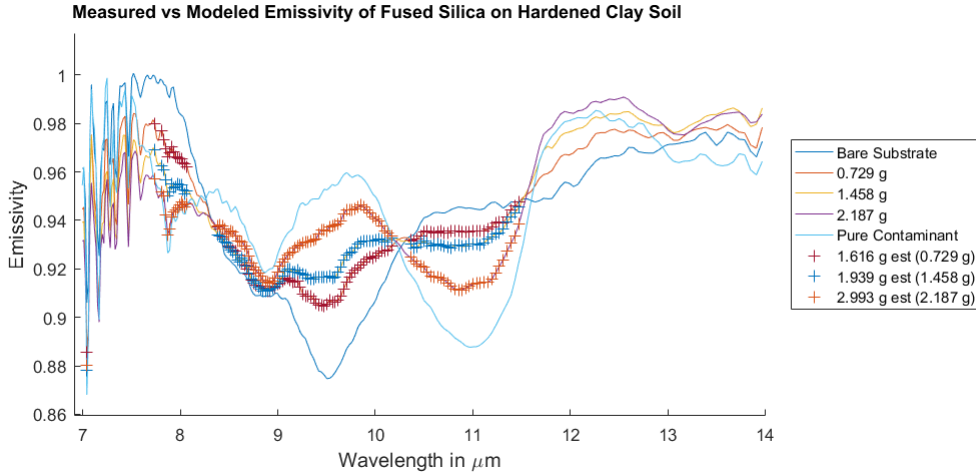


Figure 5.25: Measured and modeled comparison for fused silica powder on hardened clay coil.

### Red Chalk

In the second example material, a red chalk powder was applied to a concrete surface in three amounts (0.49, 1.17 and 2.43  $\frac{g}{cm^2}$ ). Like the previous example, the estimates

for the particle stacking properties appear relatively low, indicating that the contaminating material was more concentrated and stacking occurred. Again the contaminant area density parameter increases with each increasing amount of contaminant (0.0044, 0.00069 and  $0.0080 \frac{g}{cm^2}$ ).

In the fused silica example, the reconstructed mixture spectra were good matches with the measured emissivity mixtures, however there were large portions of the spectra missing as a result of the error that occurs due from the extinction estimation step. The data for red chalk powder does not have significant sections of the spectra missing except for a small section around  $8.5 \mu m$ , so the modeled outputs were more complete compared to the fused silica. Still, when passing the parameter estimates through the forward model, the mixture results are near perfect matches to the measured dataset.

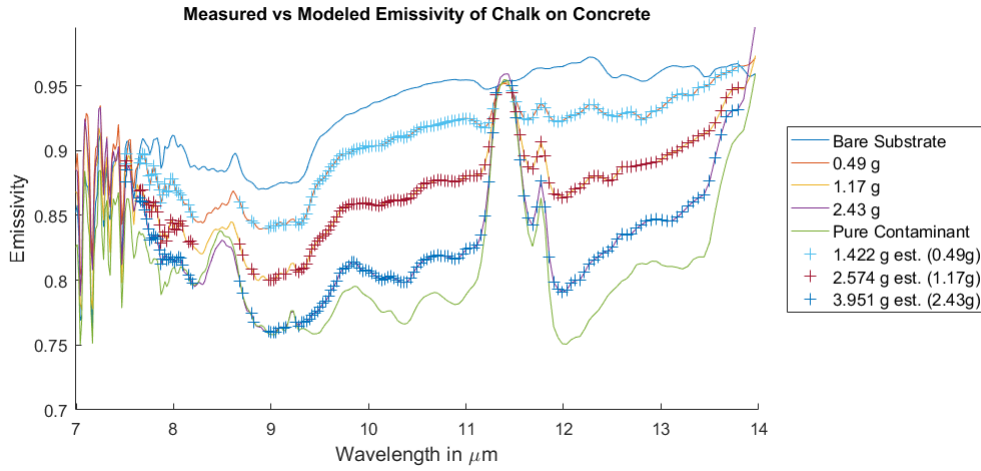


Figure 5.26: Measured and modeled comparison for red chalk on concrete.

### Silicon Carbide

In the case of silicon carbide powder, there are again similar trends in the estimated parameters. Silicon carbide was placed in amounts from 1.27-3.80 grams onto a concrete slab. The stacking properties parameter appears relatively high within the set boundary conditions with values of 8.364, 8.714 and  $6.825 \frac{cm^2}{g}$ . This demonstrates that the contaminant is more evenly spread across the surface than the previous examples. An even spread helps to create a more consistent mixture across the area. With regards to

the coverage density parameter, once again the estimated density of material increases ( $0.0035$ ,  $0.0080$ , and  $.0122 \frac{g}{cm^2}$ ) as material is added to the surface.

Reconstructed mixture spectra as seen in Figure 5.27 show that almost all wavelengths were present in reconstruction and that they modeled parameters result in excellent matches to the measured spectra. There is explicit consistency for all materials in the estimation of parameter and well fit reconstruction of mixture signatures.

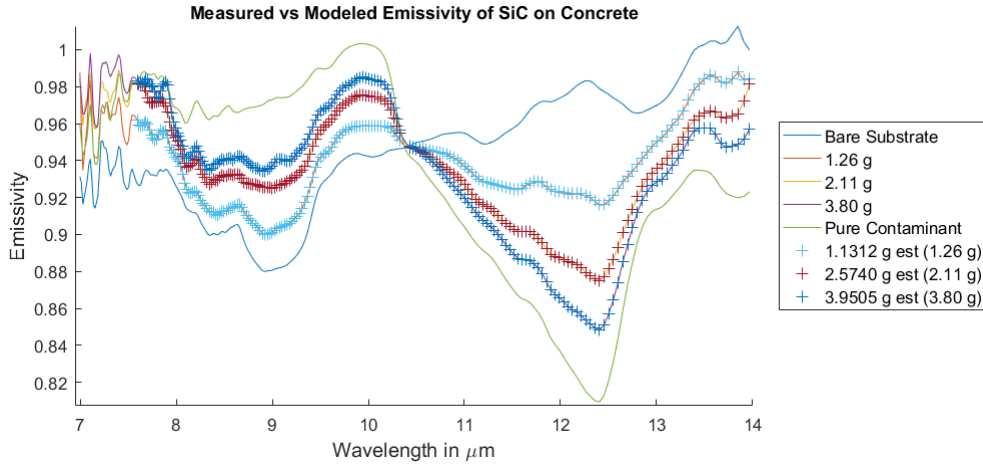


Figure 5.27: Measured and modeled comparison for silicon carbide powder on concrete.

#### 5.4.7 Derived Total Mass

Once all parameters from the parameter inversion model have been estimated, the total contaminant mass present can be derived. This calculation makes the assumption that the coverage density present in the sensor IFOV is consistent with the coverage density present in the area where mass was applied. The D&P FTIR instrument is non-imaging and therefore only takes in information from a single pixel. This pixel projects a roughly three inch in diameter spot size onto the surface when the instrument sits on a standard sized tripod. Due to limitations in the availability of small sized sieves, the contaminant deposition process relied on the application of material with a sieve that was ten inches in diameter.

Using equation 4.4, the total amount of material was determined for each mixture. Results for all three example cases are presented in Table 5.2. In the case of fused silica,

overestimation occurred for all three mixture amounts, but each derived mass fell within 0.9 grams of material of the actual amount applied. Error in this sample may have been a result of uneven application as this example had very low  $\beta$  estimations. Furthermore, there were clear disadvantages in the estimation of the extinction cross section (lack of points, slight inconsistencies between spectra) that could have caused issues in the estimation of the total contaminant mass. Red chalk powder also saw overestimation of the total mass occur. Like the fused silica, the distribution of particles as denoted by the  $\beta$  values likely contributed to the error.

Unlike the previous two examples however, silicon carbide mass estimations were on point, being within 22% of the actual amount applied in all cases and less than 10% in two of the three. This set had high estimations for the  $\beta$  parameter, indicating good spread of particles. It is clear that if there is uneven or poor particle distribution of the sample on the surface, the total estimations of material will be error prone as they are based on densities of the sensor IFOV. In a theoretical sensor with an array of pixels, all area will be covered and each pixel will have a unique coverage density associated with it. In that situation, this problem should not exist as every contaminated area will have a measurement associated with it. Figure 5.28 demonstrates the error between each derived total mass value to the actual amount applied with a 1:1 line present for reference.

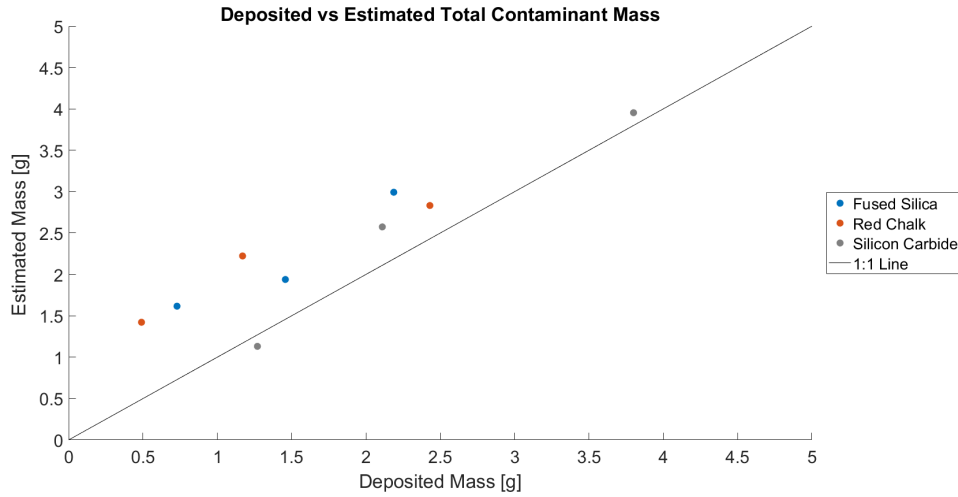


Figure 5.28: Deposited versus Estimated total mass for each contaminant.

Table 5.1: Best fit line statistics for each dataset of Applied vs Estimated contaminant total mass.

Fused Silica on Hard Soil			
Material	Slope [m]	Intercept	$R^2$
Fused Silica	0.944	0.806	0.9141
Red Chalk	0.697	1.209	0.9393
Silicon Carbide	1.073	-0.015	0.9587

Statistical best fit lines were calculated to determine if any inherent bias existed, if there was a trend to the data fits and how well they produced a matching plot with the data. The results of this analysis are presented in table 5.1. Ideal fits for this sequence have a slope of exactly one with a zero y-intercept which would represent perfect mass derivation for all cases. Red chalk powder represented a failure to achieve either statistic having a slope of 0.697 and an intercept above 1.2. These characteristics indicate that for this particular material, the model improved as more material was added to the surface as a slope below one will eventually converge with the 1:1 line. This fit matched with the projected line reasonably well, having an  $R^2$  value of 0.9393.

Fused silica has an adequate slope (0.944) on its fit line, but contains a large bias (0.806) factor. Without a bias of this size, the best fit line would nearly overlap the desired 1:1 fit line. Having a bias is not necessarily a bad thing as this example represents a fit with a near 1.0 slope, indicating that the bias for this material is similar across the range, but still robust in its calculation of total mass amounts. Statistically, the  $R^2$  value for this material is the lowest of the three examples, but still remains at 0.914 meaning the data can be 91% explained using the slope and intercept parameters.

The most ideal case presented is of silicon carbide powder. This example fit a line with a slope of 1.073 and an intercept of just -0.015, which almost perfectly matches with the 1:1 trendline desired. For this example, the  $R^2$  value is just .9587, but most of the unexplainable phenomenology originates in the second datapoint where the estimated mass is slightly too large. Each of the three examples presented a different type of result indicating that while the method is robust, improvements can still be made to ensure more accurate results.

Table 5.2: Estimated NEFDS contamination model scalar parameters and total mass for fused silica, red chalk and silicon carbide powder examples. Total mass is based on surface area of 10 inch diameter sieve.

Fused Silica on Hard Soil				
Mass Applied [g]	$\beta$ -value [ $\frac{cm^2}{g}$ ]	$\frac{n}{A}$ [ $\frac{g}{cm^2}$ ]	Estimated Mass [g]	$\Delta$ Mass Es- timated
0.729	3.481	0.0050	1.616	0.887
1.458	2.221	0.0060	1.939	0.481
2.187	5.841	0.0093	2.993	0.806
Red Chalk on Concrete				
Mass Applied [g]	$\beta$ -value [ $\frac{cm^2}{g}$ ]	$\frac{n}{A}$ [ $\frac{g}{cm^2}$ ]	Estimated Mass [g]	$\Delta$ Mass Es- timated
0.49	3.2732	0.0044	1.422	0.932
1.17	4.5787	0.0069	2.223	1.053
2.43	4.0131	0.0080	2.833	0.403
Silicon Carbide on Concrete				
Mass Applied [g]	$\beta$ -value [ $\frac{cm^2}{g}$ ]	$\frac{n}{A}$ [ $\frac{g}{cm^2}$ ]	Estimated Mass [g]	$\Delta$ Mass Es- timated
1.27	8.364	0.0035	1.131	-0.139
2.11	8.714	0.0080	2.574	0.464
3.80	6.825	0.0122	3.951	0.151

#### 5.4.8 Statistical Analysis

Each of the inversion model runs finds the optimal parameter set to reconstruct the mixture spectrum using the radiometric model behind the NEFDS contamination model. The results of the inversion model can however, vary from run to run in the event that the model finds localized error, the existence of multiple local minima or otherwise. Steps were put into place in the model itself to help reduce this, including the incorporation of a multiple start program, which performed each estimation using a user defined set of randomized starting locations on the spectrum. As an additional statistical support, the model operated 1000 times on the same dataset to achieve statistical metrics of performance and variability. A set of example statistics is shown in this section on the silicon carbide dataset. Each estimated scalar parameter alongside the derived total contaminant mass has statistics of mean, standard deviation, variance and standard error.

Table 5.3: Statistical analysis for parameter estimates of silicon carbide on concrete dataset.



$\beta$ Estimate Statistics for Silicon Carbide on Concrete				
Mixture	Mean [ $\mu$ ]	Standard Deviation [ $\sigma$ ]	Variance [ $\sigma^2$ ]	Standard Error
0.729 [g]	5.066	4.352	18.936	0.1376
1.458 [g]	4.960	2.862	8.188	0.0905
2.187 [g]	5.360	2.865	8.209	0.0905
Coverage Density Statistics for Silicon Carbide on Concrete				
Mixture	Mean [ $\mu$ ]	Standard Deviation [ $\sigma$ ]	Variance [ $\sigma^2$ ]	Standard Error
0.49 [g]	0.0033	0.0003	$1.1 \cdot 10^{-6}$	$9.49 \cdot 10^{-6}$
1.17 [g]	0.0074	0.0007	$5.3 \cdot 10^{-6}$	$2.21 \cdot 10^{-5}$
2.43 [g]	0.0110	0.0011	$1.15 \cdot 10^{-5}$	$3.48 \cdot 10^{-5}$
Grams Present Statistics for Silicon Carbide on Concrete				
Mixture	Mean [ $\mu$ ]	Standard Deviation [ $\sigma$ ]	Variance [ $\sigma^2$ ]	Standard Error
1.27 [g]	1.066	0.106	0.011	0.0034
2.11 [g]	2.398	0.235	0.055	0.0074
3.80 [g]	3.565	0.347	0.120	0.0110

The results for the  $\beta$  parameter show that the model does not have a well defined physical representation for this parameter. The mean results for  $\beta$  hover around the midway point of its defined boundary conditions, while the standard deviation of each of the mixture amounts show that almost the entire bounded range for the parameter falls within the first standard deviation from the mean. Since the parameter is utilized as a fitting parameter in the forward model, the statistical results seem to confirm its lack of physical meaning and insensitivity to the final results. Other materials showed similar statistics for this parameter. A visual representation of this parameter is seen in Figure 5.29 which shows the 1000 estimated  $\beta$  results for the 2.11g mixture binned into 10 groupings. From this figure, it is clear that there is not a normal distribution, but an equal likelihood of any result within the boundaries occurring for this mixture. This is the expected behavior of a parameter that is only applied as a fitting term in a model.

The mean results for the coverage density and grams present terms of the three mixtures are significantly more interesting. They show that the model does converge towards the actual amounts applied to the surface. Each coverage density had means centered at similar points to the single run results from Table 5.2, but also had very small standard deviations and variance results. Histogram results indicate that the coverage

density and derived total mass terms both follow normal distributions with elongated leftward tails.

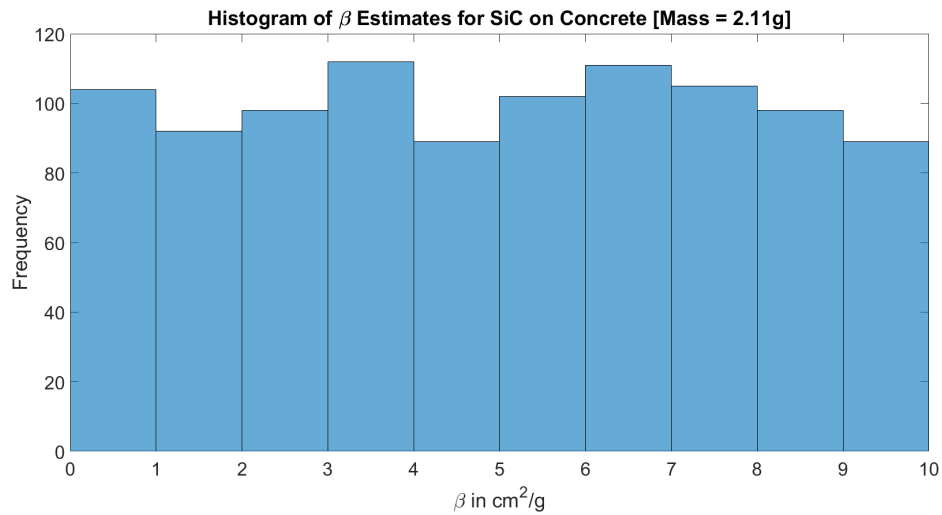


Figure 5.29: Histogram chart of the estimated results for the 2.11g application of silicon carbide on concrete for the  $\beta$  parameter.

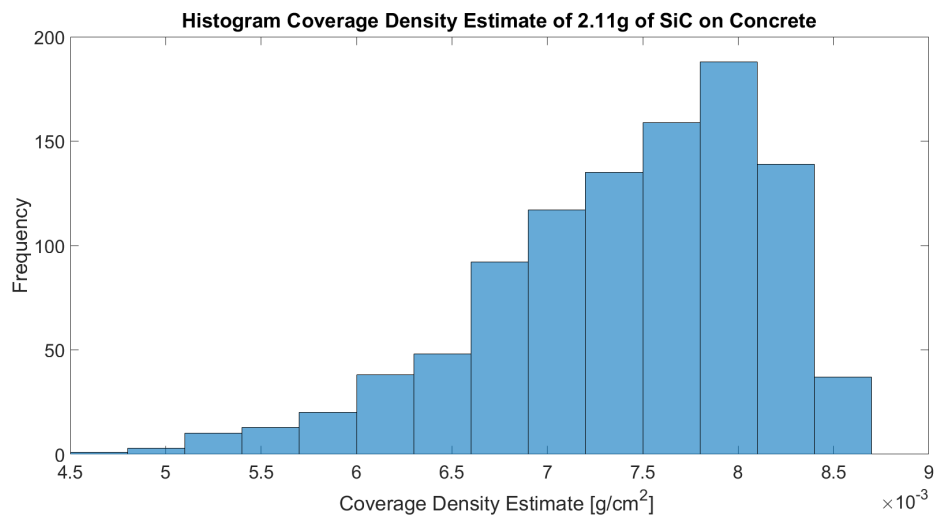


Figure 5.30: Histogram chart of the estimated results for the 2.11g application of silicon carbide on concrete for the  $\frac{n}{a}$  parameter.

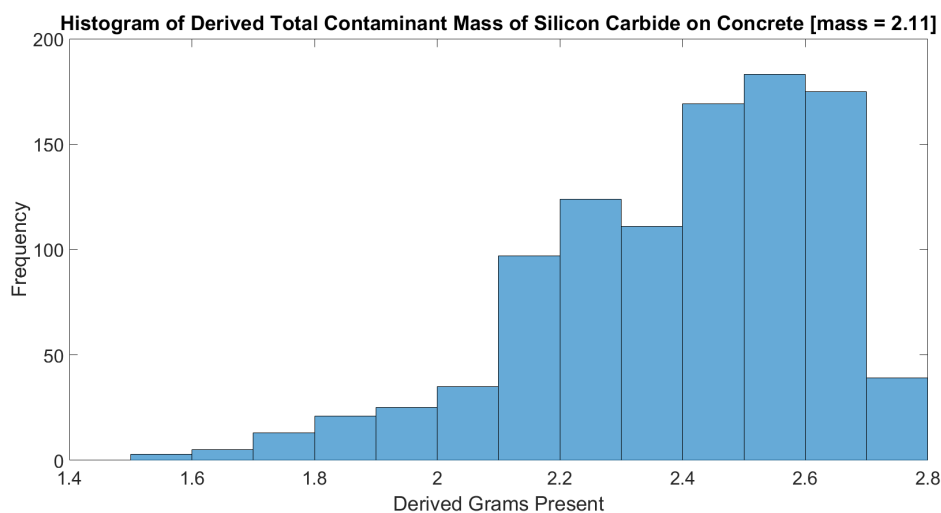


Figure 5.31: Histogram chart of the estimated results for the 2.11g application of silicon carbide on concrete for the derived total contaminant mass.

### Error Propagation

In addition to the statistics provided above, a brief study of error propagation was performed on silicon carbide data to examine how shifting the temperature of the mixture signatures changed the parameter inversion model's ability to derive total contaminant mass. In order to do this, instrument measurements for all mixture spectra from the silicon on concrete data collection were adjusted by one, two and five degrees Kelvin and reprocessed for spectral emissivity. Pure material substrate signatures were left alone so that the spectral shift in emissivity only occurred in the mixture spectra. The new mixture spectra were then re-run through the inversion process and an output for total contaminant mass was derived.

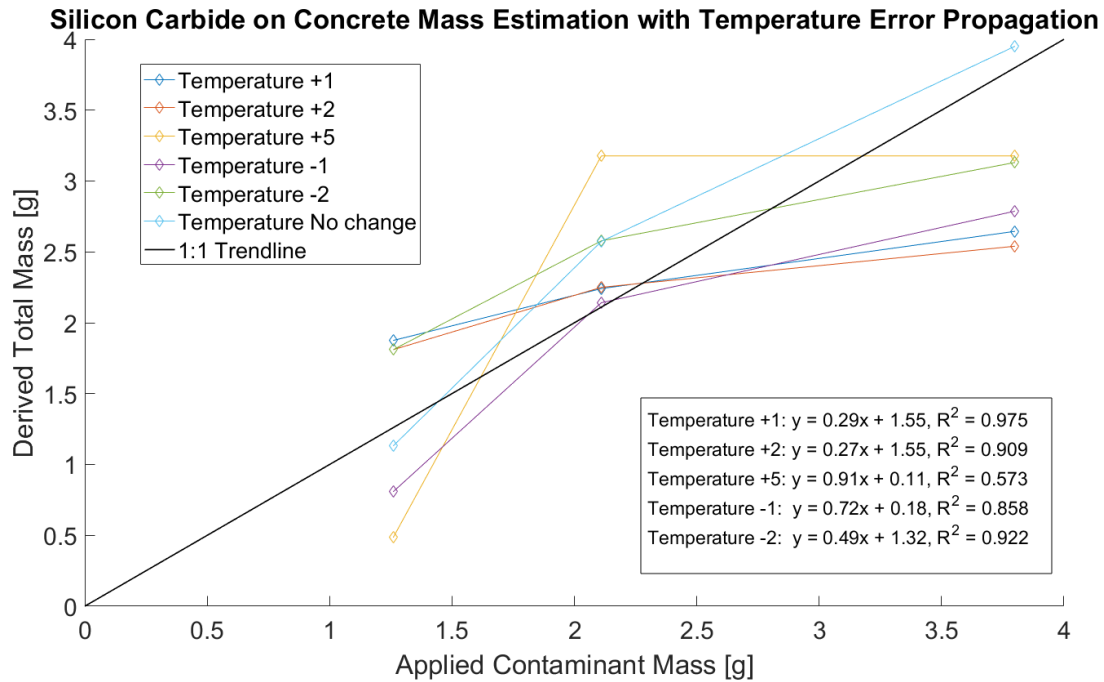


Figure 5.32: Derived total contaminant mass [g] for three contaminant amounts with varying temperature changes.

The estimated total contaminant mass amounts were plotted against the amounts applied in Figure 5.32 for five temperature changes. Because the magnitude of emissivity shifts as temperature is adjusted, mixtures with a negative five degree deviation fell outside of normal parameters for emissivity and were not considered in this examination. Included in the figure are linear best fit lines and r-squared values for each set of mass estimates. There appears not to be a specific trend associated with a change in temperature for the derived total contaminant mass. Fitted slopes for all five instances fell well below one, and intercepts were varied between each example. This study may show more clearly defined trends in this data with an example containing more than three contaminant amounts for analysis.

## 5.5 Signature Injections

Parameter inversion model results were used to create synthetic target signatures in hyperspectral data from the Blue Heron sensor (described in Chapter 4). The data was

created with the parameter estimates from the model, the pure contaminant spectrum, and the selected pixel emissivity spectrum from the airborne scene as the substrate. Mixtures were made using the NEFDS forward contamination model and placed back in the scene in the original locations of the substrate asphalt signatures. Each target block contained a 3x3 section of pixels with a different combination of conditions. Every row represented a different coverage density estimate from the parameter inversion model and each column of target blocks representing a different sub-pixel fraction coverage resulting in 27 unique combinations of the conditions with nine pixels for each combination. Pixel fraction coverage varied by target scene, but typically occurred in 10% drops from full pixel down to 20% coverage.

The main scene used for the signature injections came from the Blue Heron sensor collection over building 101 of the Harris Corporation in Rochester New York in November 3<sup>rd</sup> and 4<sup>th</sup> of 2015 [36]. The weather on these days showed clear skies with unseasonably warm air temperatures. The scene occurred over a mostly empty parking lot and next to a very shallow water retention pond. The example scene described in the following sections will be of a collection that occurred on November 4<sup>th</sup> at 18:07:02 UTC time (1:07 pm est).

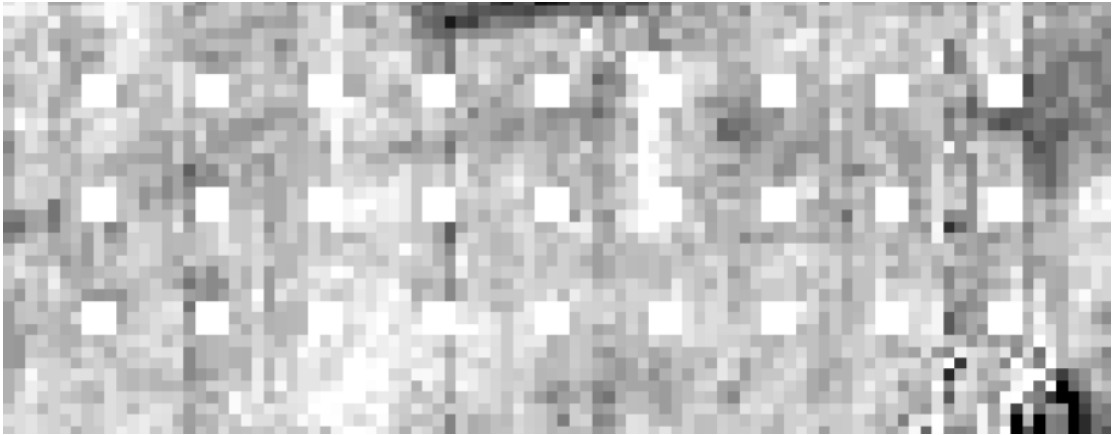


Figure 5.33: Blue Heron airborne sensor data with synthetic target signatures injected onto asphalt parking lot surface. This image was created without consideration to the effects of the point spread function created by the limitations in the optics of the Blue Heron sensor. Spectral plots show emissivity products of each pixel in a target block (9 total).

### 5.5.1 PSF vs. No PSF

The initial placement of synthetic targets in the scene was performed without consideration for the degradation of signal due to the optics in the system. This caused pixels within each target block to appear uniform and stand out relative to background pixels which is not realistic or ideal for this study. Since the point spread function blurs targets and was not initially available or obtainable from objects in the scene, the synthetic targets were first added without a blurring effect. An example of how the targets appeared can be seen in Figure 5.33 where all 27 3x3 blocks of targets appear essentially the same visually in this image chip.

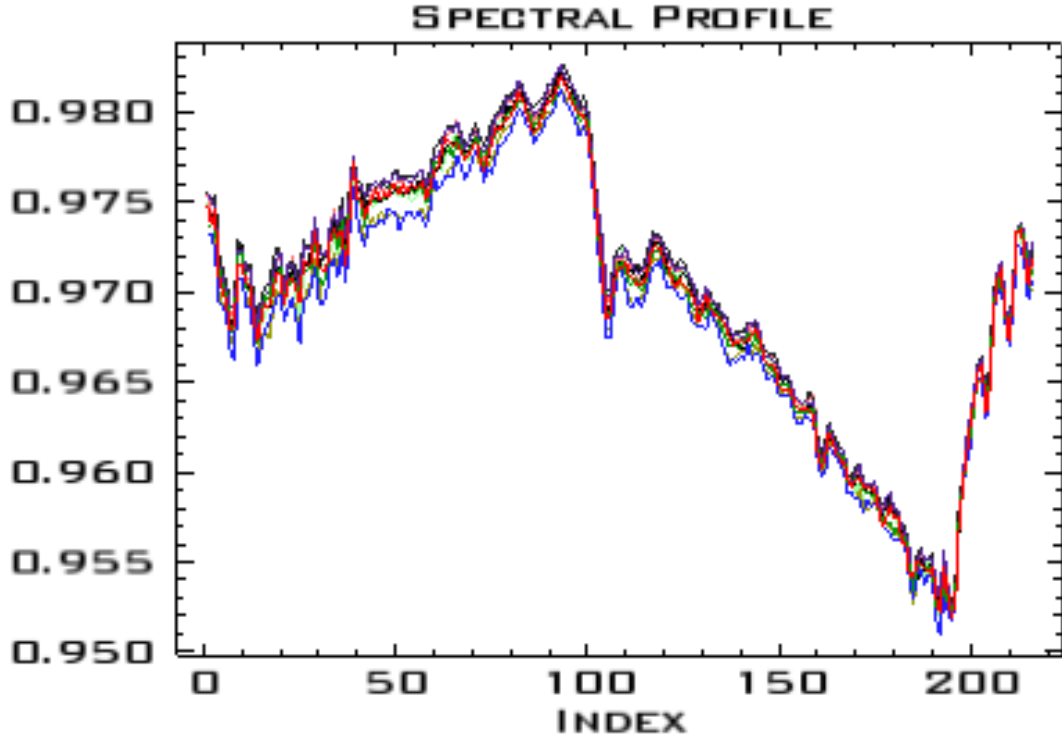


Figure 5.34: Spectral profiles of the nine target signatures from the center target block found in the middle row and fifth column of the target block grid. Targets in this block were created with the middle mixture parameters estimated from the parameter inversion model and contain target signatures in just 50% of each pixel. Little to no variability exists between the spectra due to the effects of the point spread function not being included in the target signatures.

An example of how a failure to incorporate signal degradation due to optics can be seen when examining the middle target block (middle row, 5th block from either direction). This block is a 50% sub-pixel fraction target block with the second largest amount of contaminant present from the measured data. Each pixel is created by incorporating the estimated parameter values with the measured pure contaminant spectrum and asphalt emissivity from the airborne data. When targets are created without the effects of a point spread function, the signals from the 3x3 block only differ by the variation found between the asphalt substrate. Every other parameter included in the creation of the emissivity spectrum is exactly the same for these nine pixels. The lack of variation can be viewed in Figure 5.34 where the spectral profile for all nine pixels are overlayed in a spectral plot. Clearly the variation between the nine signatures is extremely limited.

It is understood that when applying a blur kernel or point spread function to a pixel, the pixel will contain contributions from all surrounding pixels and depending on PSF size, secondary neighboring pixels. In this situation, if a PSF was 5x5, an edge pixel on the 3x3 target blocks stronger contributions from background pixels than would the center target. Edge targets would have an even stronger influence by the background as the mismatch between PSF center and target block center would be less aligned.

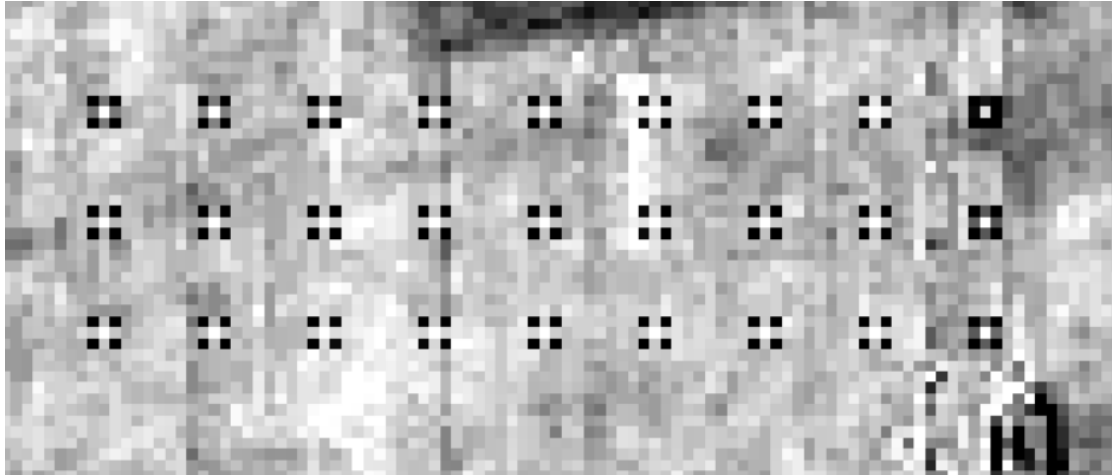


Figure 5.35: Target signatures from pixels contained in the center target block (5th column, middle row) for silicon carbide. These target signatures contain the effects of the point spread function unlike the previous example. Variability exists between the middle pixel, edge pixels and corner pixels that would normally have been seen in real imagery.

The PSF was determined from a line spread function created by a narrow aluminum foil line in a separate collection with the sensor that occurred in November of 2017. The line spread function was used to create a 3-dimensional point spread function that was used exclusively on the synthetic target data. The PSF was 5x5 pixels, however target blocks were separated by enough pixels not to self-contribute to other synthetic targets. Following the application of the point spread function to the synthetic targets, a check on the variability of the emissivity signatures was done. Using the same visualization settings, an image chip of the targets degraded by the PSF can be seen in Figure 5.35. Clearly the effects of the PSF were stronger on the edges and corners than on the center pixels, where an effect still occurred but more contribution from target signatures occurred. Looking at the spectral responses of the pixels in the middle target block discussed earlier, clear variability can be seen. Three groupings occur as seen in Figure 5.36, two grouping of four spectra and a single spectrum appearing alone as the highest magnitude spectrum.

These target representations indicate the importance of including the effects of sensor optics to synthetic targets placed in airborne imagery. Without the addition of these effects, the target spectra will appear essentially uniform and have no relevance to the study of target detection performance sensitivity to the variables considered.

## 5.6 Target Detection

The goal of this experiment is to determine if better matching with a mixture spectrum to a test pixel will improve detection performance over simply using a pure contaminant spectrum. By creating a grid of mixture targets with varying target signatures, analysis can be performed to achieve this goal. Following the convolution of the point spread function to synthetic target spectra created with the estimates from the parameter inversion model, the scenes were ready for target detection analysis. Airborne data was from a parking lot was used for synthetic target injection and a full scene example of data with targets can be found in Figure 5.37. A sparsely filled asphalt parking lot makes up about 40-50% of the scene while grass and a nearly empty retention pond comprise the rest of the scene. The large black area in the parking lot appears to be a location that was sealed with different sealant than the rest of the lot or painted with a paint. Targets varied in coverage density by row (increasing density moving downward)



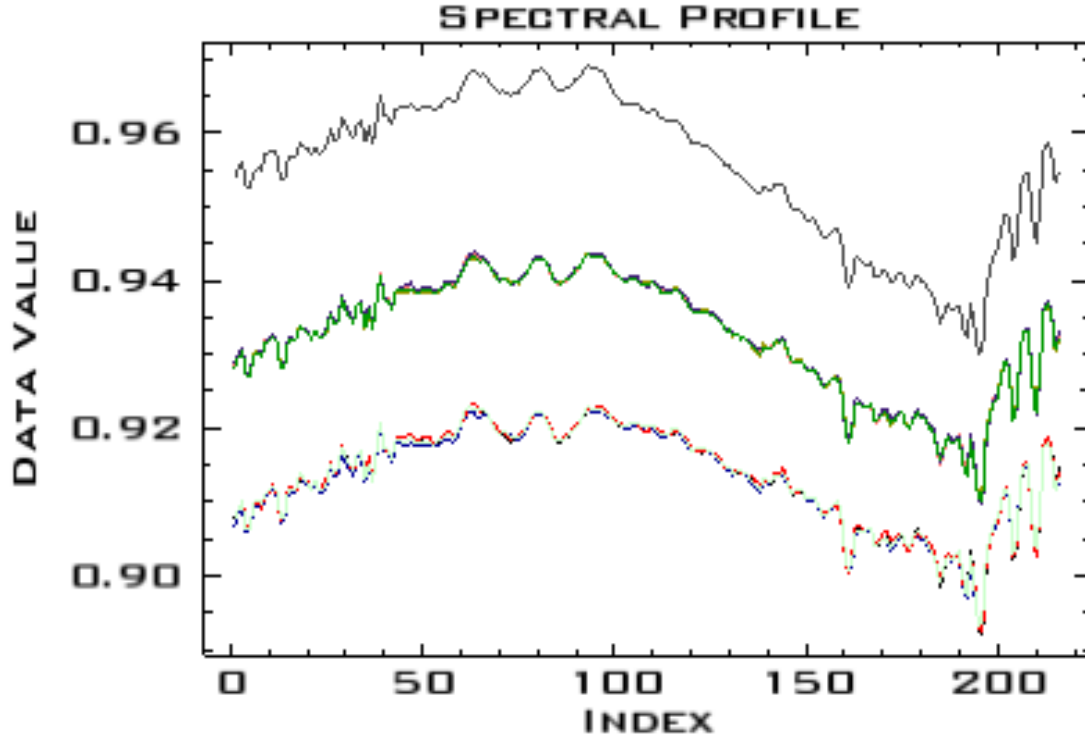


Figure 5.36: Blue Heron airborne sensor data with synthetic target signatures injected onto asphalt parking lot surface. This image was created with consideration to the effects of the point spread function created by the limitations in the optics of the Blue Heron sensor. Clear variation occurs between center, edge and corner pixels from a visual and spectral standpoint.

and sub-pixel coverage in columns (full pixel on right-most column to 20% sub-pixel coverage on far left).

Target signatures were created using the same estimated parameters from the inversion model along with a spectral average of a large swath of asphalt pixels from the scene for the substrate signature. Spectral averaging of the asphalt pixels prevented irregularities from affecting the output spectral emissivity. Using an asphalt background ensured that the substrate in the target spectra matched that of the test pixels in the emissivity image. This prevented error as a result of differences between substrate materials of the target and test pixels from occurring. Four target signatures were created; one for each parameter estimate of coverage density as well as the measured pure material spectrum.

While ROC curves were created that depict several different methods of detection,

the main algorithm applied to the data was the Adaptive Cosine/Coherence Estimator (ACE) algorithm. This algorithm will be the basis for comparing the best possible target spectrum to use on each target pixel. Four target detection statistics were generated for every target pixel in the scene representing the scores for ACE using each target spectrum. The target spectrum associated with the largest detection statistic at each pixel represents the best spectrum to use for that pixel. Since each target block represents a unique combination of sub-pixel fraction percentage and coverage density, there should be trends associated with use of different target spectra.



Figure 5.37: Full scene image from Blue Heron sensor with the synthetic targets placed inside the bounds of the asphalt parking lot. Targets were blurred with the PSF of the sensor.

### 5.6.1 Red Chalk

Red chalk was the initial example used as its signature was spectrally the most varied visually from the asphalt surface. Targets were created from the parameter estimates calculated in a previous section and followed the 10% sub-pixel coverage step discussed, with full pixel targets being the right-most column. Four target spectra were used in the ACE algorithm to determine under what conditions a particular target spectrum was best suited for detection of a target pixel. Three spectra were created with the estimated parameters from the inversion model along with a asphalt substrate spectrum. The fourth target spectrum came from the empirical data collection and represented the pure contaminant spectrum. Each of the 243 target pixels in the scene were color coded based on the which target spectrum produced the highest detection score. Figure 5.38 shows the results for the red chalk powder with the ACE algorithm. In 171 cases, the best target spectrum for detection was the pure contaminant spectrum. Conditions for these pixels tended to trend towards lowest sub-pixel fraction targets and targets with the highest coverage density. At least one full pixel target for all coverage density levels were best detected by the pure contaminant spectrum.

The high number of target pixels that were best detected by the pure contaminant spectrum were unremarkable as red chalk powder has a novel spectral shape relative to the asphalt surface (i.e. red chalk on asphalt has high contrast to the background and is relatively easy to detect). When the coverage density decreased to its lowest (top row of target pixels), there was a shift in which target spectrum was best fit for detection. In 64 cases, the middle coverage density spectrum was ideal. Most of these did not occur in the row with the matching coverage density parameter (middle row) which was counter-intuitive. The remaining eight pixels came from the highest coverage density mixture spectrum and the lowest mixture spectrum. They occurred in random locations and at low sub-pixel coverages indicating that results for those pixels were likely extremely close and by chance these spectra were best.

Overall, what can be said about this case is that when a target signature is vastly different in spectral shape from the background constituent pixels, the targets are in most cases best detected by the pure material spectrum. In rare cases where the targets are extremely sparsely contaminated, mixture spectra may be considered as an improved method for detection.

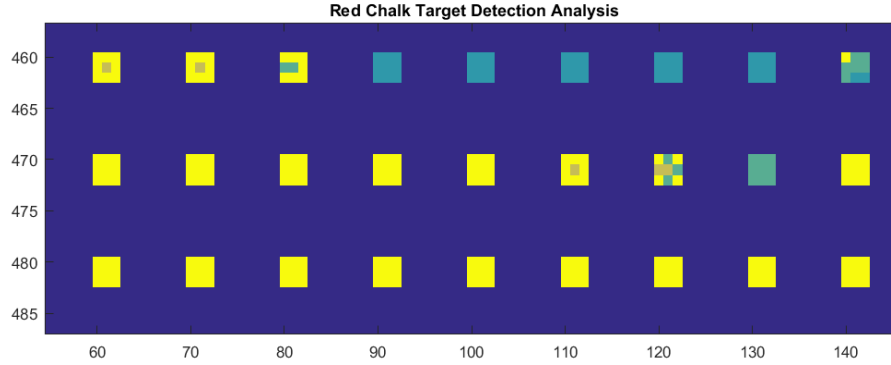


Figure 5.38: Target detection analysis of synthetic red chalk targets using the ACE algorithm. The best target spectrum for each target pixel are colored as pure contaminant spectrum (yellow), highest mixture spectrum (orange), middle mixture (green), lowest mixture (lighter blue). Background pixels are labeled dark blue.

### 5.6.2 Silicon Carbide

Analysis of ACE target detection on silicon carbide targets using four unique target signatures is presented in Figure 5.39. Pixels were colored coded based on the highest magnitude target detection statistic found from the four detection maps. Each pixel was labeled with the appropriate color. Pixels which were best detected by the pure target spectrum were colored yellow. In the case of silicon carbide targets, all full pixel targets, regardless of coverage density were best detected by the pure target spectrum. This means under conditions where the background surface is at least somewhat contaminated with material, the best method is to use the pure material. In cases below 50% sub-pixel fraction, most target pixels were again best detected in ACE using the pure target spectrum. In total, 149 pixels were best detected by the pure target spectrum.

For higher sub-pixel fraction targets, there was a clear trend towards well-matched target signatures. The highest coverage density targets (found in the lowest row of target blocks) had several high sub-pixel fraction target blocks that were best detected by the mixture using the same coverage density. A total of 32 pixels from the highest coverage density were detected by the appropriately matched density target spectrum, but so were 25 additional pixels from the other rows. These all occurred at high sub-pixel fractions, but had a lessened effect at lower coverage density. This seems to indicate that sub-pixel fractions can have a strong influence on which target signature to use when the targets are not significantly different from the background. High coverage

density targets at 50% sub-pixel fraction were detected by the same spectrum as some of the lowest density targets at 90% sub-pixel fraction.

The second mixture target spectrum demonstrated the same trend with pixels at lower coverage densities being detected by it better than other target spectra. In this case however, the lowest coverage density targets were only better detected by this spectra when they were not on corners of target blocks. This likely is an effect of the signal degradation by convolving synthetic targets with the sensor point spread function. Corner target pixels degrade more due to the increased effect of background pixels on the signal. In total, 24 pixels were best detected by the second mixture target spectrum, with 18 of them occurring in the lowest mixture row (top row in Figure 5.39).

Like the last example, only a handful of target pixels were best detected by the target spectrum created with the lowest coverage density parameters. These locations were not random, but occurred in the center pixels of the lowest target sub-pixel fractions and densities. This indicates that there is use for low contaminant mixture targets in the detection of sub-pixel targets in extremely low coverage density. At extremely low sub-pixel fractions below 50%, the pixels were mostly best identified by the pure material spectrum, but there is not a clear trend in this region. The likely explanation is that at such low pixel fractions, detection statistics for each of the input spectra are so low that it does not truly matter which spectrum is used.

The main takeaway from the example of silicon carbide is that when a target signature does not have unique features to distinguish it from the background, target spectra need to be thoroughly considered case by case. Silicon carbide does have a unique signature, but it is relatively flat and highly emissive across the longwave infrared spectral range. This could cause a detection algorithm such as ACE to mistake it for a background pixel under the wrong conditions. In real cases one might choose to use a bank of target signatures that span a range of average densities to ensure best detection across a range of test pixel conditions.

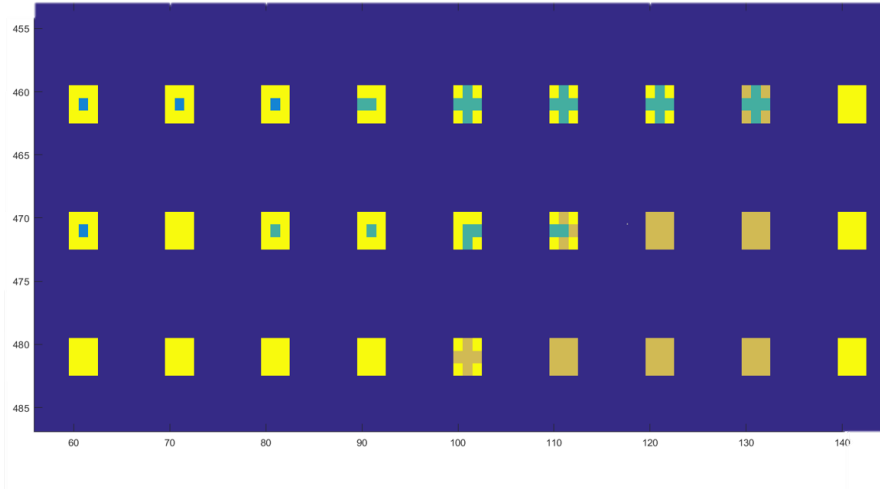


Figure 5.39: Target detection analysis of synthetic silicon carbide targets using the ACE algorithm. The best target spectrum for each target pixel are colored as pure contaminant spectrum (yellow), highest mixture spectrum (orange), middle mixture (green), lowest mixture (lighter blue). Background pixels are labeled dark blue.

## 5.7 Blue Heron Real Airborne Data

Real data was collected in November of 2016 where sparsely contaminant targets could be directly placed into the scene. This removed the need to apply a blur kernel using the point spread function onto synthetic targets in airborne images. It also allowed for a real world example for which to apply the created parameter inversion model and target detection analysis. Targets were created by applying two contaminant materials (silicon carbide and fused silica powder) in two coverage density amounts ( $0.025$  and  $0.050 \frac{g}{cm^2}$ ) over an area that was approximately  $1.5 m^2$ . Ground images of each density amount can be seen in Figure 5.40. This created four unique targets of varying coverage density and material, each bounded by aluminum foil wrapped 2x4 lumber as seen in Figures 5.36 where 25 and 50 grams of silicon carbide powder was distributed in an aluminum bounded target. This material, like the empirically measured targets using the FTIR instrument, were applied using a sieve. Because this sieve in this example is significantly smaller than the area of the targets, material was only spread as evenly as humanly possible.

From an aerial perspective, the collected radiance data from the Blue Heron sensor



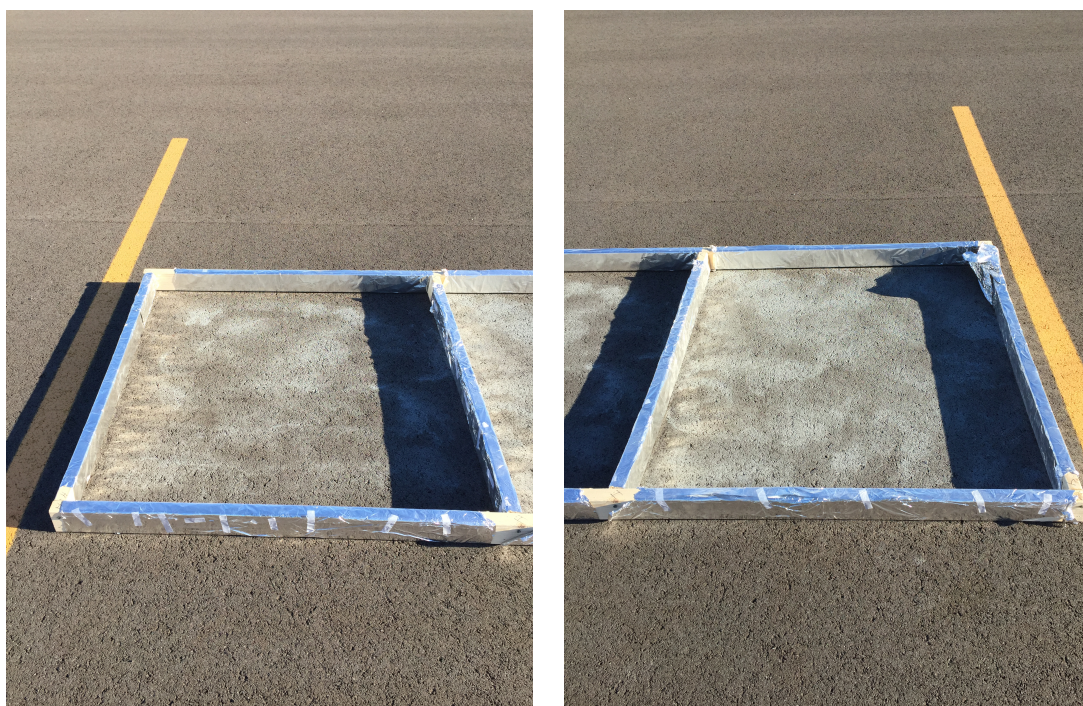


Figure 5.40: Left: 25g of silicon carbide powder placed across target area surrounded on all sides with aluminum wrapped 2x4 lumber. Aluminum helps provide high fidelity targets in airborne data. Right: 50g of silicon carbide powder placed across target area surrounded on all sides with aluminum wrapped 2x4 lumber. Aluminum helps provide high fidelity targets in airborne imagery.

has striping due to pixel malfunctions mainly on the leftmost section of the sensor array. This error can be removed using ENVI based software tools. An example of the collected radiance map with the targets can be seen in Figure 5.41, where the Blue Heron sensor flew over a parking lot in the Gates, NY region with our targets present in-scene. In this false color image there are six targets, with two pairs of adjacent targets and two stand-alone ones. All of these targets exist roughly halfway down the image and are pushed all the way to the left edge. The two individual targets are of Quartz sand and large particle fused silica placed in the same sized space, but with an optically thick layer present. The two sets of adjacent targets are silicon carbide (green targets) and fused silica (pink targets) powders. Clearly bounding all targets are darkened lines representing the highly reflective aluminum wrapped lumber used to bound targets. These clearly define fidelity of the contaminant mixture target space by creating strong contrast between materials.





Figure 5.41: Full scene image from Blue Heron sensor with the synthetic targets placed inside the bounds of the asphalt parking lot. Targets were blurred with the PSF of the sensor.

### 5.7.1 Target Detection Analysis

Prior to applying real target pixels to the parameter inversion model, target detection analysis was performed using ENVI's target detection wizard. Since Blue Heron pro-

duces radiance maps of a scene, the images first needed to be converted into emissivity space. This was accomplished by performing in-scene atmospheric compensation on the radiance image to achieve ground leaving radiance without upwelling contributions. Compensated radiance imagery was then directly solved for emissivity using the emissivity normalization application. The resulting emissivity image could then be used within the target detection wizard in ENVI to analyze how effective pure target spectra could be in detecting each sparsely contaminated surface.

Table 5.4: Target detection statistics for fused silica and silicon carbide targets in Blue Heron imagery.

Detection Scores for Blue Heron Targets Using ACE (ENVI)			
Material Type	Threshold	Target Pixels Detected	False Alarms
Fused Silica	0.096	38	2
Silicon Carbide	0.035	19	1

Images presented in Figure 5.38 are target detection statistic images for fused silica and silicon carbide using the pure contaminant spectra for both materials respectfully. Numerical analysis of the detection scores are presented in Table 5.4. Fused silica represents a contaminant material that has strong spectral contrast with the underlying substrate, while the silicon carbide targets have little contrast with the asphalt. In applying the pure fused silica spectrum to ACE, nearly every target, full and sub-pixel alike appeared to be detected in the image before false alarms appeared. Given the spectral contrast between the test pixel and background, this result is the expectation based on results presented in the previous section.

With a higher threshold value, the results for the silicon carbide targets also confirmed examinations from the previous sections. While 19 target pixels were identified from the image, a higher threshold was needed and many of the sub-pixel edge targets were not discovered before false alarms began to dominate. This leads credence to the idea that spectral contrast between the background and test pixels has an important impact on the target spectrum that should be applied in this detection algorithm.

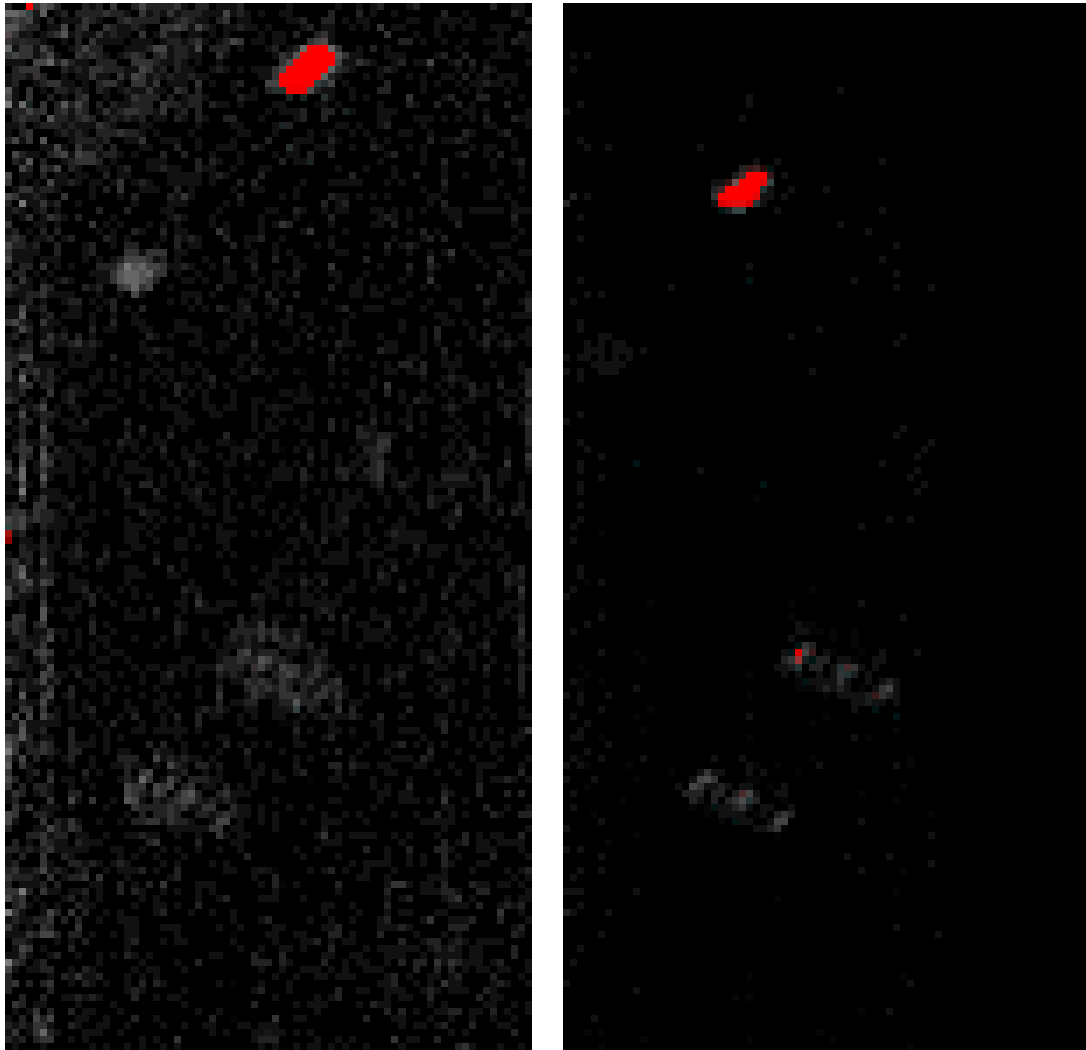


Figure 5.42: Left: Detection score map for ACE run with pure fused silica spectrum as target spectrum for Blue Heron data collection. Target pixels were detected at a 0.096 threshold with 38 target pixels identified to two false alarms. Right: Detection score map for ACE run with pure silicon carbide spectrum as target spectrum for Blue Heron data collection. Target pixels were detected at a 0.035 threshold with 19 target pixels identified to one false alarm.

### 5.7.2 Application into the Inversion Model

Given the excellent detection of the two materials using the ACE algorithm, the next step was to examine if the parameter inversion model could be used to correctly estimate the amount of material on the surface by accurately determining the coverage density

in the four types of targets. Both fused silica and silicon carbide materials were placed on the surface in targets of 0.0025 and 0.0050  $\frac{g}{cm^2}$ . Since material was applied to each target using a sieve, the material was not perfectly uniform coverage density across the entire target square (see Figure ). Given the sensor GSD for the collection, there were at least four full target pixels in each target square that could be used to make an average mixture spectrum for each of the four targets.

In order to pass an emissivity spectrum from the airborne data into the parameter inversion model, emissivity signatures of both the pure contaminant and bare substrate spectra must be determined. The pure substrate signature was calculated by taking the average of 16 pixels in an open section of the asphalt parking lot from the airborne emissivity image. Consideration was made to ensure that pixels chosen were not near vehicles, edges or buildings. The pure contaminant spectrum came from a resampled version of a D&P FTIR instrument emissivity from a previous empirical data collection. Resampling occurred to match FTIR datapoints to the wavelengths associated with the airborne spectrum. Results are presented in Table 5.5 where estimates for coverage density are compared to each target's known value for the parameter.

Table 5.5: Parameter inversion estimates for coverage density of real Blue Heron targets

Coverage Density Estimates for Real HSI Targets			
Material	Coverage Density Applied	Coverage Density Estimated	Difference
Fused Silica	0.025 $\frac{g}{cm^2}$	0.0022 $\frac{g}{cm^2}$	0.0003 $\frac{g}{cm^2}$
	0.050 $\frac{g}{cm^2}$	0.0053 $\frac{g}{cm^2}$	0.0003 $\frac{g}{cm^2}$
Silicon Carbide	0.025 $\frac{g}{cm^2}$	0.0020 $\frac{g}{cm^2}$	0.0005 $\frac{g}{cm^2}$
	0.050 $\frac{g}{cm^2}$	0.0055 $\frac{g}{cm^2}$	0.0005 $\frac{g}{cm^2}$

In all four cases, the estimated coverage density values for the targets were within 0.0005  $\frac{g}{cm^2}$  of the actual coverage density present on the surface. Results for the fused silica material indicate that estimates are extremely close to the actual amount applied, however this table only provides results from a single run of the inversion model. For deeper analysis, the inversion model was run 1000 times and basic level statistical analysis was performed. This found that the average coverage density estimates for the fused silica mixtures were 0.0037 and 0.0063  $\frac{g}{cm^2}$  respectfully. These results are further from the single run estimates, but still close to the reference data. Variances for each mixture of fused silica were extremely low (less than  $5 * 10^{-6}$ ) demonstrating that the

spread of estimates from the mean value is low. Histogram analysis in Figure 5.43 and 5.44 shows that for the each case, the deviation between scores is higher than expected. Scores for the larger coverage density fit a pseudo normal distribution, but the smaller fused silica mixture failed to fit that distribution type. The distortion from a normal distribution in the lowest mixture is such that the most frequent bin has a significantly lower magnitude than the bin which contains the mean value of the distribution. Both distributions are wider than expected, indicating that the estimates had variability despite being centralized near the reference density. An increase in the varied results for this material could be due to the reduction in the number of bands used for processing. Because of spectral disagreement between pure material spectra and the mixtures, only the wavelengths between 10 and 11.5  $\mu m$  could be used for estimation. While the inversion model is robust, an increase in the number of wavelengths used should help increase the confidence of the estimations and reduce this wider distribution.

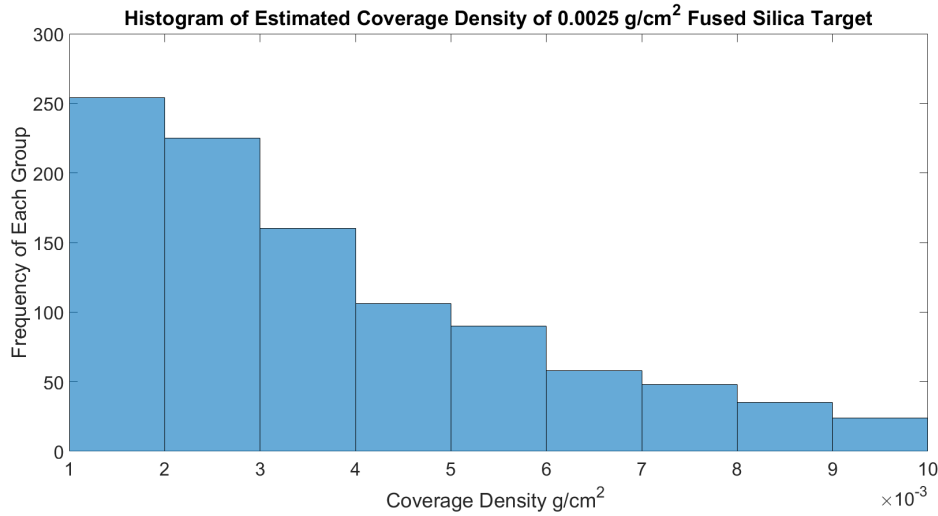


Figure 5.43: Histogram of 1000 parameter inversion runs on the 0.0025  $\frac{g}{cm^2}$  fused silica coverage density target.

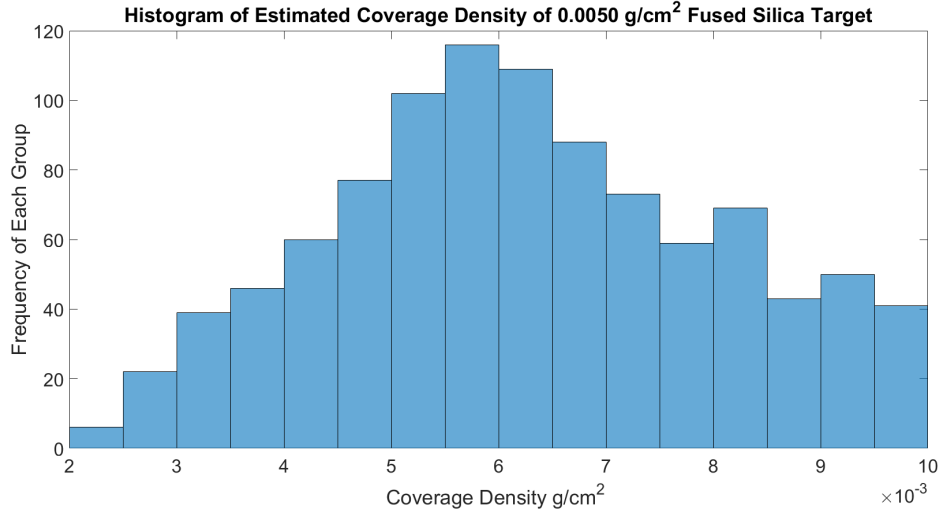


Figure 5.44: Histogram of 1000 parameter inversion runs on the  $0.0050 \frac{\text{g}}{\text{cm}^2}$  fused silica coverage density target.

Silicon carbide targets from the Blue Heron data collection were also run through the parameter inversion model 1000 times and analyzed against the single run results presented in Table 5.5. Unlike the fused silica test, the silicon carbide contained a large majority of its constituent wavelengths, improving the calculations. Only a handful of wavelengths at  $8 \mu\text{m}$  and at  $10.5 \mu\text{m}$  needed to be culled for the model. This is a similar result to the empirical dataset measured by the D&P FTIR instrument. The latter of the two groups is the location of the cross-over point where all spectral signatures have roughly the exact same spectral emissivity. Estimated mean coverage densities for the two mixture targets were  $0.0027$  and  $0.0049 \frac{\text{g}}{\text{cm}^2}$  respectfully, converging even closer than the single model runs from the previous table. Variance calculations proved that there were smaller deviations within the data than in the fused silica example, with variances being  $2.6 * 10^{-6}$  and  $3.8 * 10^{-6}$  respectfully. When analyzing the frequency of the estimation for each mixture in the histograms, it becomes obvious that the spread of data is reduced from the previous example. While both example appear to have an elongated right tail, the data is centered at the expected locations and with a narrower, taller distribution. One reason for a long right tail in the distributions is that a larger portion of the range dictated by the boundary conditions is to the right of the expected mean. There will always be a small probability that the model inversion estimates a value within the coverage density range set by the model, but outside the expected

distribution.

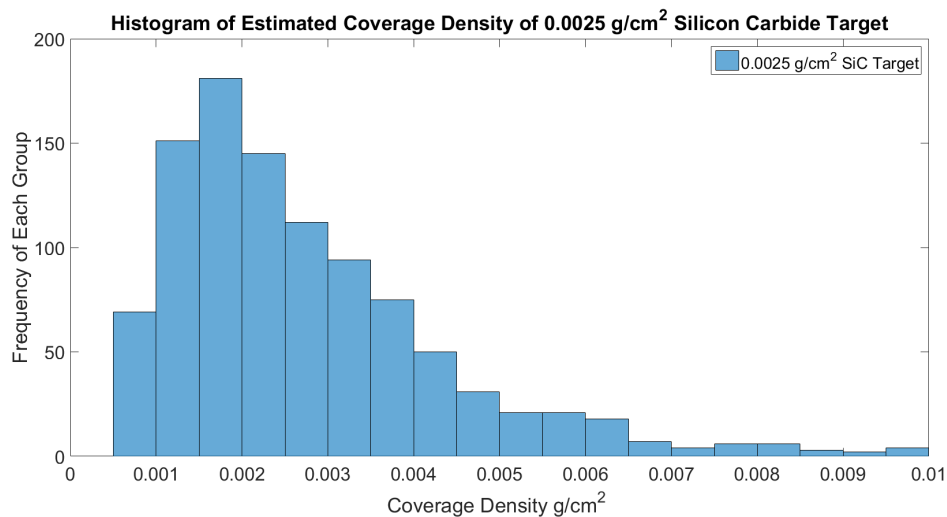


Figure 5.45: Histogram of 1000 parameter inversion runs on the 0.0025  $\frac{g}{cm^2}$  silicon carbide coverage density target.

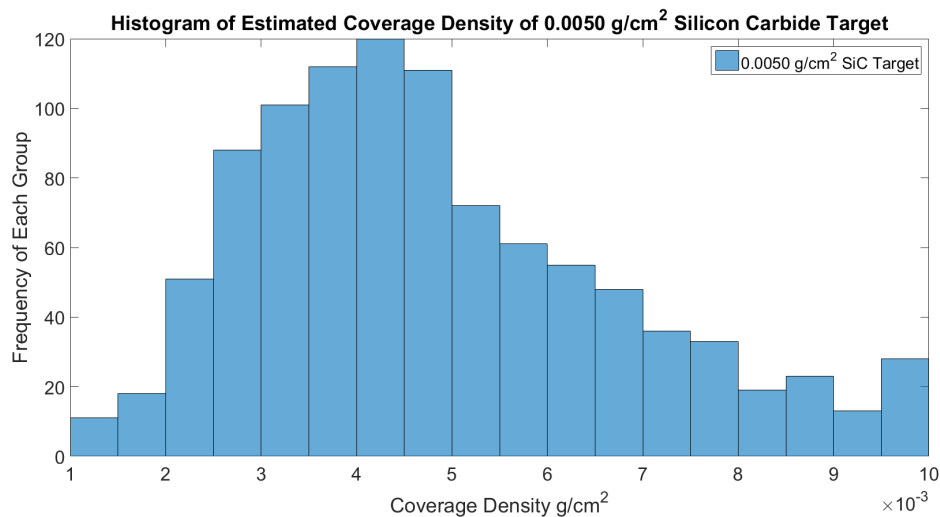


Figure 5.46: Histogram of 1000 parameter inversion runs on the 0.0050  $\frac{g}{cm^2}$  silicon carbide coverage density target.

For the fused silica targets, the reconstructed spectra from the inversion model are presented against the aerial collected emissivity spectra. The pure asphalt signature comes from the average of 16 asphalt pixels in the scene while the pure contaminant spectra for both materials is from empirical data collections that occurred in other experiments. Both mixtures are again the average of center pixels in the target squares from the airborne collection. For fused silica, a  $1.5 \mu m$  range between 10 and  $11.5 \mu m$  represented the only region in the spectrum that was usable due to differences between the aerial measurements and the pure material emissivity spectra. With such a low number of wavelengths being used for calculation, the results as previously discussed had a somewhat larger variability, but were still roughly centralized around the expected result. Using the first run results from table 5.5, spectral mixtures were recreated in the NEFDS forward contamination model and overlayed with the spectral measurements from the airborne data in Figure 5.47.

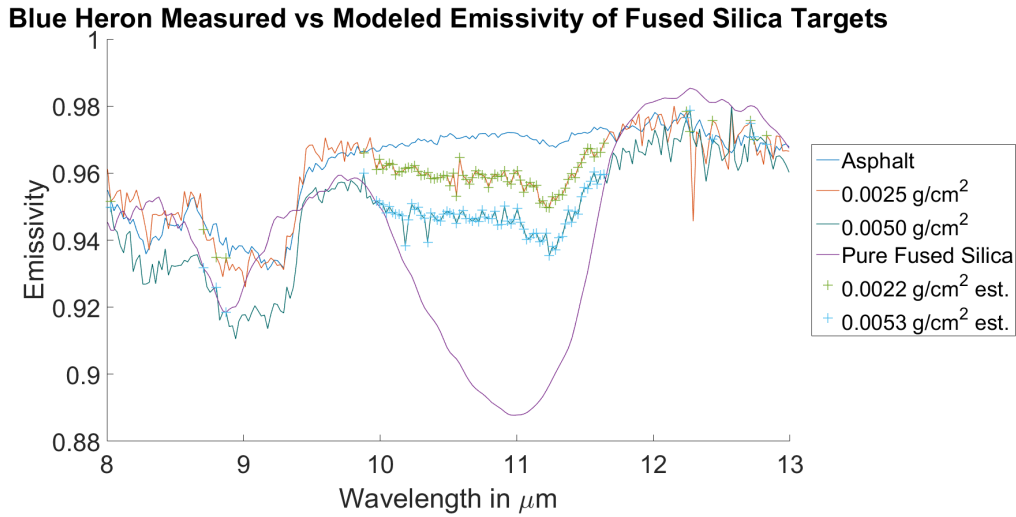


Figure 5.47: Measured vs Modeled Estimates for fused silica targets placed in Blue Heron 11/12/17 flyover. Estimated coverage density for both targets is in near perfect agreement with the actual amounts placed in-scene.

A much larger swath of wavelengths were able to be included in the calculations for silicon carbide as both mixture spectra fell within the envelope created by the pure material spectra. This helped produced results that were more localized around a mean and



even better physical representations than the single run results used in the reconstruction of the mixture spectra. The results of which are presented in Figure 5.48. Alongside the pure material reflectances and airborne emissivities of both coverage amounts, reconstructed spectra (labeled with disconnected colored plus signs) were overlayed for a visual comparison. The results of both of these examples indicate that it may be possible to extrapolate out a coverage density (and therefore total contaminant mass) from an aerial pixel using this method.

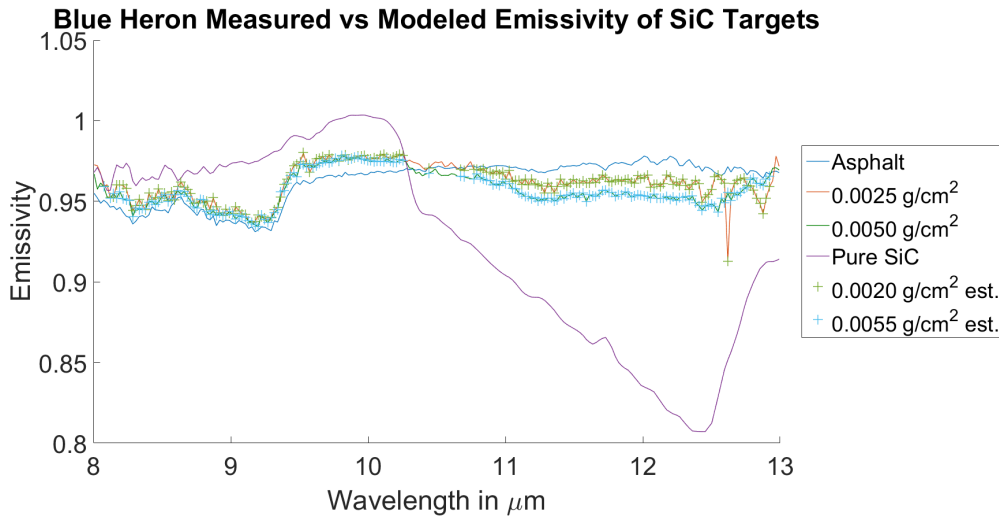


Figure 5.48: Measured vs Modeled Estimates for silicon carbide targets placed in Blue Heron 11/12/17 flyover. Estimated coverage density for both targets is in near perfect agreement with the actual amounts placed in-scene.

### Application to Unknown Target Locations

If the desired target material was known but its location in a scene was not, a step-by-step process as seen in Figure 5.49 could be undertaken to find and determine contaminant mass quantities from an airborne scene. Initially, the scene must be converted from radiance to emissivity or reflectance space by performing atmospheric compensation and temperature emissivity separation. Target spectra representing the pure material as well as several mixtures between the pure material and underlying substrate surfaces are used to perform target detection with the desired algorithm. Potential target pixels can then be identified and ranked by detection score from likeliest target to least likely target.

Each target pixel can then be run against the parameter inversion process  $n$  times and statistical averages can be computed. As the number of runs increases, the average coverage density will converge to the best estimate for the parameter. This can be used to determine the total contaminant mass within the IFOV by multiplying the coverage estimate and IFOV of the sensor together. The process then repeats for the next highest detection score until all target pixels are identified.

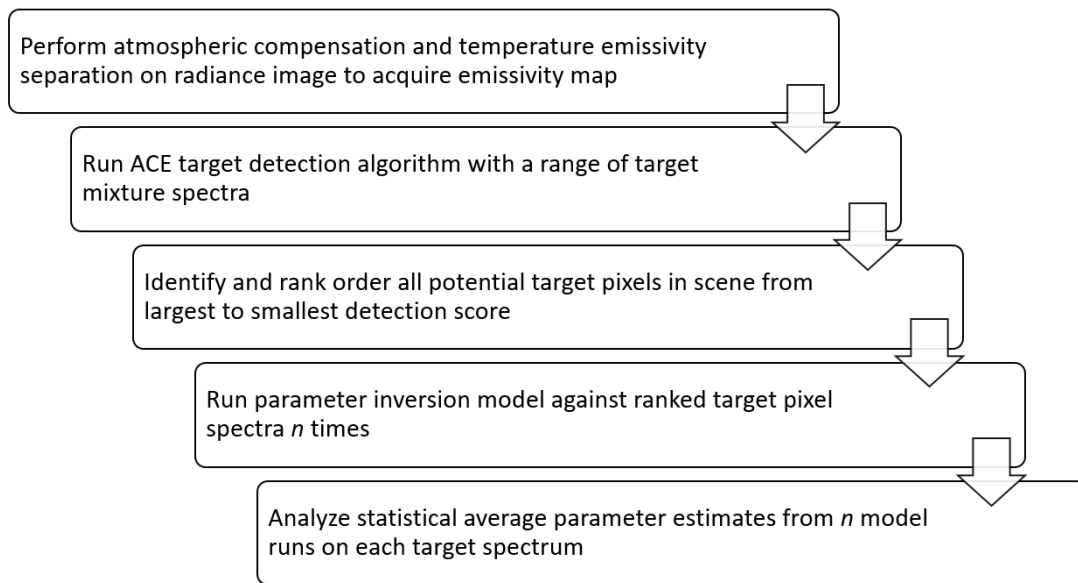


Figure 5.49: Process to incorporate inversion model estimator with target detection

Using the parameter inversion process in this way is more computationally efficient than attempting the inversion process on all pixels within an emissivity image. The number of trial runs for each inversion can also increase when analyzing only the highest likelihood targets. This improves the estimates for coverage density and mass by increasing the sample set of estimates.



## Chapter 6

# Summary

The determination of physical properties regarding a sparsely contaminated surface with powders is important in several fields including industrial pollution monitoring. The target signatures of powders can be affected by the particle size, shape and distribution of particles. Their crystalline structure affects the optical properties of the material and angular effects can cause shifts in the signature in certain materials. The goal of this research was to determine how we can improve the characterization of low density powder contaminated surfaces with longwave infrared imagery. Our initial focus was to try and estimate the total contaminant mass present on a sparsely contaminated surface using a parameter inversion model designed in the spirit of the NEFDS contamination model.

Results from NEFDS contamination model inversion indicate that empirically measured intimate mixtures can be used to determine a coverage density and contaminant mass from a pixel with relative success using several different types of materials. These results were achieved by applying varying contaminant amounts to several types of surfaces and making emissivity measurements with the Design and Prototypes FTIR and Surface Optics Corporation Reflectometer. These grouping of mixture measurements were made with different combinations of red chalk, silicon carbide, fused silica and quartz sand onto several different types of simple substrates. In most cases, the coverage density amounts estimated for the sparse contaminant amounts were similar to those actually applied to the surfaces being measured. On occasion, uneven material distribution caused issues with the measurements. Coverage density estimates helped derive the total contaminant mass on the surface, typically within a factor of two from the actual amount applied. Other parameters including the  $\beta$  parameter were estimated

in this model, but no solid conclusion can be made from this parameter as it was used as a model fitting parameter in the original NEFDS forward contamination model.

Extinction cross section was also estimated in the parameter inversion model. As a contaminant material property, this was not supposed to have variation between different amounts of contaminant. While estimated results typically did not vary between mixture amounts, the extinction cross section was never in perfect agreement between mixtures in a collection. Therefore attempts were made to directly measure this parameter using an integrating sphere and later on, a blackbody. Compressed disks of varying contaminant number density were used to find radiance ratio variation at each wavelength. The slope created in a semi-logarithmic plot at each wavelength represented the extinction cross section at that wavelength. As each wavelength was processed, an extinction cross section signal was built up with for the material. The findings of this research indicate that the amount of contaminant material placed in the disks was likely too large relative to the coverage density boundary conditions set forth by the NEFDS forward contamination model. At larger coverage density, the number density parameter becomes insensitive due to the stacking of particles and produces diminishing returns for radiance ratio. When deriving the cross section from disks that had coverage densities within the model range, the results improved somewhat. Specifically in fused silica where the data fell within a factor of two of the estimated extinction cross section found using the parameter inversion model. While the use of these results would greatly reduce the complexity of the parameter inversion model, the extinction cross section measurements were too low in magnitude. This caused the coverage density parameter to reach its maximum boundary condition for all mixtures, even with the improved results. This occurs because the area fraction term described in

$$f = \exp\left[\frac{\alpha(\lambda)\frac{n}{A}\ln[1 - \phi_0(1 - e^{-\beta\frac{n}{A}})]}{\phi_0(1 - e^{-\beta\frac{n}{A}})}\right], \quad (6.1)$$

can only have a magnitude shift by changing the extinction cross section parameter or the coverage density parameter. Since coverage density has clear defined boundaries set, a decreased extinction cross section magnitude will cause problems in the estimation of the coverage density.

The estimated parameter information from the empirical measurements was then used to inject synthetic targets into real longwave hyperspectral data from the Blue Heron sensor. Targets were created with the NEFDS contamination model parameters so that each block of pixels had a unique combination of coverage density and sub-pixel

fraction coverage. A total of 27 3x3 target blocks were placed on a parking lot substrate and degraded with the calculated point spread function of the sensor. Target spectra for each mixture and the pure contaminant emissivity were used in the ACE algorithm to determine the spectra best suited to detect each condition. The results show that when the material signature has significant spectral character relative to the background material spectra, most cases will be best detected by the pure contaminant spectrum. In cases where the target is not wildly different from the background, more consideration must be placed in what type of target signature should be used in ACE.

Real targets were recently placed in a data collection with the same sensor and tested against ACE and the parameter inversion model. Testing found that when airborne hyperspectral imagery of targets was passed through the parameter inversion model, extremely good estimations of coverage density occurred for the two materials in scene. This result demonstrates the robustness of the parameter inversion model to achieve reasonable results for a total contaminant mass on the surface.

## 6.1 Future Considerations

Going forward, there are several aspects of the research that should be considered for future evaluation. Firstly, the examination of extinction cross section of powders should be performed as described in Chapter 4, but with much lower density contaminants. While disks were made using 0.5-2.0% contaminant, that created much larger coverage density values that were examined by the NEFDS forward model. Any disks made for this purpose should not have more than  $0.01 \frac{g}{cm^2}$  of contaminant in them. While the extinction cross section was calculated using 3-4 disks, it is recommended that future calculations use more disks to build up a better defined slope at each wavelength. In some cases, having three disk measurements did not provide clarity on the slope of the line. With this in mind, it is possible that the measurements do not produce a stable result even at extremely low coverage densities or that the process is non-linear in this range which would require a different solution be developed.

It is also worth examining whether the physical properties of the powder have shifted when put under the immense stress of a 40 ton disk press. All powders were measured for crystalline structure using a x-ray diffraction instrument prior to experimental trials. If the material crystalline structure does change under the pressure of making a disk, the structure could be re-measured using an x-ray diffraction instrument by breaking apart a previously made disk and placing its contents onto a slide for analysis.

Finding a way to acquire the index of refraction parameters necessary to simulate sparse surfaces of the powder materials in  $\mu$ DIRSIG would be extremely beneficial as well. Simulations of sparse contaminants that are accurate help provide specific emissivity information for surfaces under specific conditions. While the measured optical constant values did not work with the ellipsometer, this was likely because of disk preparation problems. If given more time, properly created disks could yield good results for the  $n$  and  $k$  parameter as was done in Blake (2017). Other methods described in that paper could also be explored if the proper instrumentation is available.

Moving forward, the parameter inversion model should also attempt to incorporate the improvements made in recent editions of the NEFDS contamination model. The parameter inversion model was created using documentation for version 15.0 of the model. Currently, the Cortana Corporation is working on version 18.1, which has significantly updated the  $\beta$  parameter to account for particle size distributions. Clearly from the histogram analysis of the parameter, it is extremely model insensitive and essentially has no impact on the results. Version 15.0 defined this parameter as a fit parameter for the model, so this improvement gives the parameter clearer purpose in the calculations. It is worth examining if the NEFDS contamination model is even the best model for the problem of characterizing sparse intimate mixture of particles. While it was convenient and had good results, the NEFDS contamination model is not a robust way to determine a lot about a material as it only contains three parameters.

## Appendix A

# X-Ray Diffraction Data

This appendix chapter contains measurements of x-ray diffraction for two additional materials not included in the main text. The first material is fused silica powder which was purchased from Washington Mills. Figure A.1 shows the resulting intensity chart given sample angle. Normally, the intensity plot would contain discrete narrow intensity features as seen in the silicon carbide example found in the main text. These discrete peaks would allow for the matching of crystalline structures from a database of materials to determine if one or several different structures exist within the material. Fused silica has no discrete peaks, but rather a single wide peak that ranges from 10-40 degrees. When no discrete peaks are present in the measurement, the material is said to be amorphous which means that no defined crystalline shape is present within the material.

Figure A.2 shows that about two dozen low magnitude narrow peaks do exist in the red chalk sample. Since data from the company that provided the chalk powder (Irwin Tools) showed that the material was made of calcite and red iron oxide, all x-ray diffraction data from the spectral library for both these materials was cross-checked against the peaks measured. Library reference data was positioned below for both materials so that visual comparison of the location and intensity of the peaks could be made.



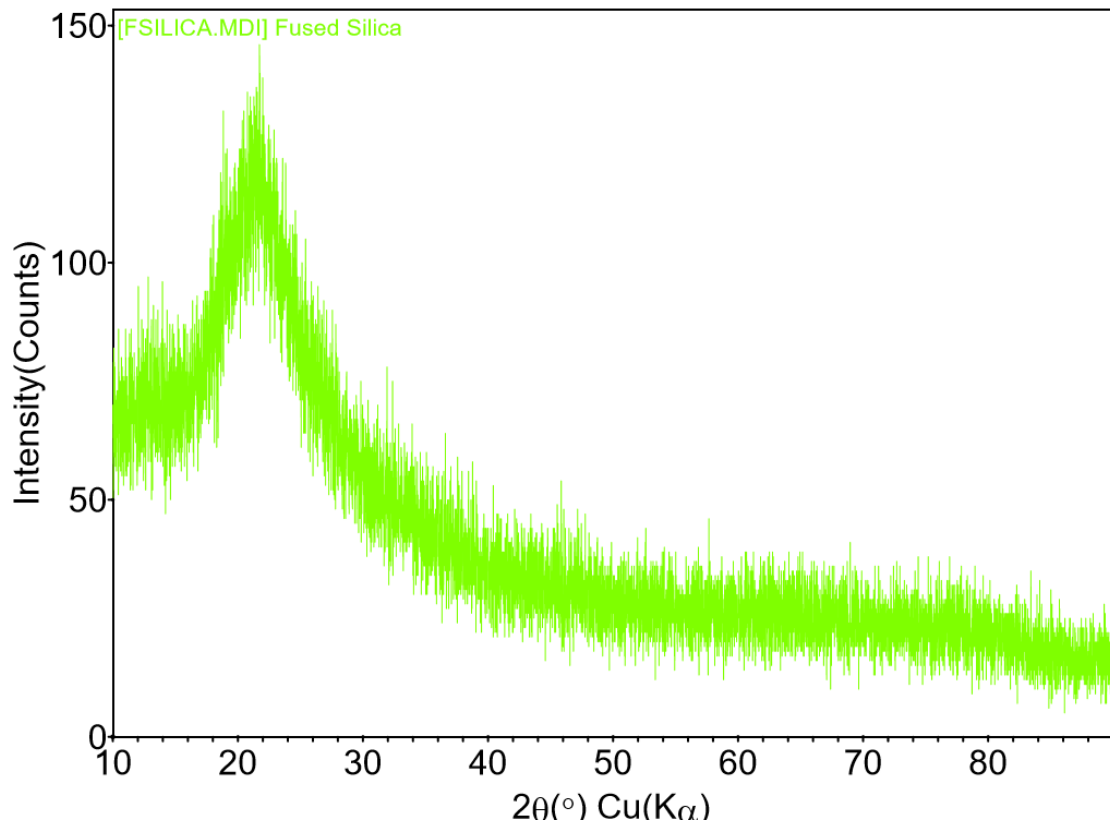


Figure A.1: X-ray diffraction images of Fused Silica powder. Fused Silica has one broad intensity lobe, indicating that the material is comprised of multiple types of materials. The result is that the Fused Silica is amorphous, not crystalline like the other materials. Data was collected in the material science department at the Rochester Institute of Technology in August 2016.

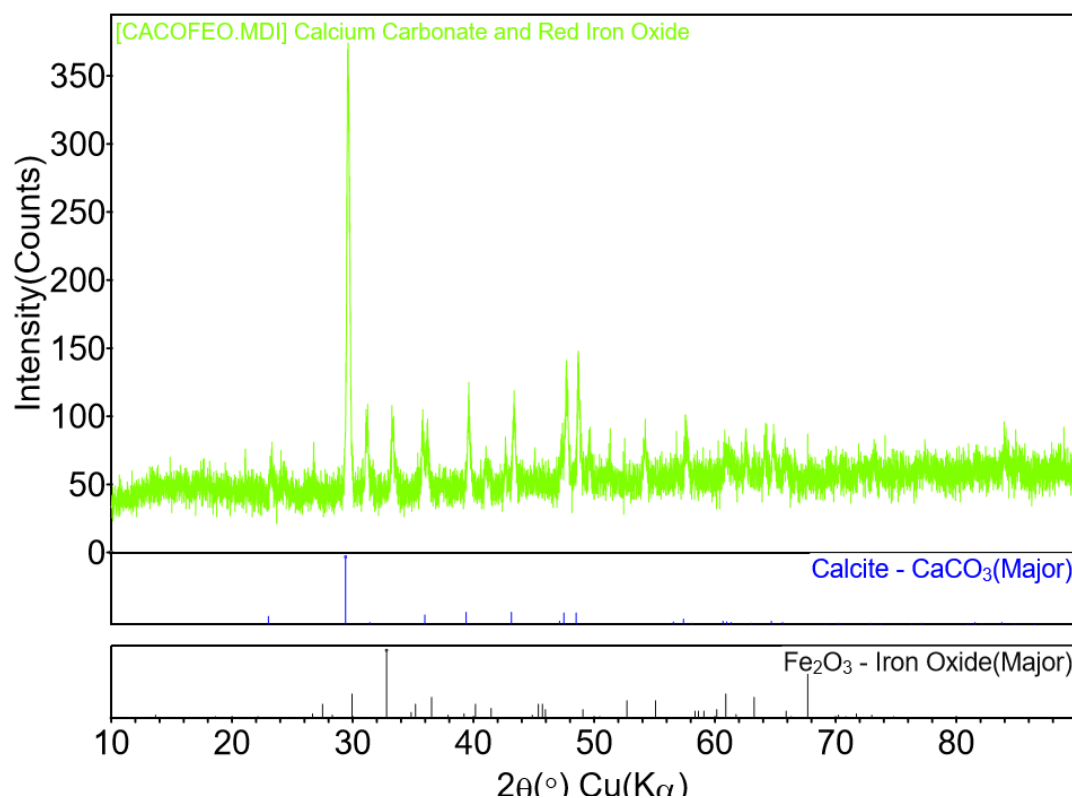


Figure A.2: X-ray diffraction images of Red Chalk powder. This confirms the technical data sheet that stated the material was a combination of calcium carbonate dyed with red iron oxide powder. Data was collected in the material science department at the Rochester Institute of Technology in August 2016.

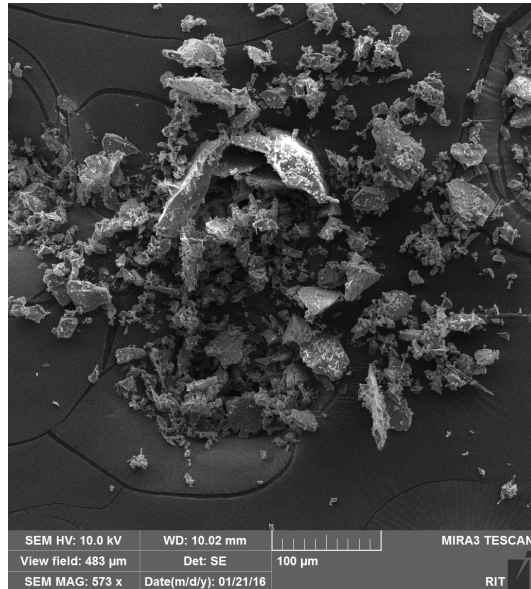


## Appendix B

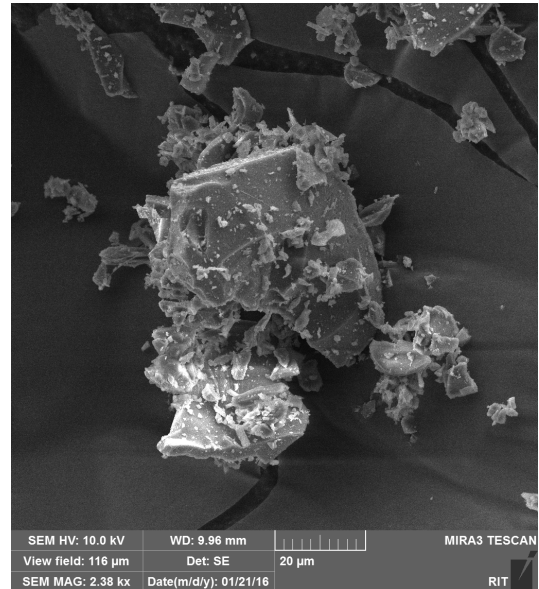
# Scanning Electron Microscope Images

Scanning electron microscope (SEM) imagery was taken for all powders purchased through Washington Mills and found in RIT storage. Besides the silicon carbide example shown in the main text, there were four additional materials examined with SEM imagery. They were red chalk powder, fused silica powder, duralum white powder and duralum brown powder. The latter two materials were later discarded for lack of significant spectral features in the longwave infrared, but were included in this text. The fused silica powder from Washington Mills showed unique features in its composition. Since it was already determined to be amorphous, the material was expected to have a complete lack of uniformity to particle shape and size. The SEM imagery seems to indicate that this was the case. Particles are jagged and inhomogeneous. Relatively larger particles exist (less than  $50\text{ }\mu\text{m}$ ), but many smaller particles are electrostatically attached to these larger particles as can be seen in the highest resolution imagery.

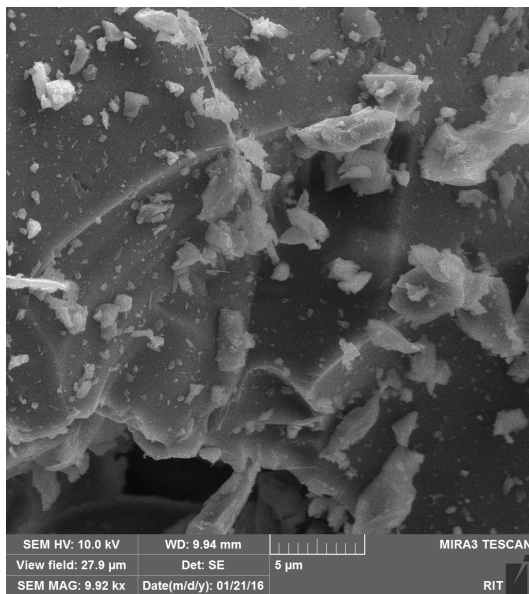
Red chalk powder is significantly different in its composition. Since the material is used for construction, the particles are designed to be uniquely combined. Larger calcium carbonate particles are present (around  $50\text{ }\mu\text{m}$ ) while most of the smaller particles are red iron oxide which are extremely small and attached to the large particles. This is likely by design as the red iron oxide is used as a dying agent for the chalk.



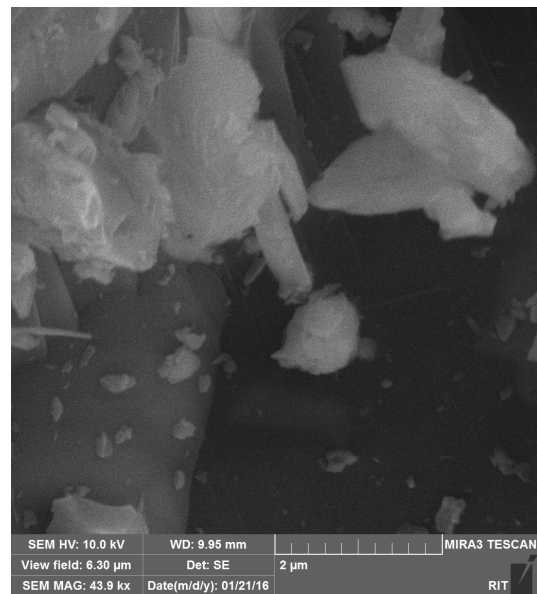
(a) SEM image of Fused Silica Powder at 573x zoom



(b) SEM image of Fused Silica Powder at 2380x zoom

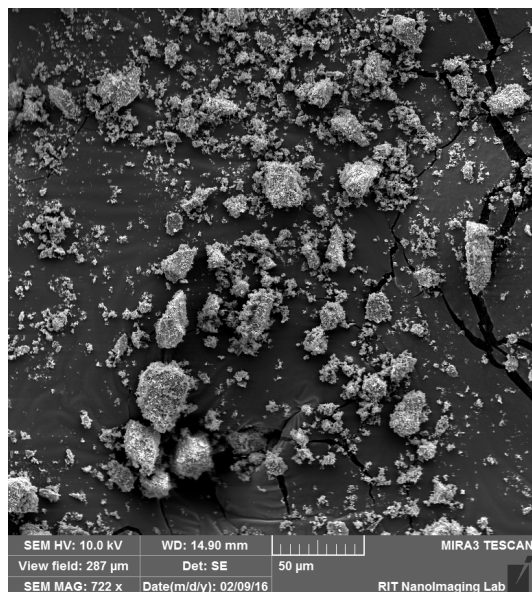


(c) SEM image of Fused Silica Powder at 9920x zoom

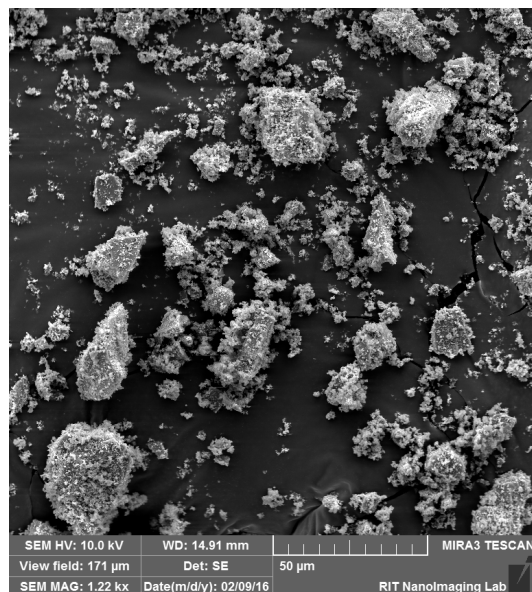


(d) SEM image of Fused Silica Powder at 43290x zoom

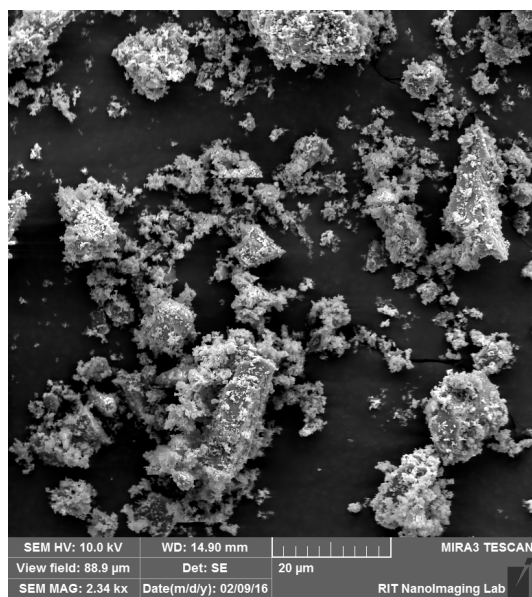
Figure B.1: Scanning Electron Microscope (SEM) images of Fused Silica powder at various zooming distances



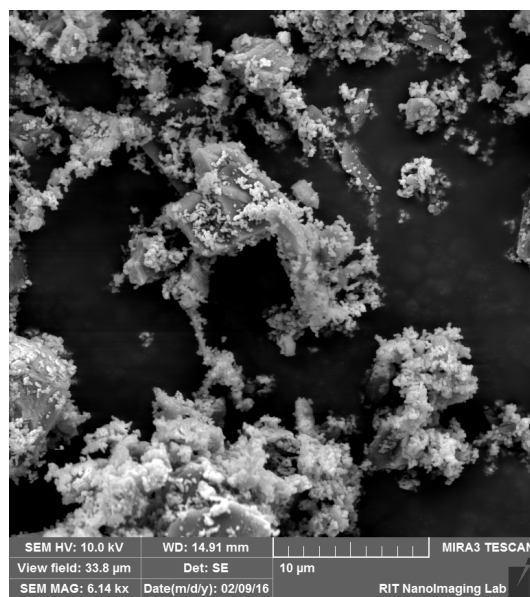
(a) SEM image of Red Chalk Powder at 722x zoom



(b) SEM image of Red Chalk Powder at 1220x zoom

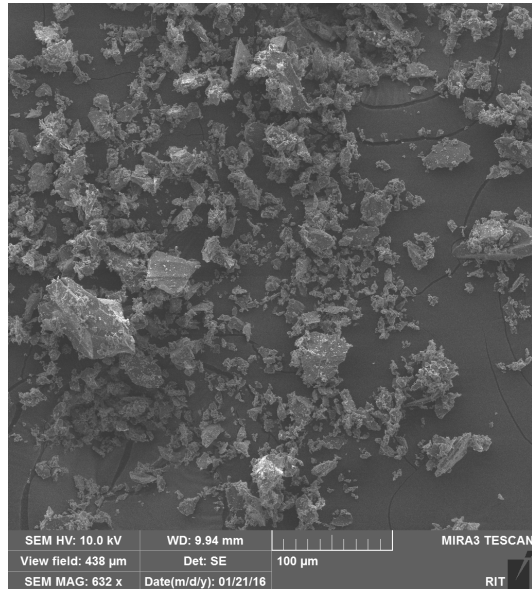


(c) SEM image of Red Chalk Powder at 2340x zoom

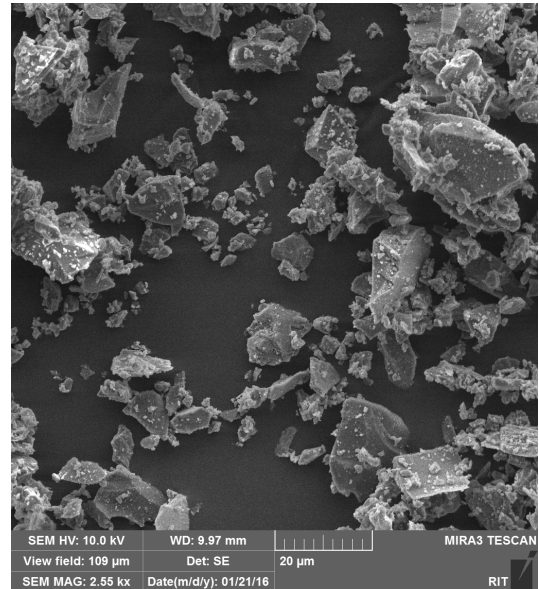


(d) SEM image of Red Chalk Powder at 6140x zoom

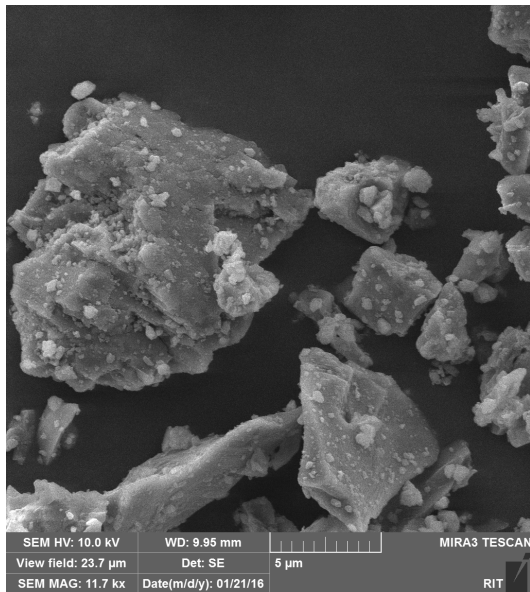
Figure B.2: Scanning Electron Microscope (SEM) images of Red Chalk powder at various zooming distances



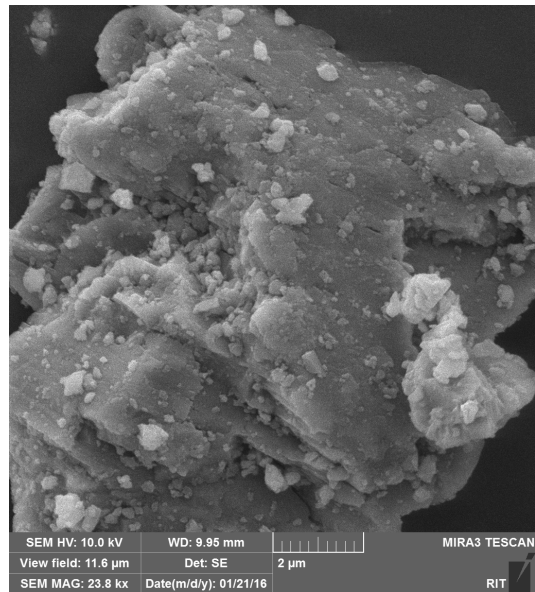
(a) SEM image of Duralum White Powder at 632x zoom



(b) SEM image of Duralum White Powder at 2550x zoom

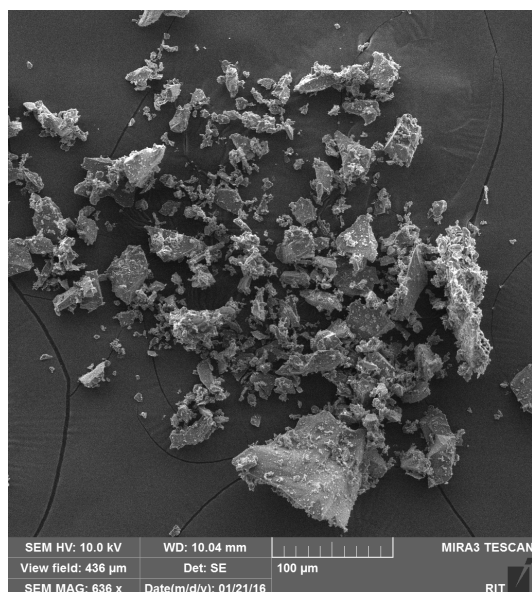


(c) SEM image of Duralum White Powder at 11700x zoom

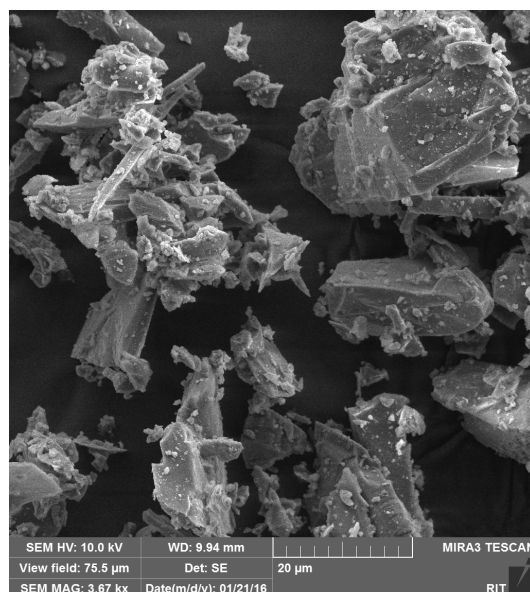


(d) SEM image of Duralum White Powder at 23770x zoom

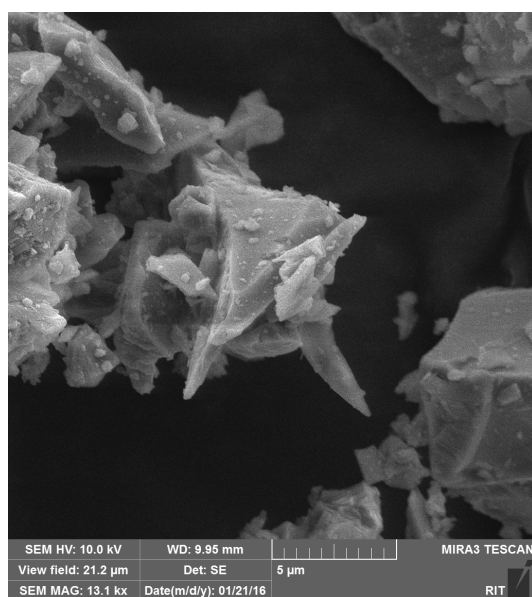
Figure B.3: Scanning Electron Microscope (SEM) images of Duralum White powder at various zooming distances



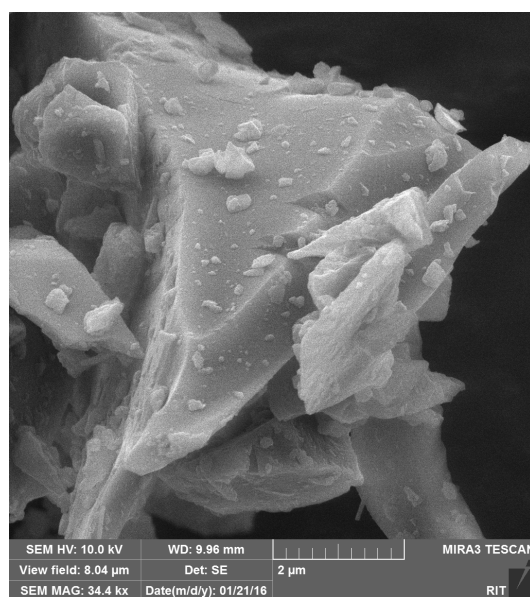
(a) SEM image of Duralum Brown Powder at 636x zoom



(b) SEM image of Duralum Brown Powder at 3760x zoom



(c) SEM image of Duralum Brown Powder at 13070x zoom



(d) SEM image of Duralum Brown Powder at 34430x zoom

Figure B.4: Scanning Electron Microscope (SEM) images of Duralum Brown powder at various zooming distances





## Appendix C

# Parameter Inversion Results: Additional Data Collections

This chapter shows the other sets of results not presented in the results chapter. Experimental collections in this section may not have had enough data points, been collected without knowledge of the contaminant mass deposited onto the surface or were repeats of results presented in the results chapter.

### C.1 Chalk on Asphalt

This example demonstrates the fidelity of the parameter inversion model on red chalk powder contaminating asphalt surfaces using the Design and Prototypes FTIR. The three-step optimization technique is used so that a spectrally depended parameter ( $\alpha(\lambda)$ ) can be estimated alongside two scalar parameters ( $\frac{n}{A}$  and  $\beta$ ). In the second optimization step, a contrast ratio is found and used to calculate the extinction cross section ( $\alpha(\lambda)$ ) which can be seen in figure C.1, where all contrast ratio data points fall between zero and one as expected.

Locations that fall under conditions where the contrast ratio is negative or above one are eliminated. For this example, there are only a handful of points at  $11.5 \mu m$  that are discarded. If a data point fails in any spectra in the family of mixtures, all are removed. In this example, one mixture had data that failed to meet the criteria at  $11.5$

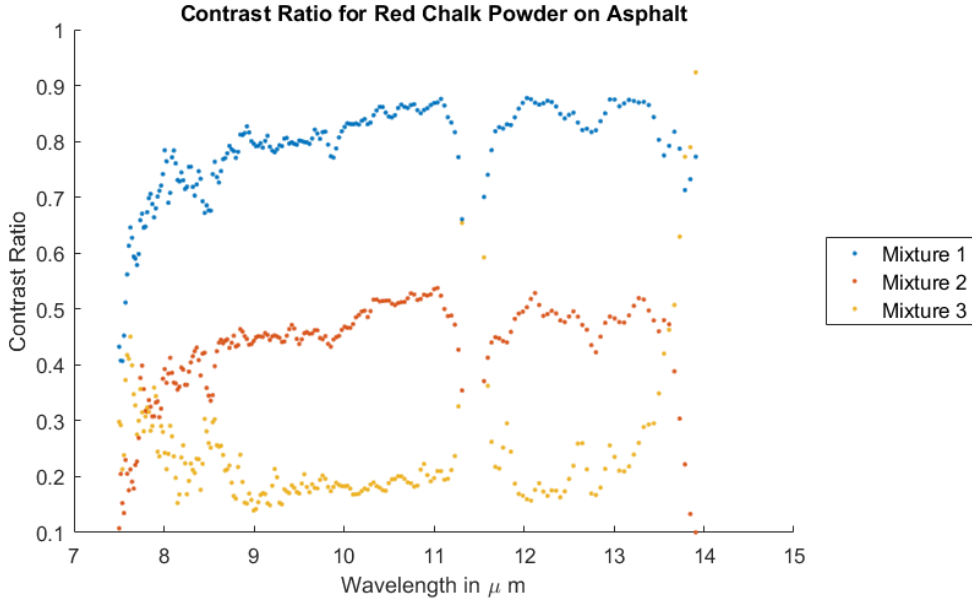


Figure C.1: Contrast Ratio for three mixtures of red chalk powder on asphalt.

$\mu m$ , but all three mixtures had this location removed. This is done to keep variable structure in the algorithm consistent for all measurements.

Once the contrast ratio is calculated, an extinction cross section can be found for each mixture amount shown in Figure C.2. This is the spectrally dependent parameter that should only describe the characteristics of the contaminant. The extinction cross section represents the total amount of incoming energy scattered or absorbed by the powder. Poor agreement across mixtures in this example could be a result of the asphalt slab having a lot of texture. In the initial parameter estimation, the algorithm may underestimate the amount of contaminant present relative to the contrast ratio for all mixtures because of these cracks, but have a larger effect on those with more contaminant present.

For a contaminant coverage with a reflectance that is spectrally close to the pure contaminant reflectance, the contrast ratio will approach zero and its logarithm will approach a very large negative number. An underestimation of coverage density due to the presence of crevasses will not modulate the contrast ratio logarithm low enough and  $\alpha(\lambda)$  estimates will appear too large.

For small amounts of contaminant, the natural log of the contrast ratio approached zero from a positive direction. The non-logarithmic term will be larger with a underes-

timated coverage density. However since the contamination present is not particularly thick, coverage density estimates from the first parameter estimation step will be considerably closer than in a thicker layer. The result of which is a reasonably close  $\alpha(\lambda)$ .

Another potential source of error comes from the collection method for this data set. Measurements collected with the D&P FTIR occur in a field setting and require clear skies, no wind or humidity and warm temperatures. Regardless, field measurements will intrinsically contain errors relative to laboratory measurements that can cascade through a parameter estimating process.

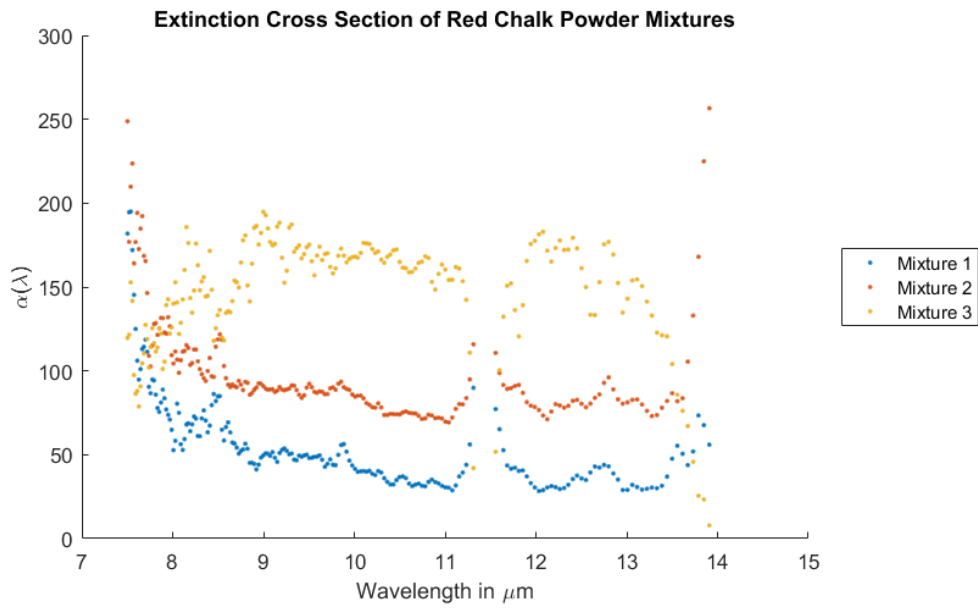


Figure C.2: Extinction cross section for three mixtures of red chalk powder.

In the third parameter estimation step, the estimated spectral  $\alpha(\lambda)$  is used to find the scalar parameters for the effective packing fraction and coverage density for each mixture via a look-up table. In Table C.1, both scalar parameters are listed alongside the computed contaminant mass present on the surface. Mixtures are listed in order of least contaminant to most contaminant present. Parameter inversion results safely fall within the bounding set by the NEFDS forward model for coverage density. The derived total contaminant mass represents the estimated amount of contaminant across the entire substrate surface. This is calculated by assuming a uniform coverage density across

Parameter Estimates for Red Chalk on Asphalt			
Mixture Number	Effective Packing Fraction ( $\beta$ )	Coverage Density ( $\frac{n}{A}$ ) in $\frac{g}{cm^2}$	Contaminant Mass (g)
Mixture 1	1.7220	0.0046	1.4868
Mixture 2	8.0100	0.0088	2.8307
Mixture 3	7.1870	0.0099	3.1948

Table C.1: Table of parameter estimates and total calculated mass for red chalk powder mixtures on asphalt.

the area directly below the sieve used to deposit contaminants. In this example, the estimates are qualitatively correct. Since truth measurements of the deposited amounts are not available, no quantitative comparison can be made.

After all three parameter values are determined, they are input into the forward NEFDS Contamination Model along with the pure contaminant and bare substrate reflectances. The output results are converted back into emissivity using Kirkoff's law with measured and modeled results being overlayed. Figure C.3 overlays the modeled data points using parameter inversion estimates with the measured D&P data. For completeness, pure material emissivities are included as well.

While the parameter inversion model worked well to estimate each physical parameter value, there remain concerns about using this material. Highly inconsistent extinction cross section estimates indicate that other parameter estimates while stable, are not sufficiently accurate.

## C.2 Quartz Sand

Another contaminant that was examined was Humboldt Calibration sand.. This sand is composed of nearly 100% quartz, but does have a wide particle size distribution. Portions of this could be considered powder, however this measurement data set was measured using the full particle size distribution. Quartz measurements were made using the Surface Optics Corporation reflectometer in the laboratory, so no environmental errors were present in the measurements, but the spot size was significantly reduced. A total of four mixtures were created and the quartz sand was placed on a Krylon 1602 black spray painted surface.

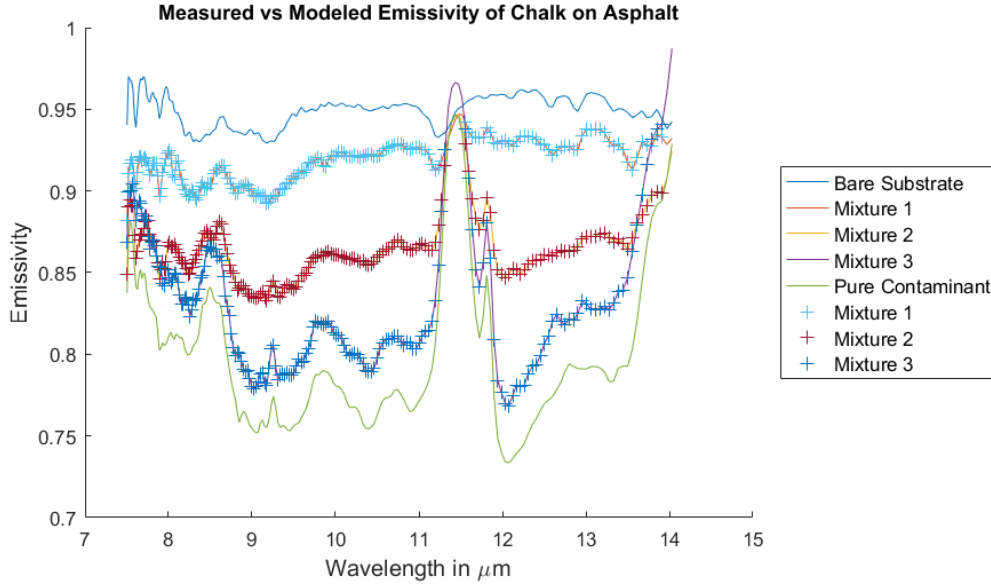


Figure C.3: Measured emissivity (solid lines) vs modeled results for mixtures of red chalk powder on asphalt. Emissivity data for the bare substrate and pure contaminant are also included.

In this example, calculated contrast ratios shown in Figure C.4 are fairly consistent with the exception of one mixture level. Several grouping of data points were eliminated because a mixture did not meet the contrast ratio standards required for further calculation. This did not preclude the parameter inversion model from performing estimates on the rest of the spectrum.

There is excellent agreement between mixtures for the extinction cross section as shown in Figure C.5. Unfortunately, because of lost data points the cross section in the region of most importance is lost. The most significant absorption feature of Quartz occurs between 8-9.5  $\mu\text{m}$ . With a small 20-30 data point exception, this section is completely missing from the  $\alpha(\lambda)$  estimates.

Scalar parameter estimates were very poor for this material. Mixtures one and two converged to the same parameter space location despite having different amounts of material present. Errors in low contaminant scalar parameter estimation did not occur due to a lack of data in the strongest absorption feature of quartz. Issues arose as a

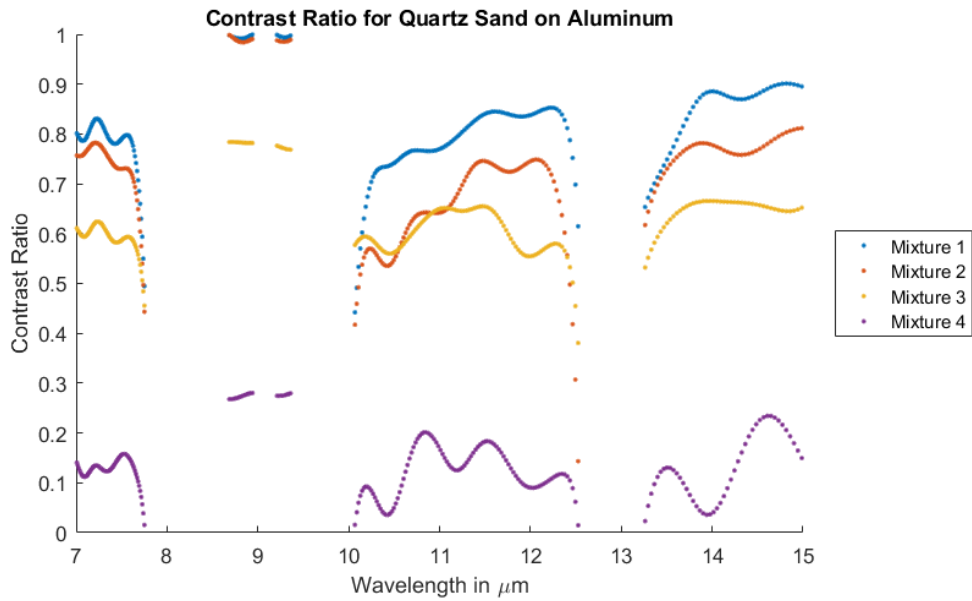


Figure C.4: Contrast ratio for four mixtures of quartz sand on Krylon 1602 spray painted aluminum.

result of too little contaminant being present and experimental error in the deposition process.

The Surface Optics Corporation reflectometer has a one centimeter diameter aperture, so it is difficult to apply small coverage densities without undershooting or overshooting the target amount. In this case, too little material was applied to the spot and the model as a whole failed. However, good estimates are made when using the results from only steps one and two of the parameter inversion.

The first two mixture coverage densities and all effective packing fraction rate es-

Three-Step Parameter Estimates for Quartz Sand on Krylon 1602 Painted Aluminum			
Mixture Number	Effective Packing Fraction ( $\beta$ )	Coverage Density ( $\frac{n}{A}$ ) in $\frac{g}{cm^2}$	Contaminant Mass (g)
Mixture 1	0.0010	0.0010	0.3232
Mixture 2	0.0010	0.0010	0.3232
Mixture 3	8.2130	0.0054	1.7690
Mixture 4	8.2640	0.0092	2.9843

Table C.2: Table of parameter estimates and total calculated mass for four mixtures of Quartz sand on Krylon 1602 painted aluminum sheet

Two-Step Parameter Estimates for Quartz Sand on Krylon 1602 Painted Aluminum			
Mixture Number	Effective Packing Fraction ( $\beta$ )	Coverage Density ( $\frac{n}{A}$ ) in $\frac{g}{cm^2}$	Contaminant Mass (g)
Mixture 1	8.1519	0.000811	0.2621
Mixture 2	7.5016	0.000915	0.2957
Mixture 3	0.2963	0.0054	1.7453
Mixture 4	6.7783	0.0093	2.0058

Table C.3: Table of parameter estimates and total calculated mass for four mixtures of quartz sand on Krylon 1602 painted aluminum. Results were obtained only with parameter estimates from steps 1,2 of the three-step parameter inversion technique.

timates shifted from the initial parameter estimates. Because the amount applied was so small, the model became unstable when estimating these parameters in the final step. This instability does not occur in the first parameter estimation step because the boundaries are more loosely defined.

Mixture emissivity signatures were recreated with the three-step parameter inversion technique for continuity with other examples. The recreated spectra again overlay well with their measured emissivity. Both bare substrate and pure contaminant are also included. This example should be redone with larger initial contaminant quantities to ensure initial parameter coverage amounts fall within acceptable boundary conditions.



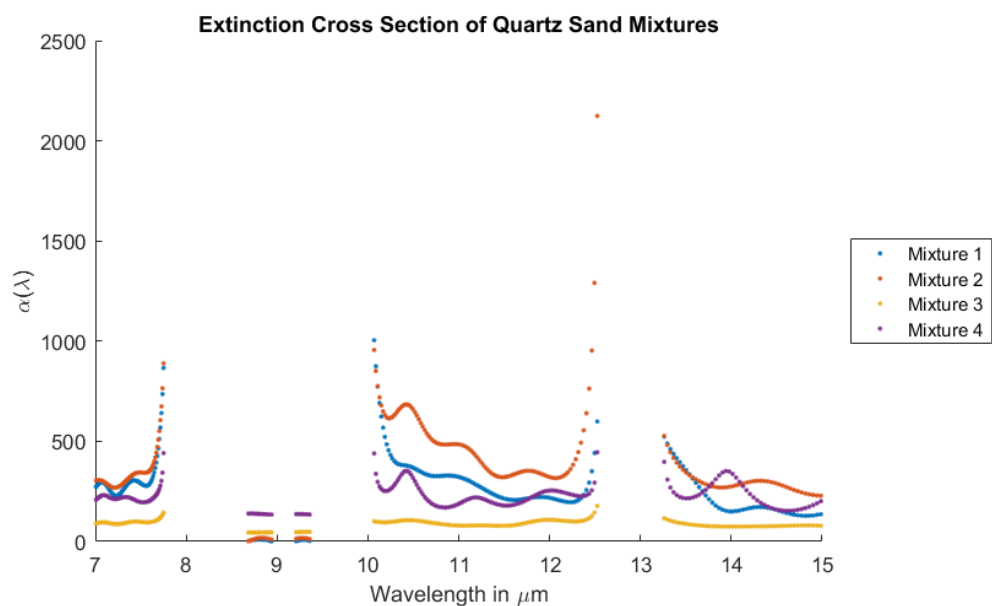


Figure C.5: Extinction cross section for four mixtures of quartz.

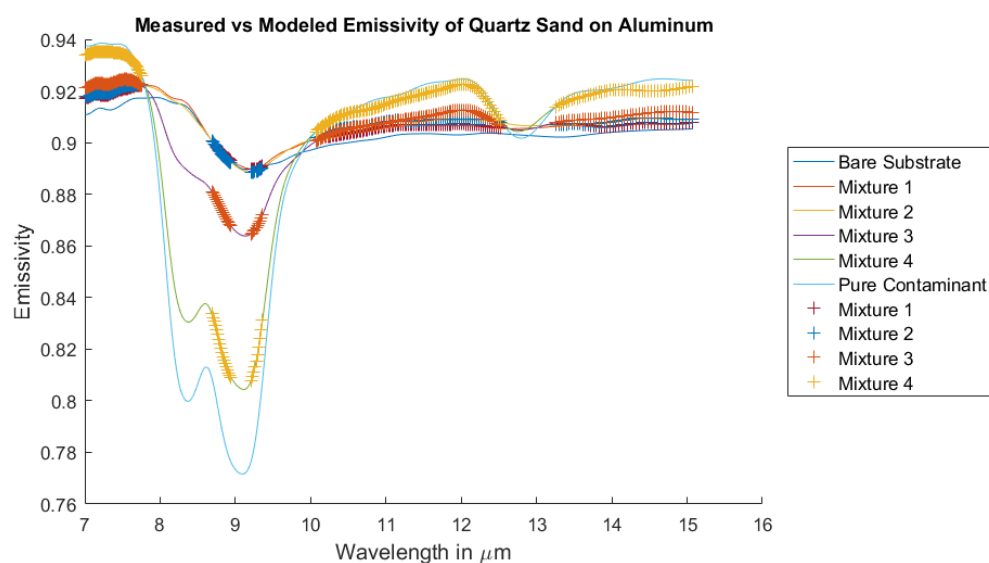


Figure C.6: Measured emissivity (solid lines) vs modeled results for four mixtures of quartz sand on Krylon 1602 painted aluminum. Emissivity data for the bare substrate and pure contaminant are also included.

## C.3 Silicon Carbide

Silicon Carbide is an example of a metallic powder manufactured by a mining company (Washington Mills) that presents a challenge to parameter estimation. A thick layer of pure Silicon Carbide powder has a spectral window from approximately 8.5-10.5  $\mu m$  that is less emissive than the substrate (black aluminum) it contaminants and a region beyond 10.5  $\mu m$  that is more emissive than the substrate. Invariably, this will lead to a single or multiple crossover points: locations where the substrate and contaminant emissivities cross as one becomes larger or smaller than the other. The substrate emissivity averages around 0.92 with contaminant surface emissivities occurring before 10.5  $\mu m$  being more emissivity and values beyond 10.5  $\mu m$  being less emissive.

Silicon Carbide like quartz, was tested on a Krylon 1602 spray painted aluminum substrate surface. Materials were deposited with a 100  $\mu m$  eight inch diameter sieve. Measurements were made in the laboratory with the SOC-400T reflectometer and spectrally smoothed using the instruments proprietary software. Settings for the smoothness algorithm were set low so as not to remove important features in the spectra.

As in the previous examples, the contrast ratios seen in Figure C.7 are mostly complete data sets with some exceptions at 8.5 and 10.6  $\mu m$ . They have very similar shapes as well, but occur at vastly different magnitudes like some of the previous materials. Again, magnitude of the contrast ratio has no standing to the validity of the estimated extinction cross section or the other estimated parameters.

Parameter Estimates for Silicon Carbide			
Mixture Number	Effective Packing Fraction Rate ( $\beta$ )	Coverage Density ( $\frac{n}{A}$ ) in $\frac{g}{cm^2}$	Contaminant Mass (g)
Mixture 1	0.5370	0.0040	1.2928
Mixture 2	3.6550	0.0083	2.9681
Mixture 3	10.000	0.0010	3.2299

Table C.4: Table of parameter estimates and total calculated mass for silicon carbide (SiC) on Krylon 1602 painted aluminum.

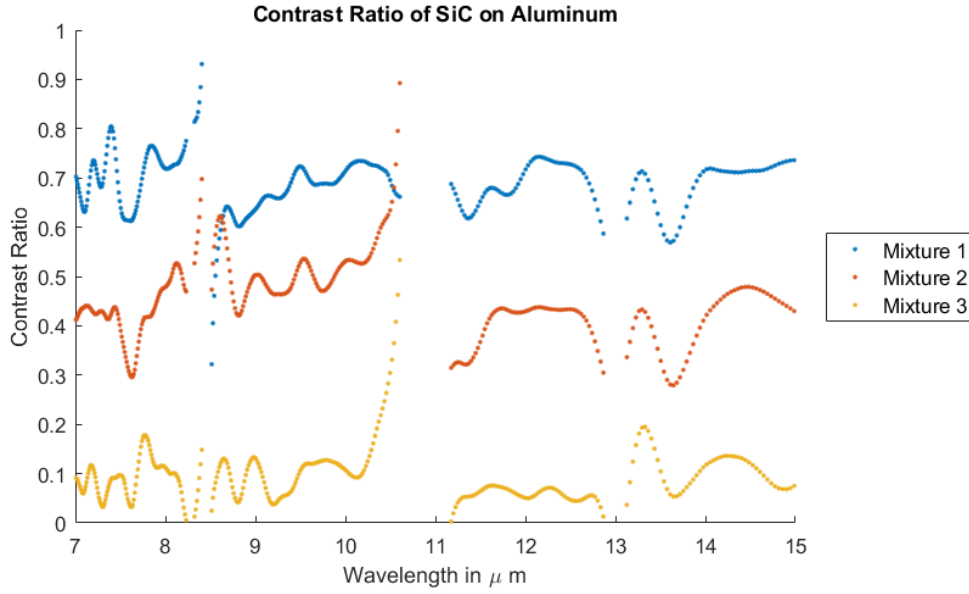


Figure C.7: Contrast ratio for three mixtures of Silicon Carbide (SiC) on Krylon 1602 painted aluminum.

In Figure C.8, estimates for extinction cross sections are shown. In mixtures one and two, agreement exists across the entire spectral region for the extinction cross section. Mixture three has an increased magnitude spectrally from the other two extinction cross sections, and appears more stretched vertically. This is very apparent at the 13-15  $\mu m$  range where peaks and troughs are exaggerated in mixture three and relative to the others.

Scalar parameter estimates take shape from the extinction cross section measurements in the next optimization steps. Like the quartz example, the estimated parameter values for the final mixture approach the maximum boundary conditions for both the

effective packing fraction rate as well as the coverage density. However, in this case the initial parameter estimates also do the same.

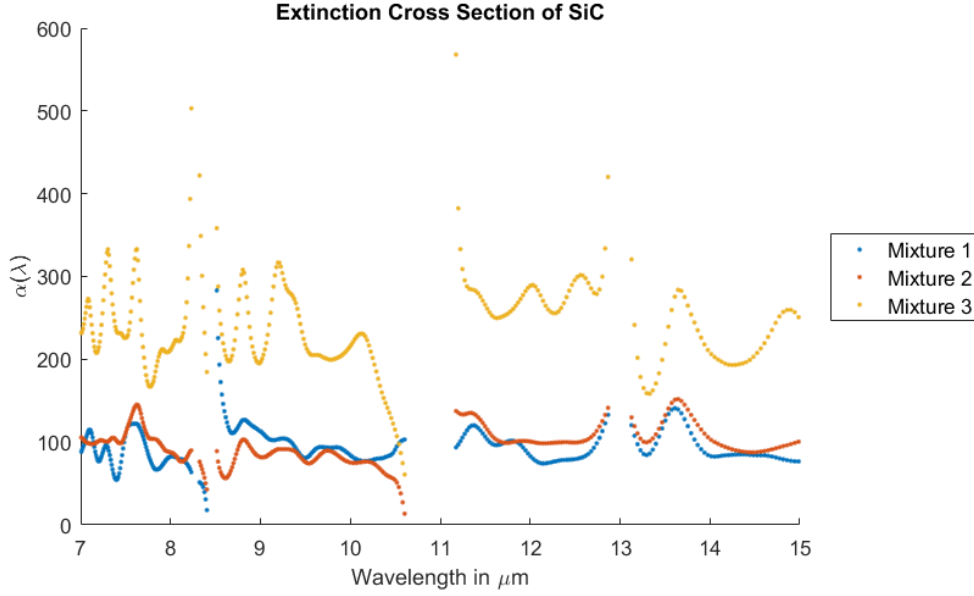


Figure C.8: Extinction cross section of three mixtures of Silicon Carbide (SiC).

One possible explanation for poor results in the final mixture is inherent to the estimation process. The NEFDS Forward model utilizes a complex exponential term to modulate the substrate and contaminant reflectances seen in equation 3.9. Because the third mixture appears so close across the spectral range examined to the spectra of the pure contaminant and due to the larger estimate of extinction cross section from the other mixtures, the exponential plays a large role. Mixture three requires the exponential term to eliminate the substrate reflectance almost completely from the equation which can only be done by forcing it to be  $\exp(1)$ .

$$f = \exp\left[\frac{\alpha(\lambda) \frac{n}{A} \ln[1 - \phi_0(1 - e^{-\beta \frac{n}{A}})]}{\phi_0(1 - e^{-\beta \frac{n}{A}})}\right] \quad (\text{C.1})$$

As seen in Equation C.1, zeroing the exponential with an already large  $\alpha(\lambda)$  requires as large a coverage density and effective packing fraction rate as possible. This pushes the other scalar parameters up to their maximum considering boundary conditions.

Despite issues with the third mixture, parameter estimates recreate the spectra for mixtures one and two very well. Mixture three works as well as shown in Figure C.9, but based on its parameter estimation, the results are suspect at best. As in previous examples, measured contaminant and bare substrates are included for completeness.

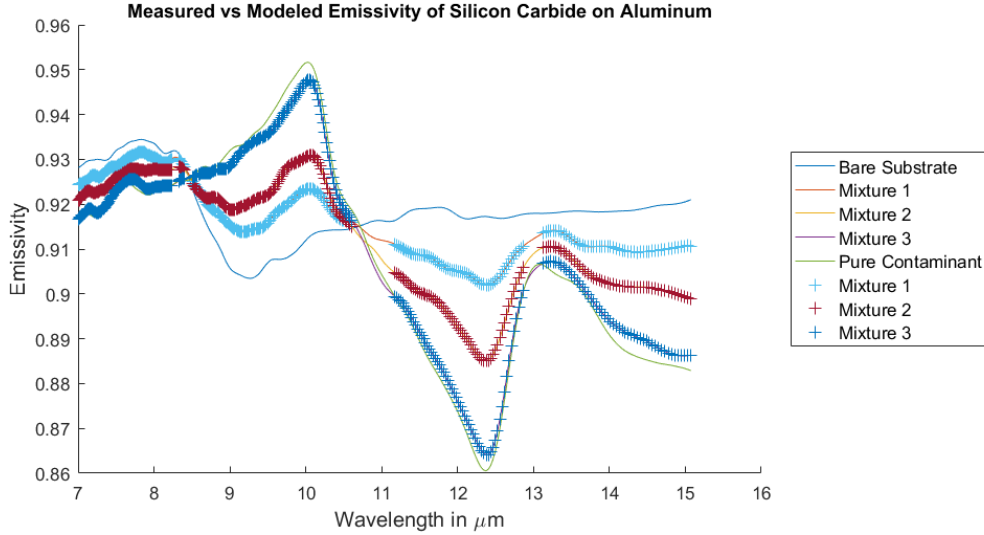


Figure C.9: Measured Emissivity (solid lines) vs modeled emissivity results for three mixtures of Silicon Carbide (SiC) on Krylon 1602 painted aluminum. Emissivity data for the bare substrate and pure contaminant are also included.

## C.4 Fused Silica

The final contaminant examined in this study is fused silica powder that also comes from Washington Mills. It is considered a powder composite because it contains the fine dust collected as remnants of the milling process. Since these are all remaining particles from milling, there occasionally exists larger particles, however a vast majority of particles in this sample will have sizes less than 20 microns. Three fused silica contaminant amounts were used to cover a flat black painted aluminum slab. Each amount of contaminant was deposited using a sieve and measured with the reflectometer previously described.

As in previous examples, Figure C.10, the contrast ratio for the extinction cross section parameter varies in magnitude between contaminant amounts. In this example,

each ratio has the same approximate shape regardless of mixture. Overall, the contrast ratio decreases with each mixture demonstrating that the difference between the mixture and contaminant approaches the magnitude of the difference between the substrate and pure contaminant as more contaminant is added (i.e. mixture 3).

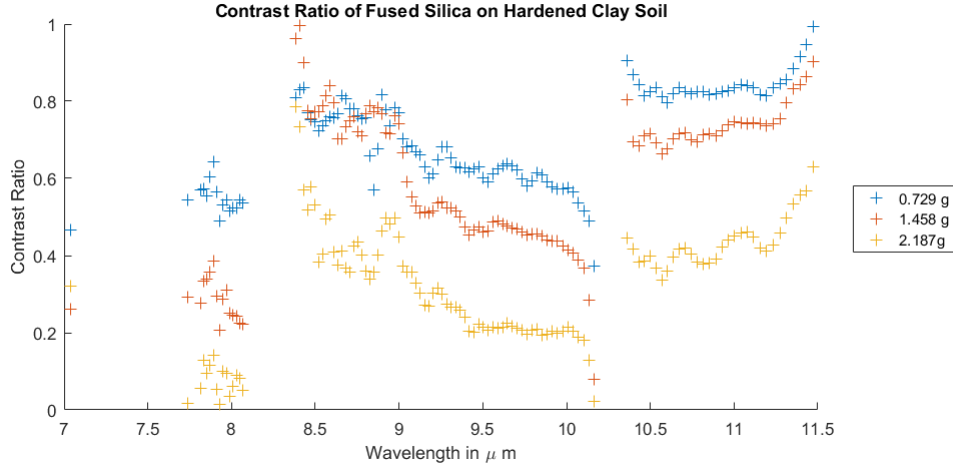


Figure C.10: Contrast Ratio for three mixtures of fused silica powder on Krylon 1602 painted aluminum.

The extinction cross section of the fused silica seen in Figure C.11 represents the best estimate for a contaminant so far. Regardless of the amount of contaminant present, the overall extinction cross section is relatively consistent at all spectral locations. Given the large differences in contrast ratio between samples, it becomes clear that the driver for consistency between samples is changes within the two scalar parameters.

Coverage density estimates shown in Table C.5 indicate little change between density estimates in the initial step to the final step of the parameter inversion model. This occurs in this example because the spectral extinction cross section estimate is relatively flat and close in magnitude to the scalar average used for the initial parameter estimate. Given the similarity, there is very little variation from the first step to the final step in estimating the scalar parameters.

Mixture to mixture, the amount of contaminant increases when more contaminant is present. With near consistency in the extinction cross section and no change between steps, it was surprising to discover that the effective packing fraction rate of the

initial mixture had reached a boundary condition. The initial estimates for this parameter never reached estimate boundaries, but had nearly identical coverage density parameters. The difference occurred in the extinction cross section. The primary estimation technique uses an averaged cross section value rather than a vector of values. Each mixture underestimated the average cross section initially which underestimated the effective packing fraction rate. Since there is no documentation regarding the ideal boundary conditions for this parameter, it is possible an increase to the boundary range is needed. Another possibility is that local minimization forced the effective packing fraction to the maximum to best fit the data.

Finally, a comparison of the measured and modeled results for fused silica is presented in Figure C.12. Even with an issue in the first mixture effective packing fraction rate, the reproduced model results represent the measured mixture emissivity well.

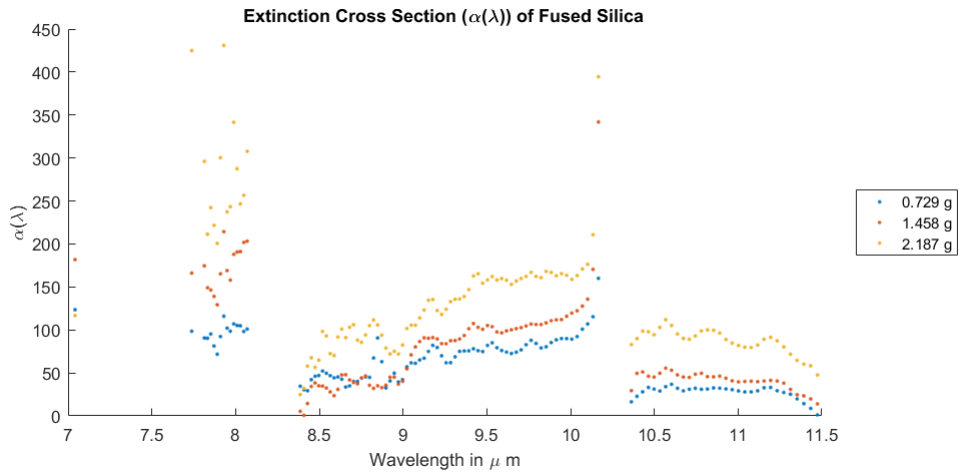


Figure C.11: Extinction cross section for three mixtures of Fused Silica powder.

Parameter Estimates for Fused Silica			
Mixture Number	Effective Packing Fraction ( $\beta$ )	Coverage Density ( $\frac{n}{A}$ ) in $\frac{g}{cm^2}$	Contaminant Mass (g)
Mixture 1	10.000	0.0013	0.4202
Mixture 2	9.3790	0.0051	1.6574
Mixture 3	8.4620	0.0091	2.9452

Table C.5: Table of parameter estimates and total calculated mass for Fused Silica powder on Krylon 1602 painted aluminum.

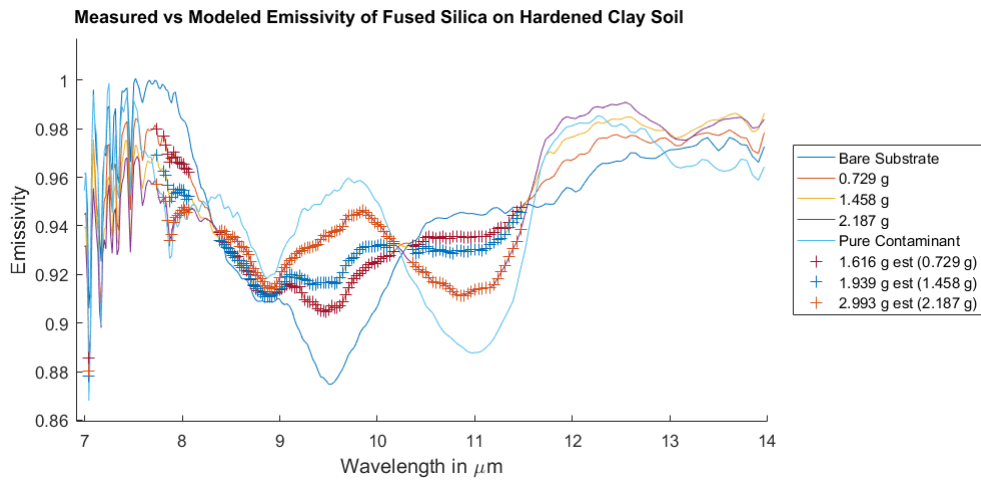


Figure C.12: Measured emissivity (solid lines) vs Modeled emissivity results for three mixtures of fused silica powder on Krylon painted aluminum. Emissivity data for the bare substrate and pure contaminant are also included.





## Appendix D

# Additional Extinction Cross Section Results

Prior the use of compressed disks with a blackbody source, the extinction cross section was measured using an infragold integrating sphere. Initial measurements were performed on the material in non-disk form simply placed in an output port cover and tamped down with a spoon. This method was challenging as the port cover was extremely small and certainty in the number density measurements were not guaranteed. The best result from this methodology is presented in this chapter. Figure D.1 shows the two measured radiance ratio plots of the silicon carbide material inside the integrating sphere. The blue line represents the lower contaminant amount and the red line represents the higher contaminant amount. Ratio values should decrease as more material is added as scattering and absorption will increase in the sphere. Figure D.2 shows the calculated extinction cross section as described by the method in chapter 4. Unlike examples using a blackbody and disk, the extinction cross section in this case is extremely low and spectrally uninteresting in the longwave infrared range.

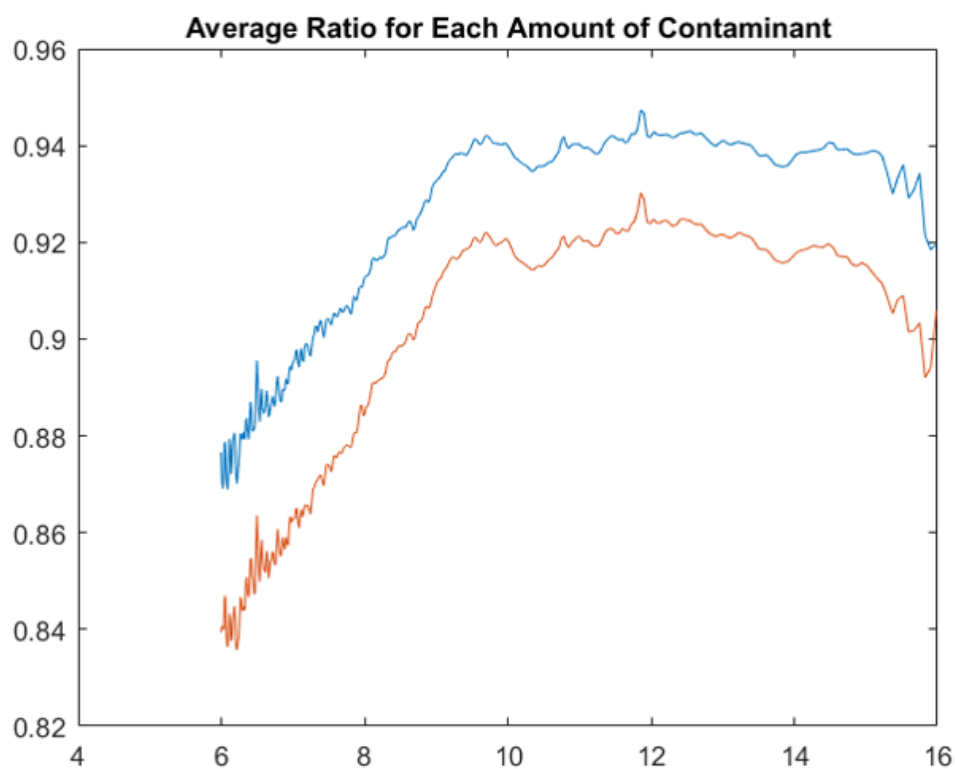


Figure D.1: Average ratio of two amounts of silicon carbide powder placed inside the port cover of an infragold integrating sphere. The silicon carbide was not compressed into a disk prior to placement inside the integrating sphere.

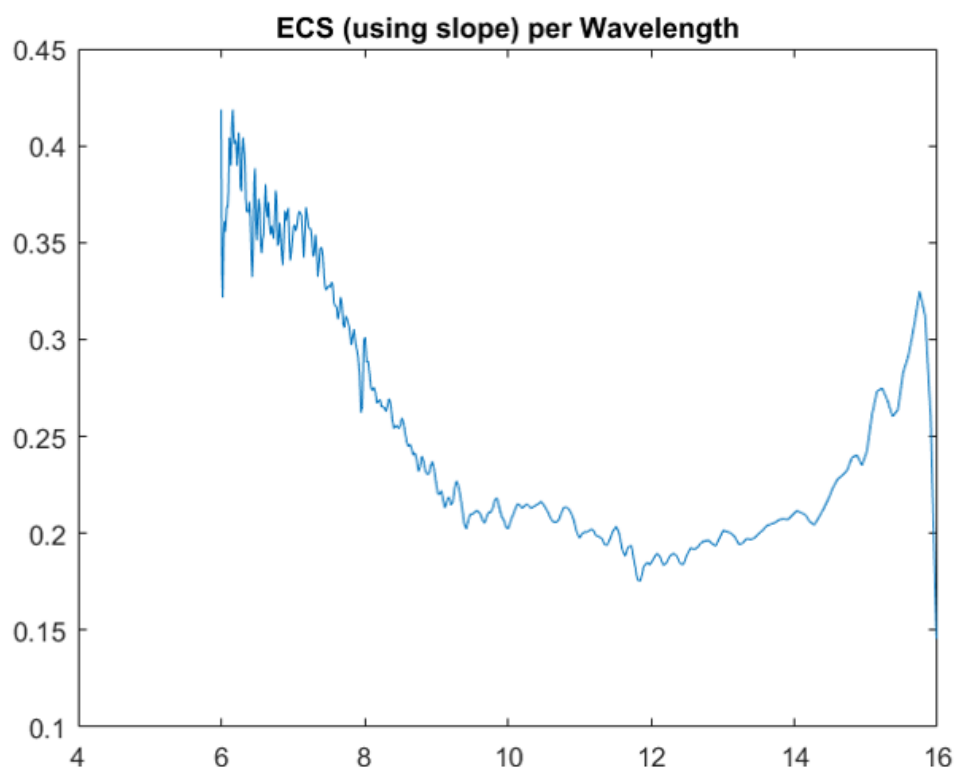


Figure D.2: Resulting extinction cross section measurement of the uncompressed silicon carbide material placed in the output port cover of the infragold integrating sphere.

Once a method that utilized compressed disks of known material was employed, disks were placed inside the integrating sphere and that apparatus was directly attached to the instrument. The major issue with that set-up was that the integrating sphere has an exceedingly high reflectivity rate in the longwave infrared. Because the instrument had a sensor cooling liquid nitrogen dewar, an internal reflection occurred that reached the sensor and caused error within the radiance ratio measurements. This phenomena can be seen in figure D.3 where over the course of an hour, the measured ratio spectra remained above 1.0 at almost every single wavelength, despite having well characterized contaminant densities from the disks. The extinction cross sections that were calculated from these ratio measurements were near and sometimes below zero as can be seen in figure D.4, where fused silica powder disks produced a negative extinction cross section due to internal sensor reflections. In this example, extinction cross section calculates at

wavelengths from 8.992 to 12.75  $\mu\text{m}$  fell below one. Even when the internal reflection issue was corrected, the signal produced by the integrating sphere light source was too weak and unstable to produce reasonable results. This is why the integrating sphere was replaced with the blackbody setup.

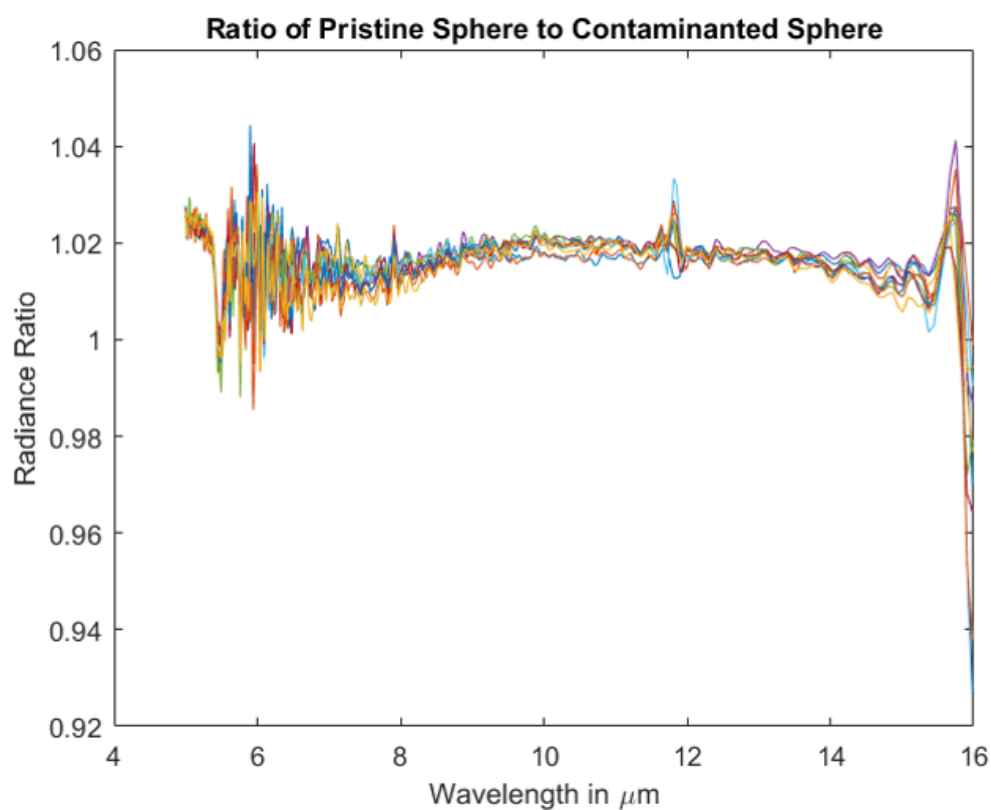


Figure D.3: Radiance ratios of fused silica to a pristine sphere found over a period of 1 hour.

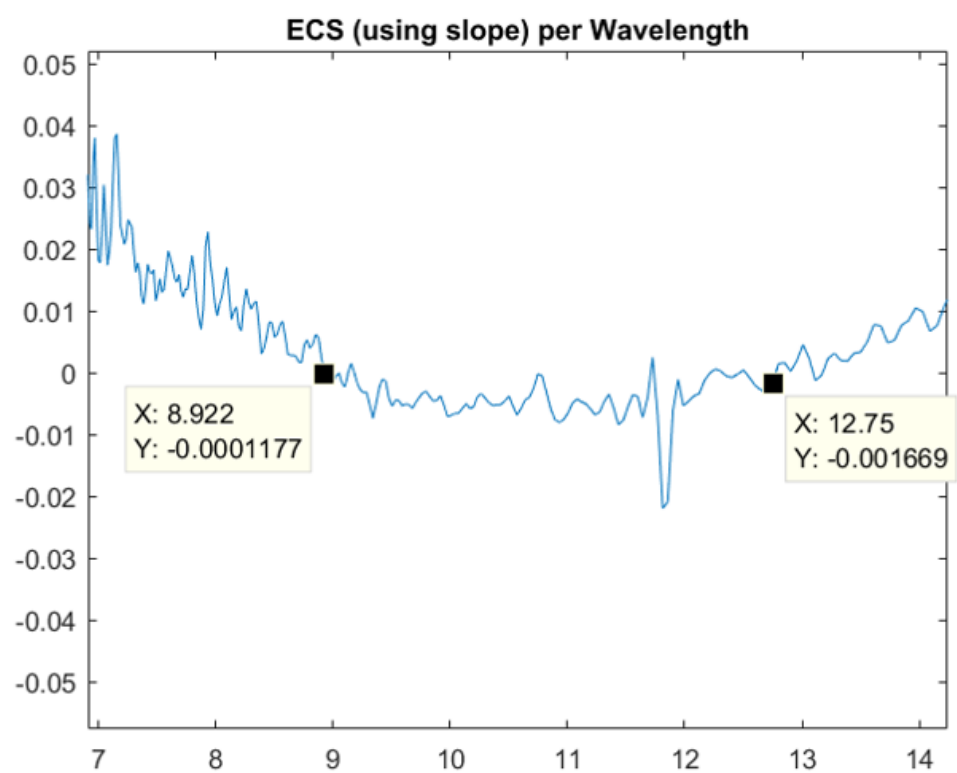


Figure D.4: Extinction cross section generated from fused silica in a infragold integrating sphere.



## Appendix E

# ROC Curve Results for Blue Heron Synthetic Targets

Airborne hyperspectral images that contained synthetic target signatures were also visualized using receiver operator characteristic curves to show the detection rate against false alarms. This method was done for all target detection algorithms employed by the ENVI software tool including ACE, Matched Filter, Spectral Angle Mapper (SAM), and Constrained Energy Minimization (CEM). Each of the four detection methods was applied to an emissivity image from Blue Heron with synthetic targets against four target spectra. The ROC figures presented in this chapter represent each of those spectra. The ACE algorithm results are generated from ENVI's ACE algorithm. The purpose of exhibiting these results is to demonstrate how the detection rate for each algorithm decreases in efficiency as the target spectrum used becomes less like the pure contaminant spectrum.

The four ROC curves presented were generated using a Blue Heron sensor collection at 18:07:02 UTC time on 11/3/16. This is the same file used in Chapter 5. Synthetic targets utilized parameter inversion model estimates for Silicon Carbide contaminant powder. Targets were generated in 10% sub-pixel intervals up to full pixel coverage with a total of 243 target pixels present.



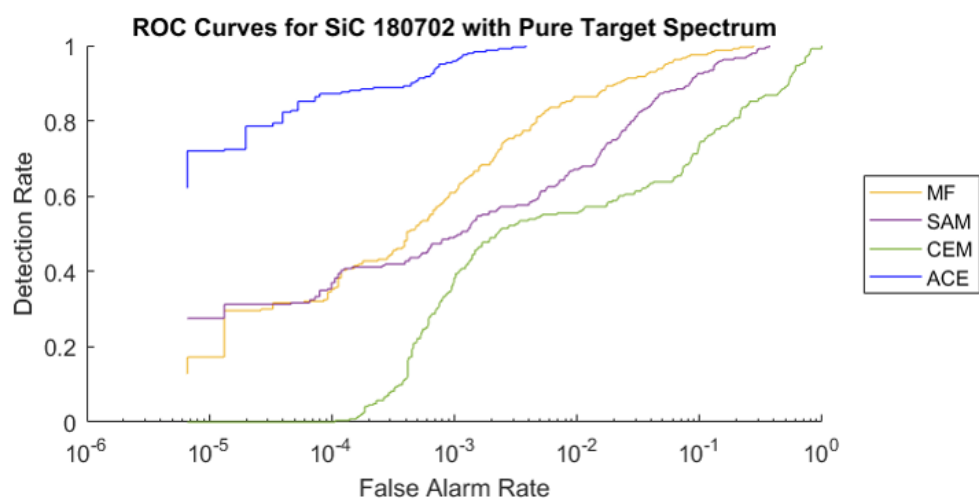


Figure E.1: ROC generated curves for pure silicon carbide target spectrum using ACE, MF, CEM, and SAM target detection algorithms.

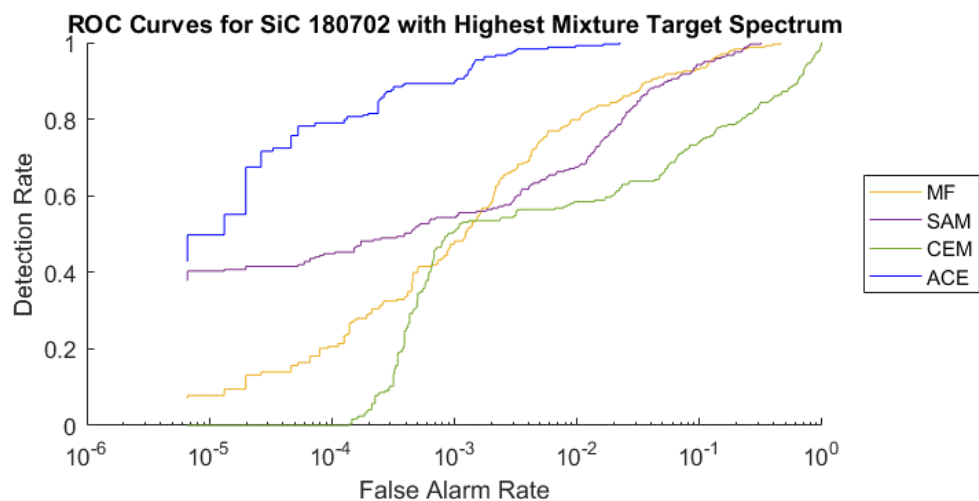


Figure E.2: ROC generated curves for highest mixture amount of silicon carbide target spectrum using ACE, MF, CEM, and SAM target detection algorithms.

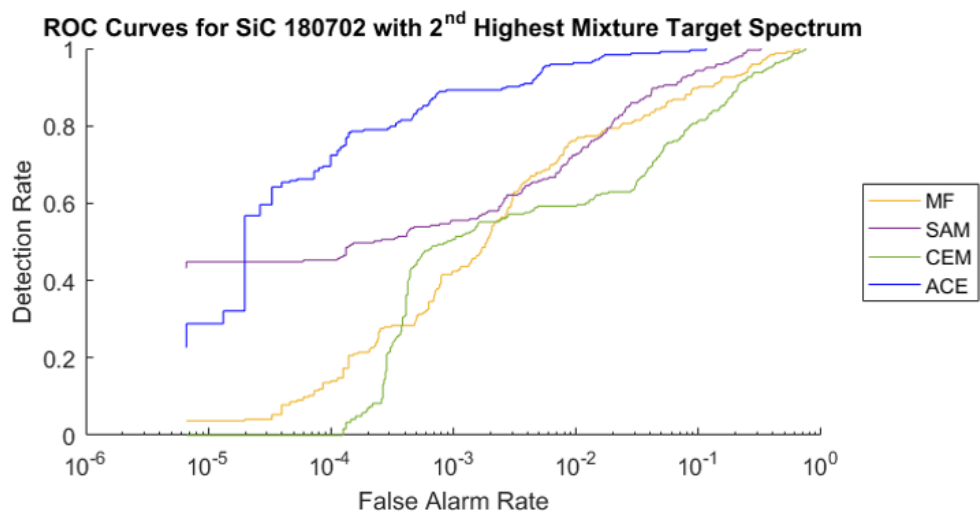


Figure E.3: ROC generated curves for second highest mixture amount of silicon carbide target spectrum using ACE, MF, CEM, and SAM target detection algorithms.

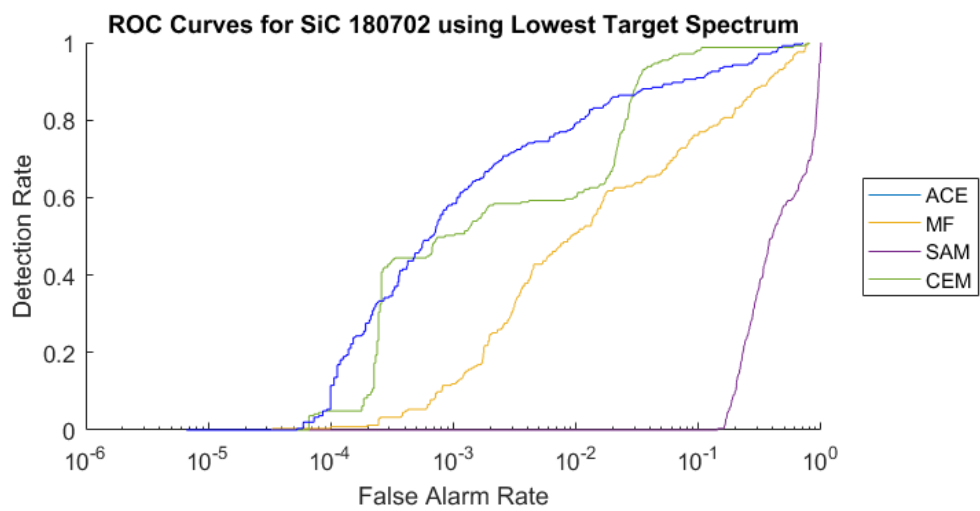


Figure E.4: ROC generated curves for lowest mixture amount of silicon carbide target spectrum using ACE, MF, CEM, and SAM target detection algorithms.



# Bibliography

- [1] F. L. Pedrotti, L. S. Pedrotti, and L. M. Pedrotti, *Introduction to Optics*. New York: Pearson, 2007.
- [2] J. R. Johnson, P. G. Lucey, and K. A. Horton, “Infrared measurements of pristine and disturbed soils 1. spectral contrast differences between field and laboratory data,” *Remote Sensing Environment*, vol. 64, pp. 34–46, 1998.
- [3] C. Borel, “Error analysis for a temperature and emissivity retrieval algorithm for hyperspectral imaging data,” in *Algorithms for Multispectral, Hyperspectral and Ultraspectral Imagery XIII*, vol. 6565, pp. 1–10, SPIE, 2007.
- [4] C. Borel, “Artemiss an algorithm to retrieve temperature and emissivity from hyper-spectral thermal image data,” in *28th Annual GOMACTech Conference, Hyperspectral Imaging Session*, GOMACTECH, 2003.
- [5] P. G. Lucey, T. J. Williams, M. Mignard, J. Julian, D. Kobubun, G. Allen, D. Hampton, W. Schaff, M. J. Schlangen, E. M. Winter, W. B. Kendall, A. D. Stocker, K. A. Horton, and A. P. Bowman, “Ahi: an airborne long-wave infrared hyperspectral imager,” in *Airborne Reconnaissance XXII*, vol. 3431, SPIE, 1998.
- [6] S. Darling and C. Salvaggio, *A Novel Approach to Temperature-Emissivity Separation Using a Multiple-Window Smoothness Criteria*. PhD thesis, Rochester Institute of Technology, 2013.
- [7] M. R. Smith, A. R. Gillespiea, H. Mizzona, L. K. Balickb, J. C. Jimnez-Muozc, and J. A. Sobrinoc, “In-scene atmospheric correction of hyperspectral thermal infrared data with nadir, horizontal and oblique view angles,” *International Journal of Remote Sensing*, vol. 34, pp. 9–10, 2013.

- [8] S. J. Young, B. R. Johnson, and J. A. Hackwell, "An in-scene method for atmospheric compensation of thermal hyperspectral data," *Journal of Geophysical Research*, vol. 107, 2002.
- [9] M. Boonmee, *Land Surface Temperature and Emissivity Retrieval from Thermal Infrared Hyperspectral Imagery*. PhD thesis, Rochester Institute of Technology, 2007.
- [10] J. R. Schott, *Remote Sensing: The Imaging Chain Approach*. New York: Oxford University Press, 2007.
- [11] D. Pogorzala, "Gas plume identification in lwir hyperspectral imagery by regression analyses," Master's thesis, Rochester Institute of Technology, 2005.
- [12] S. Walsh, L. Chilton, M. Tardiff, and C. Metoyer, "Effect of the temperature-emissivity contrast on the chemical signal for gas plume detection using thermal image data," *Sensors*, vol. 8, pp. 6471–6483, 2008.
- [13] M. Eismann, *Hyperspectral Remote Sensing*. Bellingham, WA: SPIE, 2012.
- [14] D. W. Messinger, C. Salvaggio, and N. M. Sinisgalli, "Detection of gaseous effluents from airborne lwir hyperspectral imagery using physicals-based signatures," *International Journal of High Speed Electronics and Systems*, vol. 20, no. 10, pp. 1–12, 2006.
- [15] A. Reinov, Y. Bushlin, A. Lessin, and D. Clement, "Dew, dust, and wind influencing thermal signatures of objects," in *Infrared Imaging Systems: Design Analysis, Modeling, and Testing XIX*, vol. 6941, pp. 1–10, SPIE, 2008.
- [16] S. Archer, M. Gartley, J. Kerekes, B. Cosofret, and J. Giblin, "Empirical measurement and model validation of infrared spectra of contaminated surfaces," in *Algorithms and Technologies for Multispectral, Hyperspectral and Ultraspectral Imagery XXI*, vol. 9472, pp. 1–13, SPIE, 2015.
- [17] J. Kerekes, M. Gartley, C. D. Angelis, C. Salvaggio, C. Gittins, M. Costolo, and B. Cosofret, "Measurements and modeling of lwir spectral emissivity of contaminated quartz sand," in *Workshop on Hyperspectral Image and Signal Processing, Evolution in Remote Sensing, Workshop on Hyperspectral Image and Signal Processing, Thermal Hyperspectral Imaging*, pp. 1–10, IEEE, 2013.

- [18] J. W. Salisbury and D. M. D'Aria, "Emissivity of terrestrial materials in the 8-14 micron atmospheric window," *Remote Sensing Environment*, vol. 42, pp. 83–106, 1992.
- [19] T. D. Carson, C. M. Bachmann, and C. Salvaggio, "Soil signature simulation of complex mixtures and particle size distributions," *Optical Engineering*, vol. 54, no. 9, pp. 1–8, 2015.
- [20] C. M. Pieters and P. A. J. Englert, *Remote Geochemical Analysis: Elemental and Mineralogical Composition*. New York: Oxford University Press, 1993.
- [21] J. W. Salisbury and A. Wald, "The role of volume scattering in reducing spectral contrast of reststrahlen bands in spectra of powdered minerals," *ICARUS*, vol. 96, pp. 121–128, 1992.
- [22] J. Salisbury and D. D'Aria, "Measurement of christiansen frequencies in spectra of particulate samples for determination of rock composition," *Abstracts of the Lunar and Planetary Science Conference*, vol. 20, pp. 940–941, 1989.
- [23] B. Hapke, *Theory of Reflectance and Emittance Spectroscopy*. New York: Cambridge University Press, 2012.
- [24] J. Moersch and P. Christensen, "Thermal emission from particulate surfaces: A comparison of scattering models with measured spectra," *Journal of Geophysical Research*, vol. 100, no. E4, pp. 7465–7477, 1995.
- [25] J. R. Johnson, W. M. Grundy, and M. K. Shepard, "Visible/near-infrared spectrogoniometric observations and modeling of dust-coated rocks," *ICARUS*, vol. 171, pp. 546–556, 2004.
- [26] K. Stone, J. Keller, M. Popescu, and C. Spain, "Buried explosive hazard detection using forward-looking long-wave infrared imagery," in *Detection and Sensing of Mines, Explosive Objects, and Obscured Targets XVI*, vol. 8017, pp. 1–15, SPIE, 2011.
- [27] T. Blake, C. S. Brauer, M. R. Kelly-Gorham, S. D. Burton, M. Bliss, T. L. Myers, and T. J. Johnson, "Measurement of the infrared optical constants for spectral modeling: n and k values for (nh<sub>4</sub>)<sub>2</sub>so<sub>4</sub> via single-angle reflectance and ellipsometric methods," in *Algorithms and Technologies for Multispectral, Hyperspectral and Ultraspectral Imagery XXIII*, vol. 10198, pp. 1–9, SPIE, 2017.

- [28] R. G. TOnkyn, T. O. Danby, J. L. Birnbaum, M. S. Taubman, B. E. Bernacki, T. J. Johnson, and T. L. Myers, "Measurement of infrared refractive indices of organic and organophosphorous compounds for optical modeling," in *Algortihms and Technologies for Multispectral, Hyperspectral and Ultraspectral Imagery XXIII*, vol. 10198, pp. 1–9, SPIE, 2017.
- [29] D. DiMarzio, R. Haberstroh, S. Chu, N. Fonneland, and C. May, "Contamination modeling document supplement to nefds modeling document," tech. rep., National Geospatial-Intelligence Agency, Cortana Corporation, 2013.
- [30] M. Gartley, J. Schott, and S. Brown, "Micro-scale modeling of contaminant effects on surface optical properties," in *Imaging Spectrometry XIII*, vol. 7086, pp. 1–12, SPIE, 2008.
- [31] Designs and Prototypes LTD, *Model 102F Portable FTIR Instruction Manual*, 2003.
- [32] C. Salvaggio and C. J. Miller, "Comparison of field and laboratory collected mid-wave and longwave infrared spectra/data reduction techniques," in *Algortihms for Multispectral, Hyperspectral and Ultraspectral Imagery*, vol. 4381, pp. 549–559, SPIE, 2001.
- [33] C. Salvaggio and C. J. Miller, "Methodologies and protocols for the collection of midwave and longwave infrared emissivity spectra using a portable field spectrometer," in *Algortihms for Multispectral, Hyperspectral and Ultraspectral Imagery*, vol. 4381, pp. 539–549, SPIE, 2001.
- [34] Surface Optics Corporation, *SOC 400T User Guide*, 2002.
- [35] Digital Imaging and Remote Sensing Laboratory at the Chester F. Carlson Center for Imaging Science, *SOC 400T Field Use Protocol*, 2004.
- [36] M. Z. Salvador, "Expanding the dimensions of hyperspectral imagery to improve target detection," in *Extro-Optical Remote Sensing X*, vol. 9988, pp. 1–, SPIE, 2016.
- [37] J. Kerekes, K.-E. Strackerjan, and C. Salvaggio, "Spectral reflectance and emissivity of man-made surfaces contaminated with environmental effects," *Optical Engineering*, vol. 47, pp. 1–10, 2008.

- [38] D. Manolakis, D. Marden, and G. A. Shaw, “Hyperspectral image processing for automatic target detection applications,” *Lincoln Laboratory Journal*, vol. 14, pp. 79–116, 2003.
- [39] T. D. Carson and C. Salvaggio, “Signature simulation of mixed materials,” in *Radar Sensor Technology XIX; and Active and Passive Signatures VI*, vol. 9461, pp. 1–12, SPIE, 2015.
- [40] J. R. Shell, *Polarimetric Remote Sensing in the Visible to Near Infrared*. PhD thesis, Rochester Institute of Technology, 2005.
- [41] T. D. Carson, *Signature Simulation and Characterization of Mixed Solids in the Visible and Thermal Regions*. PhD thesis, Rochester Institute of Technology, 2015.
- [42] L. Moreau, H. Bourque, R. Ouellet, C. Roy, C. Vallieres, and G. Theriault, “A field-deployable spectral reflectometer to characterize surfaces in the infrared from the nir to the lwir,” in *Infrared Technology and Applications XXXVII*, vol. 8012, pp. 1–9, SPIE, 2011.
- [43] T. A. Reichardt and T. J. Kulp, “Radiative transfer modeling of surface chemical deposits,” in *Algorithms and Technologies for Multispectral, Hyperspectral and Ultraspectral Imagery XXII*, vol. 9840, pp. 1–8, SPIE, 2016.
- [44] T. Gibbs and D. Messinger, “NEFDS contamination model parameter estimation of powder contaminated surfaces,” in *Algorithms and Technologies for Multispectral, Hyperspectral and Ultraspectral Imagery XXII*, vol. 9840, pp. 1–13, SPIE, 2016.
- [45] J. R. Ballard, S. E. Howington, and S. C. Wilhelms, “Laboratory-based rainfall effects on lwir soil reflectance,” *IEEE Geoscience and Remote Sensing Letters*, vol. 10, pp. 627–630, 2013.
- [46] T. Gibbs and D. Messinger, “Contaminant mass estimation of powder contaminated surfaces,” in *Algorithms and Technologies for Multispectral, Hyperspectral and Ultraspectral Imagery XXIII*, vol. 10198, pp. 1–13, SPIE, 2017.
- [47] T. L. Myers, C. S. Brauer, Y.-F. Su, T. A. Blake, R. G. Tonkyn, A. B. Ertel, T. J. Johnson, and R. L. Richardson, “Quantitative reflectance spectra of solid powders as a function of particle size,” *Applied Optics*, vol. 54, no. 15, pp. 4863–4875, 2015.



- [48] R. Heylen, M. Parente, and P. Gader, “A review of nonlinear hyperspectral unmixing methods,” *IEEE Journal Of Special Topics in Applied Earth Observations and Remote Sensing*, vol. 7, no. 6, pp. 1844–1868, 2014.
- [49] J. M. Bioucas-Dia, A. Plaza, N. Dobigeon, M. Parente, Q. Du, P. Gader, and J. Chnussot, “Hyperspectral unmixing overview: Geometrical statistical, and sparse regression-based approaches,” *IEEE Journal of Selected Topics in Applied Earth Observations and Remote Sensing*, vol. 5, no. 2, pp. 354–379, 2012.
- [50] N. Keshava and J. F. Mustard, “Spectral unmixing,” *IEEE Signal Processing Magazine*, vol. 19, no. 1, pp. 44–57, 2002.
- [51] J. W. Boardman, “Geometric mixture analysis of imaging spectrometry data,” in *International Geoscience and Remote Sensing Symposium (IGARRS)*, vol. 115, pp. 2369–2371, IEEE, 1994.
- [52] F. Kruse, “Comparisoin of ATREM, ACORN, and FLAASH atmospheric corrections using low-altitude AVIRIS data of Boulder, CO,” in *Summaries of 13th JPL Airborne GeoSciences Workshop*, pp. 1–10, Jet Propulsion Lab, 2004.